November 2020

Hybrid RF Acoustic Resonators and Arrays with Integrated Capacitive and Piezoelectric Transducers

Adnan Zaman
University of South Florida

Hybrid RF Acoustic Resonators and Arrays with Integrated Capacitive and Piezoelectric Transducers

by

Adnan Zaman

A dissertation submitted in partial fulfillment
of the requirements for the degree of
Doctor of Philosophy
Department of Electrical Engineering
College of Engineering
University of South Florida

Major Professor: Jing Wang, Ph.D.
Sylvia Thomas, Ph.D.
Arash Takshi, Ph.D.
Rasim Guldiken, Ph.D.
Jiangfeng Zhou, Ph.D.

Date of Approval:
November 9, 2020

Keywords: Microelectromechanical Systems, Motional Resistance, Quality Factor, Vibrating Micromechanical Resonators

Dedication

To my grandfather, my parents, my wife, my kids, and my friends

Acknowledgments

First, I would like to state my greatest appreciation to my major advisor and Professor Dr. Jing Wang for always providing his guidance on my academic research. It has been a great and valuable experience to learn from him and work with him for the past seven years.

I would also like to greatly acknowledge the contributions from all the current and former group members of RF MEMS Transducers Group, especially Abdulrahman Alsolami, Ting-Hung Liu, Xu Han, Ugur Guneroglu, and Adrian Avila for spending time and helping me with MEMS fabrication in the cleanroom and in our lab for countless days and nights; Also, I want to thanks all NREC staffs especially Rich Everly for providing assistance in cleanroom training and fabrication techniques. Also, special thanks to King Abdulaziz City for Science and Technology for supporting this work.

Lastly and more importantly, I deeply indebted to my father, my mother, my brothers and sisters for supporting me and helping me to pursue my dreams. My deepest appreciation goes to my wife and my kids for offering me endless love and support during my Ph.D. journey.

Table of Contents

List of Tables

List of Figures

Abstract

Over the past few decades, the usage of mobile communication devices such as smartphones, laptop computers, tablets has grown significantly. Clearly, smartphones and other mobile gadgets have been leading the current and emerging market thanks to the fast growing of wireless communications. Therefore, the wireless communications market is constantly looking for new ways to miniaturize the RF front-ends, while reducing the size, cost, and power consumption. Radio frequency microelectromechanical systems (RF MEMS) is widely viewed as a potential enabling technology for the multi-standard monolithic transceivers on a single chip with high reliability, high performance, and very low DC power consumption. Among a wide variety of RF MEMS device components, resonators offer unique benefits because of their very high-quality factors, which enable the implementation of advanced functions such as low insertion loss filters, mixer-filters, ultra-low phase noise oscillators, and even potential future RF front-end channel selection instead of band selection for realizing true software defined radio all in GHz frequencies. The film bulk acoustic resonators (FBAR's) and surface acoustic wave (SAW) resonators are piezoelectric resonators that have already been successfully implemented into commercial products in mass consumer electronics for more than a decade. Apparently, vibrating micromechanical resonators such as FBAR's can perform really well while enabling significant power reduction as compared to conventional RF systems. Nonetheless, both FBAR and SAW devices fall short of satisfying the performance requirements, such as quality factor at a frequency below 2 GHz by future single-chip transceiver with multi-frequency functionality. Moreover, the quality factor drops notably as the resonance frequency approaches 3 GHz and beyond. Therefore,

contour-mode resonators have been developed to replace FBAR at VHF and UHF frequencies, since their resonance frequencies are defined by lateral dimensions while being able to deliver moderate quality factor and low insertion loss to enable multi-frequency functionality on a single chip. Nevertheless, the motional impedance of these devices is still considerably higher than the value needed to match to 50 Ω RF front-end electronics. On the other hand, capacitively-transduced micromechanical resonators can achieve very high quality factor and can operate at even higher frequency, which is challenging for piezoelectric counterparts to achieve. However, relatively high motional impedance and high insertion loss is still a big issue for these devices to interface with standard 50 Ω systems. Shrinking the capacitive transducer air gap between the electrodes and the resonator body to sub-10 nm might partially solve this problem, which demands very complex fabrication processes as compared to piezoelectric resonators. Furthermore, the employment of nanogap capacitive transducers gives rise to higher fabrication cost, lower yield, poorer reliability, and reproducibility of those devices. Another solution to lower the motional impedance by improving the transduction efficiency is to use piezoelectric transducers that are capable of achieving fairly low motional impedances. For instance, piezoelectrically transduced TPoS resonators enabled by the SOI technology are capable of operating at frequencies up to a few GHz while retaining its performance reliability. Even after being equipped with all the benefits of both piezoelectric and electrostatic (capacitive) resonators, neither of these two resonator technologies can undoubtedly fulfill all the needed performance specifications for single-chip multi-frequency RF front-end applications. Meanwhile, it is obvious that these two transduction mechanisms can efficiently complement each other. Hence, a novel hybrid resonator is proposed herein by combining electrostatic micromechanical resonator with piezoelectric thin-

film transducer to exhibit low acoustic losses along with high electromechanical coupling coefficients, which could resolve the aforementioned issues hindering MEMS resonators.

Chapter 1: Introduction

1.1 Objective

Wireless electronic devices such as laptops, GPS, phones, and Wi-Fi tablets have become part of our daily necessities. The fast growing of these devices heavily relies on the development of wireless technology. The wireless market is always looking for new ways to further miniaturize the RF front-ends while reducing the size, cost, and power consumption. Silicon micromechanical resonators are expected to replace current commercial quartz-crystal resonators. Similarly, coupled silicon resonators are expected to potentially replace the SAW and BAW devices in the future, as thin-film piezoelectric on silicon (TPoS) based filter technology has already used silicon as the resonator body structural material for the improved acoustic energy stored per cycle. Therefore, current research efforts have been heavily relying on silicon as a medium for storing the acoustic energy with reduced losses. However, there are still significant problems that need to be solved before considering silicon micromechanical resonator to be a functional building-block device for successful consumer applications in RF front ends that include:

- High motional impedance: Electrostatically transduced resonators suffer from high motional impedance, which can be a cumbersome bottleneck against the employment of such devices in front-end transceivers due to large impedance mismatch between the resonators and antennae or other front-end modules.
- Limited Q-factor in piezoelectric devices: Thin-film piezoelectric transducers have demonstrated higher electromechanical coupling coefficients, while holding slightly higher material related losses, thus resulting in lower and limited Q-factor.

- High polarization voltage (Vp) in capacitive devices: Capacitively-transduced micro-resonators need a high DC-bias voltage potential to operate (>30 V), which demands special power supply circuit beyond typical CMOS operation voltage, such as a CMOS based charge pump.
- High feedthrough level: Parasitic elements deteriorate the performance of MEMS resonators. Micro-scale resonators suffer more severely from this parasitic effect as parasitic signal paths that exist between the input to the output electrodes through the substrate, thus leading to an unacceptable level of feedthrough noise level.

This work aims to address most of these issues and propose novel solutions to each of them by using a new technique of combining both piezoelectric and capacitive transducers within a single micromechanical resonator, while retaining the same device designs and materials. The concept of combining both piezoelectric and capacitive transducers in a single lateral-extensional device as dual-transduced micromechanical resonator is introduced in this work to simultaneously achieve high-Q, low motional impedance, and greatly reduced feedthrough parasitics in a hybrid multi-port micromechanical resonator.

1.2 Origin and History of RF MEMS

The concept of the micro-electromechanical (MEM) resonators was introduced in 1967 by Harvey Nathanson in resonant gate transistor for the first time [14]. Because of the growth in material science, it started to be widely studied and used in RF and wireless applications in the late ’90s. Since that, wireless communication systems have become one of the most common discoveries in human history as it changed the way people communicate with others. Wireless communications allowed the connections among systems and the transfer of information to be ubiquitous and convenient for people, unlike the wired systems. Many wireless network

applications have become an indispensable part of our daily life, such as GPS, Wi-Fi, Bluetooth, radio broadcasting, cell phones, mobile tablets, and so on. One of the major applications that people rely on in their daily life is wireless transceivers. The transceivers are designed to have the ability to both transmit and receive signals wirelessly. Researchers have been persistently trying to miniaturize the radio frequency devices while reducing their power consumption and cost to get more advanced devices that meet today's growing demands [15]. Integrating high-quality factor RF passives like quartz crystals to implement oscillators and filters has let these devices to be improved and widely deployed. A wireless transceiver works with devices that have high Q factors to reduce the power consumption and to increase the system robustness [16].

Radio frequency microelectromechanical systems (RF MEMS) are continuing to develop at a rapid rate to achieve higher frequencies and thus pushing the limit for wireless communication devices like switches, tunable capacitors, and resonators to achieve higher frequencies with excellent performance. One of the most critical advantages of MEMS devices is their abilities to be fabricated and integrated with CMOS technology. MEMS resonators are widely used in filters, mixers, oscillators, and RF applications to fulfill the need of high-Q on-chip devices. The micromechanical comb-drive resonator concept was introduced by C. Nguyen and R. Howe more than two decades ago [2]. Comb-drive capacitive electro-micromechanical systems concept is the major building block element for many RF and Microwave's components, filters, and resonators. This capacitive transducer technology has driven the studies of actuators and sensors into various novel applications such as gyroscopes and accelerometers to measure motion in vehicles and game controllers, and BioMEMS devices in disease diagnostics, drug delivery, vital signal sensors, medical implants, molecular diagnostic application, etc. However, one of the key limitations associated with the RF MEMS resonators is their relatively high motional impedance, which can

be a cumbersome bottleneck against the employment of such devices in front-end transceivers due to the large impedance mismatch between the resonators and antennae or other front-end modules. Piezoelectric transducer is a great solution to lower the motional impedance by improving the transduction efficiency to obtain fairly low motional impedances. In particular, thin-film piezoelectric-on-silicon (TPoS) resonators have shown superior performance as compared to their capacitive counterparts [17]. In addition, piezoelectrically transduced TPoS resonators are capable of operating at frequencies up to a few GHz while retaining its performance reliability with low motional impedance and moderate-quality factor [17-18].

On-chip vibrating MEMS resonators have attracted tremendous attention from both the industry and academia as these devices can achieve high resonance frequencies along with high frequency-Q products. So far, these MEMS resonators hold many promises like the ability to reach high-quality factor, while operating at high frequencies and enabling size reduction by several orders of magnitude. Moreover, they are deemed as IC-compatible for on-chip applications integrated with IC electronics such as sensing, signal processing, and wireless communication systems.

1.3 Review of Current State of the Art of Micromechanical Resonators and Filters

Most of current day wireless communications operate at the range of the radio frequencies that are between 30 MHz and 3 GHz or slightly beyond. Tunable radio frequency (RF) filter has attracted the attention of industry due to the growing need for low loss on-chip RF filters operating at very high frequency (VHF) and ultra-high frequency (UHF) ranges. Tunable capacitive RF MEMS filters and RF switches have been reported at high microwave frequencies up to 18 GHz. [19]. However, these RF MEMS filters are not yet suitable for on-chip integration due to the high impedance. Piezoelectric RF MEMS filters such as Surface Acoustic Wave (SAW) and Bulk

Acoustic Wave (BAW) are widely used now as RF and IF filters largely due to their low insertion losses along with other performance benefits. Nevertheless, SAW and BAW piezoelectrically-transduced resonators still have limitations in signal processing to meet some even more stringent performance requirements such as narrow-band filtering due to their low-Q's as compared to that of capacitively-transduced resonators.

1.3.1 Electrostatically-Transduced MEMS Resonators

Capacitively-transduced MEMS resonators have been the subject of several reviews as the needs of higher frequency is becoming a necessity. In 1994, Clark Nguyen developed and promoted the electrostatic comb-drive micro-resonators for signal processing in the low and medium frequency range (i.e., frequencies from a few hundred kHz to 3MHz only) [1]. In order to further increase the frequency range of these micromechanical resonators, flexural-mode of free-free-beam polysilicon resonators were implemented to increase the operating frequency and the quality factor to 300 MHz and 8,400 in vacuum, respectively [2]. Even though free-free-beam resonators performed very well in low MHz bandpass filters applications, free-free-beam resonators are not suitable for applications in the UHF ranges (up to 3 GHz). Scaling down the MEMS geometry structure is necessary to meet the demand by RF front-end transceivers; however, the anchors of the mass body starts to become a major contributor to the energy dissipations as the dimension goes down, which created anchor related energy loss effect that lower the quality factor. As a promising approach to address that, C. Nugyen and J. Wang also introduced a lateral vibrating micromechanical contour-mode disk resonator concept. Unlike free-free beam resonator, this resonator can obtain higher frequencies as its electrostatic force acts laterally on the resonator structure, therefore producing contraction and expansion of the disk-shaped resonator body along its radius, length, or width. Using such a design, a micromechanical resonator can

operate at 156 MHz with a measured Q-factor exceeding 9,400 at atmosphere pressure, while retaining even larger dimensions as compared to free-free beam resonators, which makes it suited for applications at UHF frequencies and beyond [3].

The development of a radial contour-mode micromechanical disk resonator with resonance frequencies up to 1.156 GHz with measured Q's above 2,500 under atmosphere pressure was the most important breakthrough discovery in capacitive resonators reported by J. Wang [4]. J. Wang et al. introduced a self-aligned anchoring stem technique that pushed the performance of radial-contour mode resonators to the next level. In contrast to the traditional anchor refill process that leads to misalignment by the limitation of the lithography alignment tolerance, the self-alignment of supporting anchors to the exact center of the resonator allowed exciting the device to higher-order modes. This novel design helped to reduce the anchor-related mechanical loss dramatically during radial vibration by symmetrically balancing disk-shaped resonators. This allows them to exhibit high-quality factors in both air and vacuum at GHz frequencies while keeping similar power handling ability and same structural dimensions of the previous version of contour-mode resonators. Accordingly, a wine-glass mode disk resonator was implemented to operate at 74 MHz with a high Q's of 8,600 in air and 98,000 in vacuum [5].

Although a very high Q-factor in UHF range has been achieved by contour mode resonators, capacitively driven micromechanical resonators still suffer from the large motional impedance (sometimes > 1 MΩ), which prevent these types of devices from matching with the standard 50Ω RF components. In order to lower the impedance, several strategies have been demonstrated, such as a solid-filled dielectric transducer gap, which relies on replacing the air gap with a solid gap filled with a high-k dielectric to achieve Q's of 3,100 at ~1 GHz and relatively low motional impedance less than 10 kΩ [7]. Another approach is to lower the impedance by

employing nanometer capacitive gap in electrostatically transduced resonators for enhanced transduction efficiency, since the motional resistance is proportional to the fourth power of the resonator-to-electrode gap. However, that will give rise to the increased fabrication cost through unbearable values and also decreases the reliability and reproducibility of those devices. Besides the efforts of lowering the motional impedance of capacitively transduced micromechanical resonators, lots of research towards increasing the operational frequency of such devices has also been in progress. In 2009, a longitudinal-mode silicon acoustic resonator with internal dielectric films was investigated to operate at a UHF frequency of 6.2 GHz along with a Q-factor of 4,277 [7]. However, even with this design of dielectrically-transduced silicon bar-shaped resonator with a 15 nm nitride solid gap, whose permittivity is much higher than that of air, the motional impedance is not drastically improved as compared to devices operating with air gap [2].

With all efforts in pushing the performance of the capacitively-transduced MEMS resonator to the next level, the complexity of fabricating capacitive devices with high yield is still a problem when one tries to shrink the capacitive transducer air gap to sub-100nm to reduce the motional impedance. Another solution for improving the transduction coefficient is by employing piezoelectric transducers with a much higher electromechanical coupling coefficient.

1.3.2 Piezoelectrically-Transduced MEMS Resonators

In contrast to the capacitive transducer, the piezoelectric transduction mechanism offers much higher coupling coefficients that are order of magnitude higher for similar resonator geometry as compared to that of capacitive transducer. Piezoelectric resonator has more efficient electromechanical transduction, which lowers the motional impedance and makes the piezoelectric resonators such as SAW and BAW devices the most dominant technology in the mobile communication market today. Unlike capacitive devices, in which most conductive materials can

be used as device layer (e.g., silicon, polysilicon, doped diamond, metals such as nickel, etc.), piezoelectric devices' working principle rely on the piezoelectric effect that only exists in piezoelectric materials, such as quartz, zinc oxide, aluminum nitride, barium titanate, and lead-zirconate-titanate (PZT). These types of piezoelectric materials deform and induce mechanical strain where charges are generated within the materials in response to an applied electric field. Piezoelectric transducer within a typical MEMS resonator consists of a thin-film piezoelectric transducer sandwiched between metallic electrodes situated on top of a low mechanical loss resonator body made of a substrate material such as silicon or diamond. The top and bottom electrodes are strategically placed to facilitate the coupling between the mechanical strain and the induced electric field. When an AC signal is applied, the polarity of the piezoelectric film is affected and the indirect piezoelectric effect takes place, where the electrical AC signal matches the natural frequency of the piezoelectric thin film and causes the film to mechanically deform and vibrate in a certain mode shape. This mechanical deformation will excite the acoustic waves to be converted back to the electrical signal or direct piezoelectric effect through the output electrodes, where it can be detected.

Surface Acoustic Wave (SAW) and the Bulk Acoustic Wave (BAW) are the two most important classes of piezoelectric resonators at the present day. SAW and BAW devices have already been widely used in filters in RF front-ends and a wide variety of sensor applications. SAW resonators can be used not only for filters but also for oscillators and sensors. SAW resonators use a pair of two metallic electrodes known as interdigital transducers (IDT) on the surface of the piezoelectric film layer or substrate to perform the transduction in the acoustic domain. These electrodes are interlocking with each other as comb-shaped electrodes that are used to generate and detect the acoustic waves at resonance as the energy converted between electrical

and mechanical domains. When an AC signal is applied, acoustic wave energy will be confined on the device surface regardless of its thickness with the help of the reflector electrodes. Basically, one of the electrodes initiates the SAW wave propagation, and the other electrode reflects it. SAW resonators have two configurations. One-port SAW resonators use single IDTs, and its typical applications are in oscillators. Two-port SAW resonators use double IDTs, and its typical applications are in filters. The resonance frequency depends on the piezoelectric acoustic velocity and the pitch distance, which is setting the wavelength of the resonator. SAW resonators are widely used in filters applications, where frequencies are lower than 2 GHz. However, as current mobile applications kept on pushing for frequencies higher than 2 GHz, such SAW devices reached its limit, and it becomes very difficult to implement low-loss and sharp-cut off filters using SAW devices. The Q-factor drops dramatically as the frequency reach 3 GHz for a SAW resonator, as scaling down the interdigital transducer pitch size to sub-micron scale becomes quite challenging and require nonstandard fabrication techniques like electron-beam lithography.

BAW resonators often consist of a piezoelectric material sandwiched between the top and bottom electrodes. Unlike the surface acoustic wave (SAW), the waves are propagated and traveled from the surface through the bulk of the piezoelectric layer to the other parts of the hosting substrate. Due to its simple electrode design, filters based on BAW resonators have attracted lots of attention from both academia and industry since they were first implemented in 1980 by Lakin et al. [8]. BAW resonators provide higher quality factor at high-frequency range and a sharp cut-off frequency characteristic highly desirable for filters. Furthermore, it is possible to implement monolithic filters alongside active RF components like transistor-based amplifiers and mixers. There are two types of implementation of BAW filters that both have been successfully commercialized in the wireless communication market at the moment. One is the solid mounted

resonator (SMR), which uses Bragg reflectors as a method of isolation from the carrier substrate by leveraging layers with mismatched acoustic impedance; and the other is the film bulk acoustic resonator (FBAR) in which the resonator structure isolated from the carrier substrate via an air cavity suspension to generate the high impedance mismatch for the sake of retaining acoustic energy in the resonator body [9]. Since the frequency of BAW devices is determined by piezoelectric film thickness, the thickness of the piezoelectric film must be accurately controlled to achieve precise target frequencies. Moreover, only one frequency can be designed on a single chip by one single process run without post-process thickness trimming. Thus, single-chip multi-frequency selective filter array cannot be fabricated on the same substrate without the usage of post-process thickness trimming. Nevertheless, the present-day wireless technology calls for multi-functional single-chip transceivers that operate at different frequencies as opposed to several discrete components integrated on the board level. Furthermore, because BAW resonators require multiple layers, the microfabrication of these devices tends to be quite cumbersome. Moreover, only moderate Q factors can be achieved due to the relatively high losses of its piezoelectric transducer layer.

In order to relieve and suppress this issue, similar to the evolution of capacitively-transduced counterparts, newly developed contour-mode resonators were developed to expand the major advantage of FBAR (i.e., high Q-factor at high frequencies and low motional impedance) to achieve multiple frequencies on a single chip as the resonance frequencies of piezoelectrically transduced lateral extensional contour-mode are determined by the lithography-defined lateral dimensions rather than the thickness of the piezoelectric layer. Piazza et al. has demonstrated multiple AlN resonators with operating frequency ranging from 23 MHz to 230 MHz together with Q-factor up to 4,300 in air and low motional impedances ranging from 50 Ω to 700 Ω [10]. These

devices were also electrically cascaded in ladder network configuration yielding high performance and low loss (I.L. ~ 4 dB at 93 MHz) and high rejection bandpass filters for 236 MHz resonators. Thin-film piezoelectric on substrate (TPoS) resonator device is a new technology that has the advantage of combining piezoelectric materials with low acoustic loss structural layer (often referred to as a substrate). This type of resonator solves the restriction of piezoelectric resonators on operating frequencies because of its dependency on the material properties. Using piezoelectric material by itself as the resonator body structure in the piezoelectric device is the reason for the low Q-factor due to the relatively high acoustic losses [60]. The material advantages, such as the high mechanical coupling coefficient of piezoelectric devices, come with a drawback in limited achievable Q's. A mechanical resonator's operating frequency is highly dependent upon the resonator body structural material's Young's modulus and density, which set the acoustic velocity. Unfortunately, as mentioned before, there are limited kinds of material suitable for piezoelectric resonators, which restricted the development of such technology in the higher frequency region. In order to solve this problem, another lateral extensional resonator, thin-film piezoelectric-on-substrate resonator (TPoS), has been proposed and demonstrated [11]. A typical thin-film piezoelectric-on-substrate (TPoS) MEMS resonator consists of a thin-film piezoelectric transducer sandwiched between two metallic electrodes situated on top of a low mechanical loss resonator body made of a substrate material such as silicon or diamond. By taking advantage of piezoelectric transduction and a low loss mechanical structure, thin-film piezoelectric transducers have demonstrated higher electromechanical coupling coefficients when compared to that of the capacitive transducers, while holding slightly higher material related losses. Therefore, the introduction of a low loss structural material such as silicon to define the TPoS resonator body for storing acoustic energy has shown great promises to exhibit low acoustic losses (high-Q's) and

low motional impedances due to the high electromechanical coupling of piezoelectric transducers, which have shown superior performance as compared to their capacitive counterparts. The TPoS resonator has been utilized to fabricate multi-frequency UHF filters within a single substrate by a single fabrication run. The piezoelectrically transduced TPoS resonators are capable of operating at frequencies up to a few GHz (at frequencies ranging from 600 MHz to 3.5 GHz with motional resistance less than 700 Ω) and retaining its performance reliability. This integration of a silicon layer and the high electromechanical coupling of the piezoelectric layer would result in such a mechanical resonator that has a fairly high Q factor and a very high frequency (VHF) range of operation frequency. In this combination, the energy of the device will dissipate more efficiently by the low damping coefficients of the coupling layer.

1.3.3 Summary of Current State of the Art

Capacitively-transduced micromechanical resonators and filters based on lateral extensional contour-mode resonators can undoubtfully achieve higher quality factors as compared with piezoelectric counterparts. However, capacitive resonators regrettably suffer from high insertion loss, which prevents these types of devices from matching with the standard 50 Ω RF components due to its high motional impedance. Even though a great deal of efforts has been made to achieve nanometer capacitive gap in electrostatically transduced resonators to achieve an enhanced electromechanical coupling coefficient, the employment of nanogap capacitive transducers also gives rise to higher fabrication cost, lower yield, poorer reliability and reproducibility of those devices when compared to is piezoelectric counterparts. On the other hand, in order to have integration between capacitive MEMS resonators and CMOS circuity, the fabrication process needs to be with standard semiconductor processing materials and equipment. Till today, FBAR and SAW piezoelectric resonators have already reached a phase of maturity. For

more than one decade, they have already been produced in large volumes and used in mass-produced commercial electronics products. However, as current mobile communication keeps on pushing for higher and higher frequencies, SAW devices have reached its limit. Moreover, the performance of these devices still relies on the mechanical and electrical properties of the piezoelectric layer, which limits the freedom of design. Although TPoS resonators have incorporated low loss structural material to define the TPoS resonator body for storing acoustic energy, which has shown great promises to exhibit low acoustic losses (high-Q's) and low motional impedances, the same method also partially sacrifices its electromechanical coupling.

1.4 Dissertation Organization

This work focuses on combining both capacitive and piezoelectric transduction mechanisms into one hybrid resonator to achieve a new type of micro-mechanical lateral extensional resonator that maintains all benefits of both capacitive and piezoelectric resonators while having small motional resistance and low insertion loss. This work is structured as follows: Origin and history of RF MEMS and reviews the current state of the art of MEMS resonators will be described in Chapter 1; Chapter 2 and 3 discuss the two mechanisms of transduction (piezoelectric and capacitive); Chapter 4 presents the localize annealing study in detail; Chapter 5 describes the newly developed processing techniques for microfabrication of the newly proposed hybrid resonator configuration; Micromechanical filters based on hybrid arrays are discussed in detail in Chapter 6; Finally, Chapter 7 presents the conclusions and the future work.

Chapter 2: Piezoelectric Transducer

Electrostatically and piezoelectrically-transduced resonators share almost the same working principles. However, two different types of driving mechanisms are used in these resonators. In both types of resonators, the goal is to drive the mass body into a strategically designed resonance mode. The vibration resonator body system is excited into a resonance mode by supplying mechanical forces that match the mechanical structure's natural resonance frequency and mode shape. For piezoelectric resonator, the mechanical excitation is provided through piezoelectric material itself. As we apply an electric field to the piezoelectric thin film layer, the film is then deformed accordingly, which causes behavior that is called the piezoelectric effect. As the applied sinusoidal electric field matches the natural resonance frequency of the resonator body, the structure is then driven into its resonating mode. On the other hand, capacitive resonator still operates the same way by driving the resonator body, which is usually a conductive material, into its natural resonance mode. However, capacitive resonators do not have the built-in piezoelectric effect characteristic similar to their piezoelectric counterparts. Therefore, for a capacitive resonator, it is required to apply external electrostatic force to provide the necessary mechanical excitation to drive the resonator mass body into resonance mode while also detecting and converting the generated vibration into an output electric signal.

In this chapter, detailed discussion with regards to the piezoelectric effect, piezoelectric transducer material, mathematical model of MEMS resonators, lateral extensional contour-modes, operating principle of MEMS resonators, and material properties of piezoelectric materials will be presented.

2.1 Piezoelectric Effect and Mathematical Modeling

Piezoelectricity was first discovered by brothers Pierre Curie and Jacques Curie in 1880. Later in 1916, the piezoelectric effect was used in the ultrasonic sensor for submarine ultrasound detection by Paul Langevin using the piezoelectric quartz element. After that, several applications based on the piezoelectric effect have been widely accomplished, such as sensors, microphones, transducers, and oscillators, which became the breakthrough for the radio-telecommunications industry. The piezoelectric effect is defined as the linear electromechanical interaction between electrical and mechanical systems in crystalline materials with no inversion symmetry. Piezoelectric materials are able to generate an electrical charge when external mechanical stress (force) is applied to it. The reason for that to happen is because the internal electric polarization from piezoelectric materials is perturbed by mechanical means, and an electrical response is generated because of the induced dielectric displacement. The amount of mechanical deformation and the electric discharge is directly proportional to the strength of both the electric field and the mechanical perturbation on the piezoelectric material. This behavior is known as the direct piezoelectric effect. Conversely, the converse piezoelectric effect appears when the mechanical deformation is generated by an applied electric field across the piezoelectric materials. The mechanical deformation is directly proportional to the strength of the electric field and to the equivalent acoustic velocity (V_{eq}) within the piezoelectric material layer. The mechanical deformation during resonance directly affects the internal electric polarization of the piezoelectric layer, thus resulting in an electrical response known as the direct piezoelectric effect that can be extracted via the output current i_0. The piezoelectric effect can be described by:

$$T = c^E \cdot S - e \cdot E \qquad (1)$$

$$D = e \cdot S + \varepsilon^S \cdot E \qquad (2)$$

where T, S, D, and E represent the stress, strain, electric displacement, and electric field, respectively. Also, c^E is the elastic stiffness at a constant electric field, e is the piezoelectric constant, and ε^S is the permittivity at a constant strain.

As mentioned before, the device consists of a structural layer that can be silicon or any other low acoustic loss structural material. The equivalent acoustic velocity can be found by:

$$V_{eq} = \sqrt{\frac{E_1T_1 + E_2T_2 + \cdots + E_nT_n}{(\rho_1T_1 + \rho_2T_2 + \cdots + \rho_nT_n)(1-\sigma^2)}} \quad (3)$$

where n is the number of the stacked layers; T is the thickness of each material; E, ρ, and σ denote the Young's Modulus, density and Poisson's ratio of the stacked resonator structural materials.

2.2 Contour-Modes in MEMS Resonators

The contour and lateral extensional mode mechanical resonant frequencies are governed by the material properties and by a characteristic lateral dimension either the radius of the disk or the width/length of the square or rectangular plate. Neglecting non-linear behaviors caused by anchors or material uncertainties, the resonant frequency can be approximated by the following governing equations:

$$\omega_{0,plate} = 2\pi f_0 = \frac{n\pi}{l}V_{eq} \quad (4)$$

$$\omega_{0,disk} = 2\pi f_0 = \frac{\alpha_n 2\pi}{R_{disk}}V_{eq} \quad (5)$$

where n and α are the frequency scaling factors, and l and R_{disk} are the length and the radius of the resonator. In this work, fundamental to higher resonant modes was explored with the following α_n values for the first four fundamental lateral-extensional contour modes: α_1= 0.272, α_2= 0.342, α_3= 0.418, α_4= 0.493. The α_n approximations are presented in this sequence after a COMSOL® FEM

simulation for extensional contour modes using estimated equivalent acoustic velocity (V_{eq}) values from fabricated devices using (3).

By having only two support anchors with strategically-designed dimensions, the acoustic energy losses leaked through the anchors have been effectively minimized. In order to excite the wine-glass mode while minimizing the anchor related losses, the supporting tethers should be placed at the quasi-nodal locations, where the resonator plate does not have any radial displacement, as illustrated in Figure 2.1.

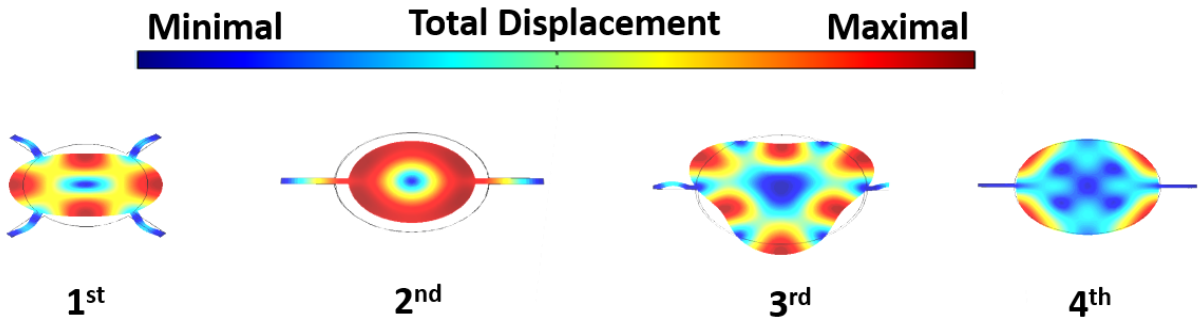

Figure 2.1 – Anchors design approaches for the first four fundamental lateral-extensional contour modes show anchors locations using the FEM COMSOL Multiphysics® modal analysis model.

2.3 RF MEMS Resonator Equivalent Electrical Circuit Model

Despite the geometry design or the mode of actuation, resonators behave like electrical devices at the resonance when looking into their ports. The resonator can be modeled by an electrical series LCR equivalent circuit derived from a mechanical model composed of a rigid-body mass attached to a grounded base through spring and damper elements, as shown in Figure 2.2 (a), (b) and (c), accordingly.

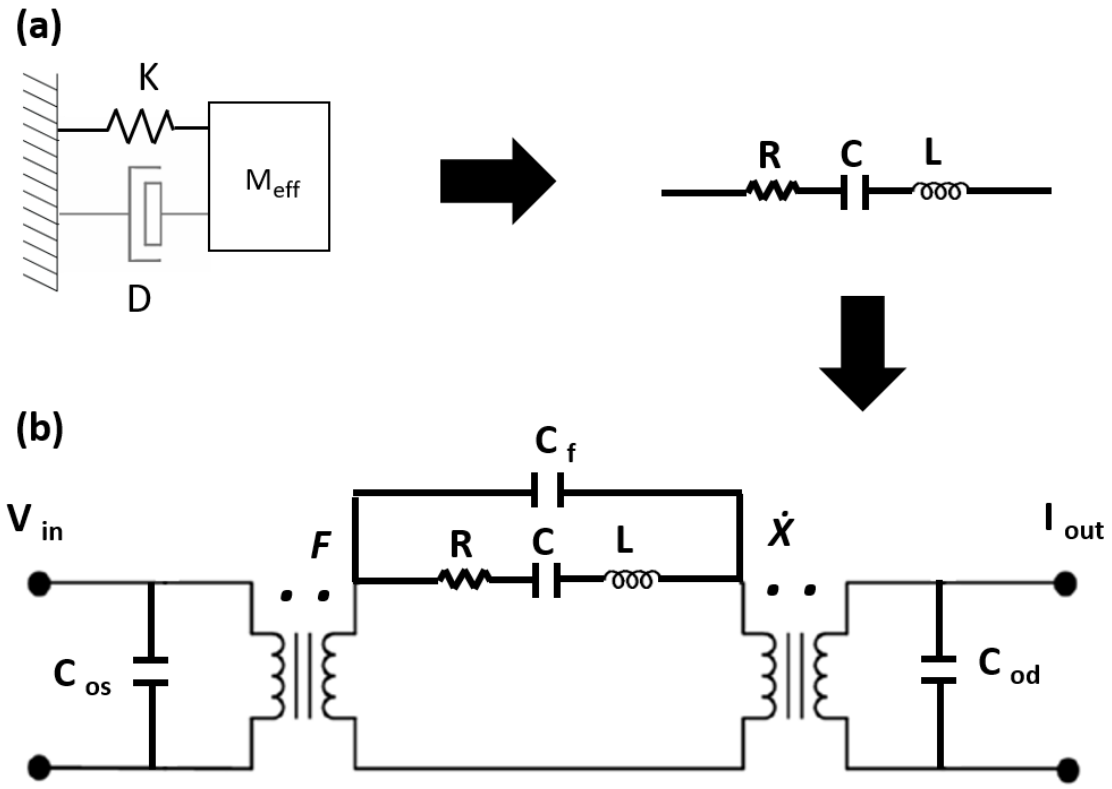

Figure 2.2 – Illustration of the equivalent circuit model for a MEMS resonator, including (a) mechanical equivalent model; (b) electrical circuit models; (c) a complete electromechanical model of the resonator.

The mechanical to the electrical analogy between the respective elements of the two equivalent models as can be seen in Figure 2.2 are correlated as the following:

$$\text{Inductance } (L_m) = MAss\ (M_{re}) \quad (6)$$

$$\text{Capacitance } (C_m) = Compliance\ (K_{re}^{-1}) \quad (7)$$

$$Risistance\ (R_m) = Dampimg(C_{re}) \quad (8)$$

$$Voltage(V) = Force(F) \quad (9)$$

$$\text{Current}(I) = Velocity\ (v) \quad (10)$$

In the two-port resonator, two transformers represent the ports and isolation between the input and output electrodes. The capacitors C_{od} and C_{os} represent the static capacitances of the driving and sensing pads between the electrodes and the device layer, accordingly. The substrate

feed-through capacitance C_f accounts for the RF signal leakage between the input and output electrodes/ports. The platform rigid dynamic elements are derived as follow:

$$L_m = \frac{M_{re}}{\eta_{re}^2} \tag{11}$$

$$C_m = \frac{\eta_{re}^2}{K_{re}} \tag{12}$$

$$R_m = \frac{\sqrt{M_{re}K_{re}}}{Q\eta_{re}^2} \tag{13}$$

where Q is the Q- factor, M_{re} is the equivalent dynamic mass, K_{re} is the equivalent spring stiffness, and η_{re} is the equivalent electromechanical coupling. The M_{re} and η_{re} are geometry dependent; they can be approximated for either disk or plate resonators by the following expressions:

$$\eta_{r,disk} \approx E_n d_{31} \pi \frac{1}{2} \tag{14}$$

$$\eta_{r,plate} \approx 2E_n d_{31} l \tag{15}$$

$$M_{re,disk} \approx \frac{2\pi\rho_n t_n \int_0^{R_{disk}} r J_1^2\left(\frac{\omega_o}{V_{eq}} r\right) dr}{J_1^2\left(\frac{\omega_o}{V_{eq}} R_{disk}\right)} \tag{16}$$

$$M_{re,plate} \approx \frac{\rho_n t_n A}{2} \tag{17}$$

where d_{31} and J_1 are the transversal piezoelectric strain coefficient and the Bessel function of the first kind, respectively.

2.4 Thin-Film Piezoelectric-on-Silicon (TPoS) Resonators

Thin-film piezoelectric transducers have demonstrated higher electromechanical coupling coefficients when compared to the capacitive transducers, while holding slightly higher material related losses. TPoS resonators take advantage of the combination of low acoustic loss structural layers such as silicon with the high electromechanical coupling piezoelectric materials. Therefore,

the introduction of a low loss structural material such as silicon to define the TPoS resonator body for storing acoustic energy has shown great promises to exhibit low acoustic losses (high-Q's) and low motional impedances due to the high electromechanical coupling of piezoelectric transducers. Previously investigated TPoS devices have reported high-Q factors with a diverse number of resonant frequencies using SOI wafers as the starting substrate. Technologies developed from SOI substrates, especially TPoS, are very attracting because it helps minimize the number of fabrication steps and maximizes the yield of single crystal silicon devices. As seen in Figure 2.3, a typical thin-film piezoelectric-on-substrate (TPoS) MEMS resonator consists of a thin-film piezoelectric transducer sandwiched between two metallic electrodes situated on top of a low mechanical loss resonator body made of a substrate material such as silicon or diamond. The resonance frequency of ZnO-on-Si resonators depends highly on the effective acoustic velocity of the device structure that consists of a stack of thin-film ZnO piezo-layer and a Si structural layer. This combination results in mechanical resonators with moderate to high Q factors and very high to ultra-high resonant frequencies. The single crystal silicon has a much higher acoustic velocity as compared to that of sputtered piezoelectric ZnO thin film. When an AC actuation signal is applied across the piezoelectric film between the top and bottom electrodes, not only the piezoelectric thin film is engaged in resonating, the silicon device layer underneath is also excited into resonance mode as well, which will drive the Si resonator body to expand and contract through the converse piezoelectric effect. Reciprocally, the body's physical deformation induces periodic piezoelectric charges detected by the output electrodes.

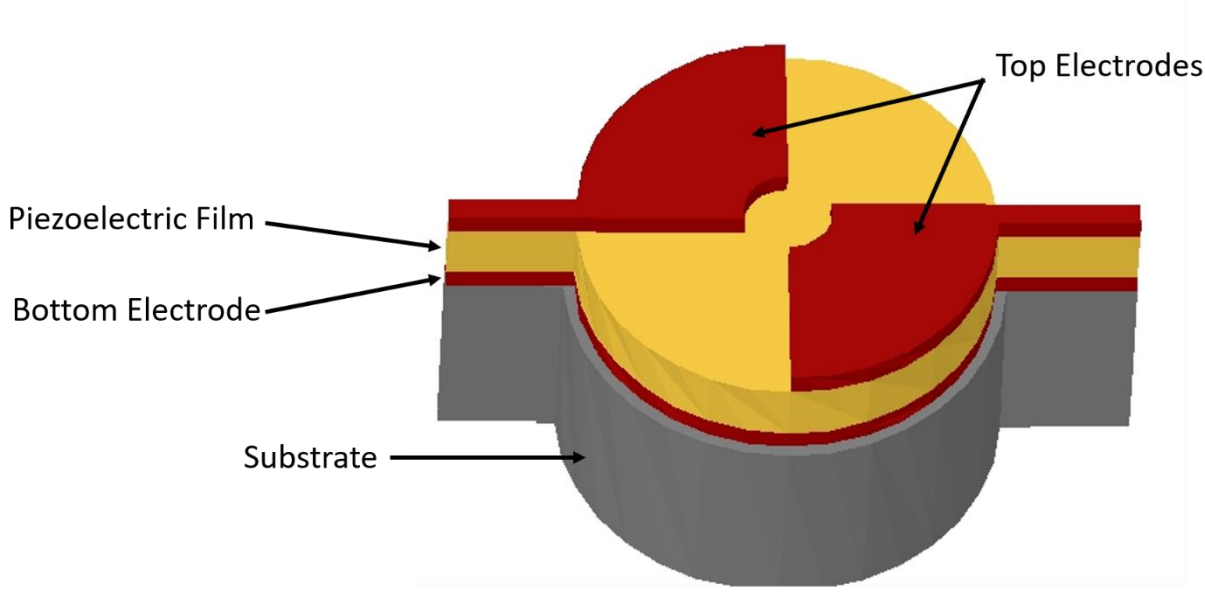

Figure 2.3 – Schematic illustration of electrode and anchor design configurations for a thin-film piezoelectric on substrate (TPoS) disk resonator that is designed for 1st lateral extensional contour mode.

2.5 Piezoelectric Materials

There are two major categories of piezoelectric characteristics: piezoelectric crystal and ceramic. For most MEMS applications, piezoelectric ceramics is a better choice as they can be integrated with CMOS devices due to their relatively low deposition temperature below 300 ^{o}C [20]. There are many types of piezoelectric ceramics, such as zinc oxide (ZnO), aluminum nitride (AlN), barium titanate ($BaTiO_3$), and Lead-Zirconate-Titanate (PZT). Properties of the most widely used piezoelectric ceramics materials are shown in Table 2.1. Barium titanate is an excellent choice for electromechanical transducers due to its high electromechanical coupling coefficient and ease of fabrication. However, it is suffering from a high thermal expansion coefficient and low Curie point, which limited its further development. On the contrary, PZT has rapidly taken the places of barium titanate in most off-chip piezoelectric applications, as PZT gives the highest piezoelectric coupling coefficients (~30x higher than those of AlN and ZnO) and low thermal expansion coefficient. In addition, PZT ceramics are ferroelectric and do not require

specific deposition processing in order to obtain high piezoelectric coefficients. However, PZT also undesirably has high permittivity (high acoustic losses), which hinders its usage for high frequency applications.

So far, AlN and ZnO are the most commonly used piezoelectric thin film materials for MEMS resonator applications due to their relatively low temperature deposition conditions and their decent electromechanical coupling and permittivity. High quality AlN and ZnO films can be obtained by RF sputtering at a relatively low temperature below 300 ^{o}C, which enables a post-IC-compatible process for CMOS integration while retaining aluminum as the standard metallization layer. Accordingly, in order to have high piezoelectric electromechanical coupling coefficients, particular fine-tuning of deposition and annealing conditions are required. AlN has low acoustic losses and the highest acoustic velocity as compared with those of both ZnO and PZT. Besides, AlN does not get attacked by HF, which make it easier to be fabricated alongside with capacitive devices, which require releasing of the SiO_2 gap layer by HF. However, to etch AlN, it requires a Cl_2-based reactive ion etching process, which is currently unavailable at USF.

On the other hand, ZnO has a very good electromechanical coupling coefficient. However, ZnO does not hold nearly as good acoustic-wave properties, by showing relatively high acoustic energy dissipations and low acoustic velocity when compared with AlN. In addition, ZnO offers a high deposition rate of 100nm/hr and an available dry etching recipe that requires CH_4/Ar through inductively coupled plasma etching (ICP) process, which makes it the only piezoelectric material that can be used in this work.

Table 2.1 – Properties of the most widely used piezoelectric ceramics materials [12, 13].

Material	ZnO	AlN	PZT
Density (kg/m^3)	5676	3260	7600
Dielectric Constant	8.8	8	400-1000
Elastic Modulus (GPA)	123	330	53
Poisson Ratio	0.18-0.36	~0.24	0.25-0.31
Relative Permittivity	9-11	8-10	400-1900
Electrical Resistivity	10^8 -10^9	10^{10} -10^{14}	10^7-10^9
Acoustic Velocity [m/s]	4655	10400	3300
Piezoelectric Coefficient d31 [pC/N]	-4.7	-1.8	-130
Temperature Expansion Coefficient	4.0 × 10^{-6}/°C	4.5 × 10^{-6}/°C	-6.0× 10^{-6}/°C

2.6 ZnO Thin Film Piezoelectric Transducer Characterization

There is a strong correlation between the degree of c-axis orientation and the value of the d_{31} piezoelectric coefficient. Therefore, in order to get a high transverse piezoelectric coefficient d_{31}, it is important to obtain a good quality (002) c-axis oriented ZnO thin-film with densely packed columnar structures. The quality of the ZnO film is critical and important to achieve the highest performance for ZnO resonators. In this work, piezoelectrically-transduced contour-mode resonators and filters will be fabricated; therefore, highly c-axis orientated ZnO films are highly desirable. Lateral extensional contour-mode resonators vibrate with in-plane motions through the orthogonally applied electrical field through the piezoelectric transducer layer.

After many studies and characterization of sputtered ZnO films, three key process parameters need to be optimized to achieve good quality films, which are substrate temperature, oxygen concentration, and post-deposition annealing. For all these different studies, the chamber pressure was set to 5 mTorr, and the RF power was held at 80 W. Although ZnO is sputtered directly through ZnO sputtering target, an oxygen environment is needed as reactive gas in the sputtering chamber during ZnO deposition to ensure an oxygen-rich ZnO film is produced. The ZnO molecule will dissociate into zinc and oxygen atoms in a reactive sputtering deposition after leaving the sputtering target, thus creating free zinc and oxygen atoms because some of the free zinc atoms will not recombine with oxygen, leaving an excess of Zn on the deposited piezo-transducer thin film. The effects of different Ar: O_2 gas flow ratios have been studied, and it was found that ZnO films have grown in a 1: 1 ratio of Ar: O_2 environment exhibit the strongest (002) crystalline orientation (strong dielectric effect). On the other hand, when the oxygen ratio is increased, it shows degradation in quality. Likewise, as the oxygen ratio decreases, the dielectric effect becomes weaker, and the ZnO film becomes conductive.

Also, the substrate temperature plays an important role in determining the quality of the RF sputter-deposited ZnO films because it helps the deposited ZnO film to achieve its piezoelectric crystal characterization. As the temperature was set to 300 ^{o}C, the ZnO film shows the highest intensity peak implying that ZnO sputtering at 300 ^{o}C condition leads to better c-axis orientation as compared to that of RF sputter deposited thin film at higher or lower temperatures. At lower temperatures, it shows degradation in the quality as the dielectric effect becomes weaker. Likewise, at higher temperatures, the intensity of ZnO film decreases gradually but maintains the same order of magnitude. Finally, post-deposition annealing at 400 ^{o}C for one hour with the Ar and O_2 flow is important, which helps the deposited ZnO film to achieve its piezoelectric crystal

characterization and to improve the c-axis orientation of ZnO as evident from the rocking curve measurements. This improvement of the c-axis orientation translates to better transduction efficiency from the ZnO layer that could result in lower insertion loss and higher-Q.

Chapter 3: Fabrication Process of Capacitive Transducer

Portions of this chapter including figures have been previously published [50]. Permissions are included in Appendix A.

Motional resistance is one of the most important performance metrics for high-quality factor, low power, and CMOS-compatible capacitively transduced vibrating micromechanical resonators. The motional resistance is primarily set by the electrode-to-resonator air gap that can be formed by deep reactive ion etching (DRIE) process. Although the state-of-the-art DRIE technologies can achieve a narrow capacitive air gap down to 1μm or less, the effective gap tends to be larger than designed values due to the sidewall roughness known as scalloping. Systematic modifications of all key process parameters are presented in this chapter for lowering the sidewall roughness to result in an up to 2x reduction of the effective capacitive transducer gap, which could lead to an up to 16x decrease of the effective motional resistance. In this chapter, the development of capacitive resonators is discussed. Firstly, the capacitive transducer model is presented. Secondly, a process optimization method to improve the sidewall smoothness is adopted to reduce the sidewall scalloping that's generated by a Bosch silicon DRIE process. After that, the fabrication tools that were used in the capacitive resonator fabrication process, including Atomic Layer Deposition (ALD), chemical mechanical polishing (CMP), and Nickel Electroplating, are illustrated in details. Finally, the process of fabricating capacitor resonators built on Silicon-on-Insulator (SOI) wafers is presented and explained in detail.

3.1 Capacitive Transducer

A capacitively-transduced MEMS resonator consists of a membrane surrounded by inputs and outputs electrodes separated by a small capacitive gap. Normally, the resonance frequency of any resonator that can be modeled as a spring-mass-damper can be expressed as:

$$F_0 = \frac{1}{2\pi} \times (K_{eq}/m_{eq})^{-1} \qquad (18)$$

where K_{eq} is the equivalent spring constant, and m_{eq} is the mass of the resonator structure. A wine glass mode disk resonator consists of four supporting beams located at its quasi-nodal points. When a bias voltage is applied to the electrodes, electrostatic force (F_{elec}) is generated (mechanical force) in the form of a parallel plate gap between the resonator body and the electrodes. The potential formed is similar to a parallel plate capacitor, and it is illustrated in (19):

$$\mathrm{Q} = \mathrm{V} \times \mathrm{C} \qquad (19)$$

where Q is the total charge existing within the capacitor, and V is a constant polarization DC voltage in the gap area. C is the capacitance between the electrodes and the resonator body can be calculated (based on parallel-plate approximation) as:

$$C = \frac{\epsilon_0 \times \mathrm{A}}{\mathrm{g} + \mathrm{x}} \qquad (20)$$

where ϵ_0 is the gap dielectric permittivity, x is the lumped displacement of the resonator body, A and g are the overlap area and the gap between the resonator disk and the electrodes, respectively.

When an AC signal is applied, the potential becomes time-variable, and the gaps behave like a variable capacitor. Consequently, this variable behavior generates an electrostatic force that at the right frequencies drives the membrane to its natural resonant frequency, therefore inducing an output current that can be detected from output electrodes. The result of applying the differentiation with respect to time to the total charge equation is given by:

$$i_{out} = \frac{dQ}{\mathrm{dt}} = \frac{V_P \times \mathrm{dC}}{\mathrm{dt}} = \frac{\mathrm{V}_P \times \mathrm{dC}}{\mathrm{dx} \times w_0 \times \mathrm{x}} \qquad (21)$$

$$F_{electrodes} = \frac{dC \times V_P \times V_i}{\mathrm{dx}} = \frac{\epsilon_0 \times \mathrm{A} \times V_P \times V_i}{\mathrm{g} + \mathrm{x}} \qquad (22)$$

where dC/dx is the integrated change in electrode-to-resonator body overlap capacitor per unit displacement, V_i is the input voltage amplitude and ω_0 is the radian resonance frequency that equals $2\pi f_0$.

By applying a DC bias voltage, the motion of the resonator is impeded by the generated force, which therefore reduces the equivalent spring constant of the resonator structure by a certain value of $K_{electrode}$, that expressed as:

$$k_{electrode} = \frac{dF_{electrodes}}{\mathrm{dx}} = \frac{\epsilon_0 \times \mathrm{A} \times V_P \times V_i}{\mathrm{g} + \mathrm{x}} \quad \mathrm{x} << \mathrm{g} \qquad (23)$$

The nominal resonance frequency of the resonator structure will be changed by the effect of the spring softening to be expressed as:

$$f = \frac{1}{2\pi} * \left(\frac{K_{eq} - K_{electrodes}}{m_{eq}}\right)^{-1} = \mathrm{f}_0 \left(\frac{1 - K_{electrodes}}{K_{eq}}\right)^{-1} = \mathrm{f}_0 \times 1 - \left(\frac{\epsilon_0 * \mathrm{A}}{K_{eq} * g^3}\right) * V_P \times V_i, \mathrm{x} << \mathrm{g} \ (24)$$

This expression shows that the performance of capacitive resonators heavily depends on the DC bias voltage. A capacitively-transduced resonator is comprised of suspended supporting beams and input/output capacitive transducers with an air gap between the body of the resonator and the surrounding electrodes, including the input (driving) electrode and the output (sensing) electrode. In order to excite the device, an alternating AC signal in the form of an excitation voltage vi is applied to the input electrode to generate a variable potential, which triggers a sinusoidal electrostatic force. Once the frequency of the input excitation AC voltage matches one of the resonance frequencies of the side-tether supported the resonant body of the device. This effect is closely related to a time-varying parallel plate capacitive transducer. The output motional current

(i_0) can be sourced out from the output electrode after applying a DC-bias voltage V_p, which not only generate an electrostatic force at the input transducer to drive the resonator to modal vibration at its resonance mode but also generate an output motional current from the time-varying output capacitive transducer with a DC bias voltage applied.

3.2 Improvement of Deep Reactive Ion Etching Process for Motional Resistance Reduction of Capacitively Transduced Vibrating Resonators

Recent advents of high-Q, ultra-high-frequency (UHF) vibrating micromechanical resonators make them viable on-chip alternatives that could lead to a paradigm shift in future wireless transceivers. Among all actuation and sensing mechanisms, capacitive transducers hold the highest performance potentials in terms of quality factor, power consumption, IC compatibility, and spurious mode suppression [24-29].

The key remaining issue of capacitively transduced resonators is their relatively large motional resistance (R_m), which is too high to be directly coupled with the other RF front-end devices given as [30-32]:

$$R_m = \frac{K_{re}}{\omega_0 Q V_P^2} \cdot \frac{d_0^4}{\varepsilon_r^2 \varepsilon_0^2 A_0^2} \qquad (25)$$

where K_{re}, ω_0, Q, V_P, ε_r, ε_0, d_0, and A_0 represent equivalent stiffness, resonance frequency, quality factor, bias voltage, relative permittivity, vacuum permittivity, electrode-to-resonator air gap, and overlap area, respectively. Among them, the electrode-to-resonator air gap spacing largely affects the motional resistance of a fourth-power dependence.

There were many prior reports on lowering the motional resistance [33-36]. One of the fabrication techniques is deep reactive ion etching (DRIE) that is capable of producing anisotropic and high aspect ratio capacitive air-gap transducers. DRIE is also known as Bosch process with alternating etch and deposition cycles to create etched sidewalls of cyclic roughness (scalloping),

thus leading to increased gap spacing and degraded electrode-to-resonator capacitive transducer efficiency. In this work, optimization of the key process parameters was explored to reduce DRIE sidewall scallops of a capacitive air-gap transducer, as shown in Figure 3.1.

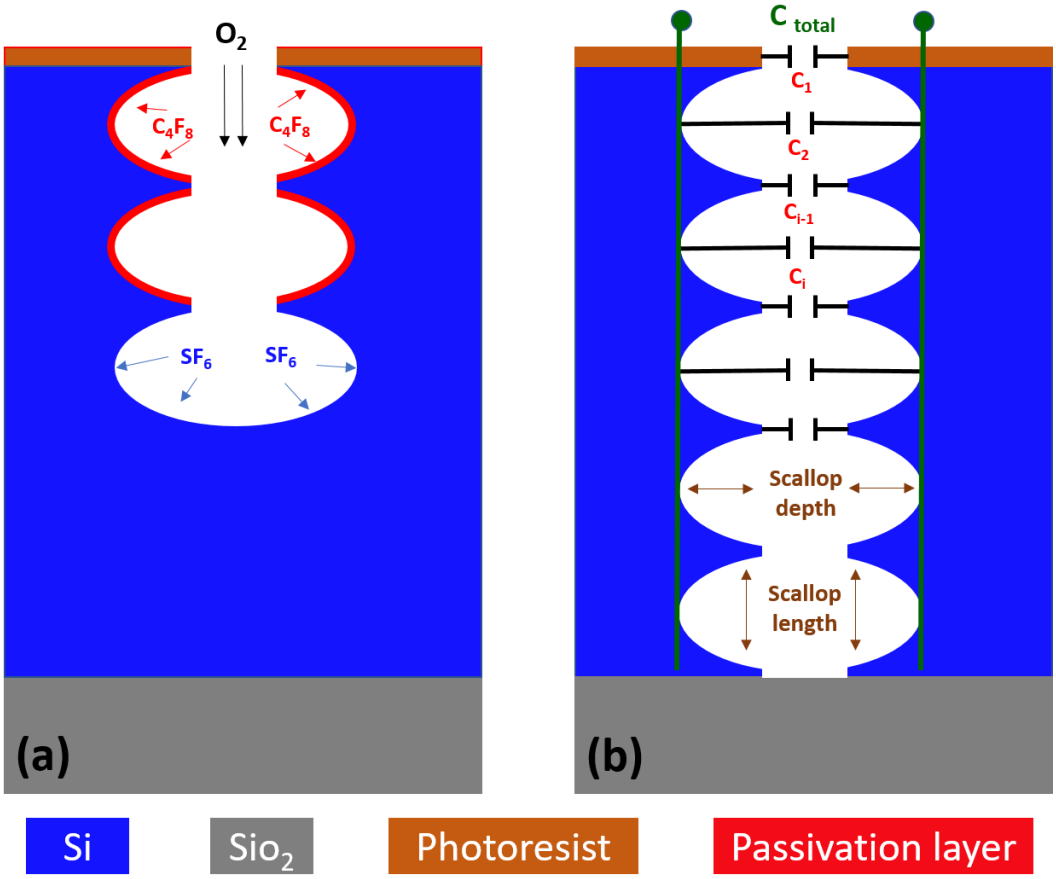

Figure 3.1 – (a) Etching step: Fluorine-based Si isotropic etching with passivation step: a conformation deposition of a Teflon-like material for protection of the etched sidewall results in a sidewall profile with key scallop dimensions specified. (b) Illustration of distributed and total capacitance of a capacitive air-gap transducer including an air-gap with a known DRIE scalloping and its equivalent circuit model.

Formation of narrow (sub-1μm) electrode-to-resonator capacitive gap by an inductively coupled plasma (ICP) etcher can be fulfilled by a time multiplexed deep etching (TMDE) technique also known as the Bosch or DRIE process that is widely used due to its high etch rate, high selectivity, and great sidewall anisotropy. SF_6 is a typical plasma etchant for silicon dry etching through released fluorine-free radicals.

Silicon etches rate depends on both the number of free F radicals and the total area of exposed silicon. Fluorine-based silicon dry etching at temperatures higher than -15°C (not under cryogenic etch condition) is known to be isotropic. Hence, there is a need for special chemistry, such as C_4F_8, to protect the etched sidewalls as it can react with silicon to form a Teflon-like protection layer. Alternative cycling of C_4F_8/O_2 and SF_6 is what makes DRIE an anisotropic etch, as seen in Figure 3.2.

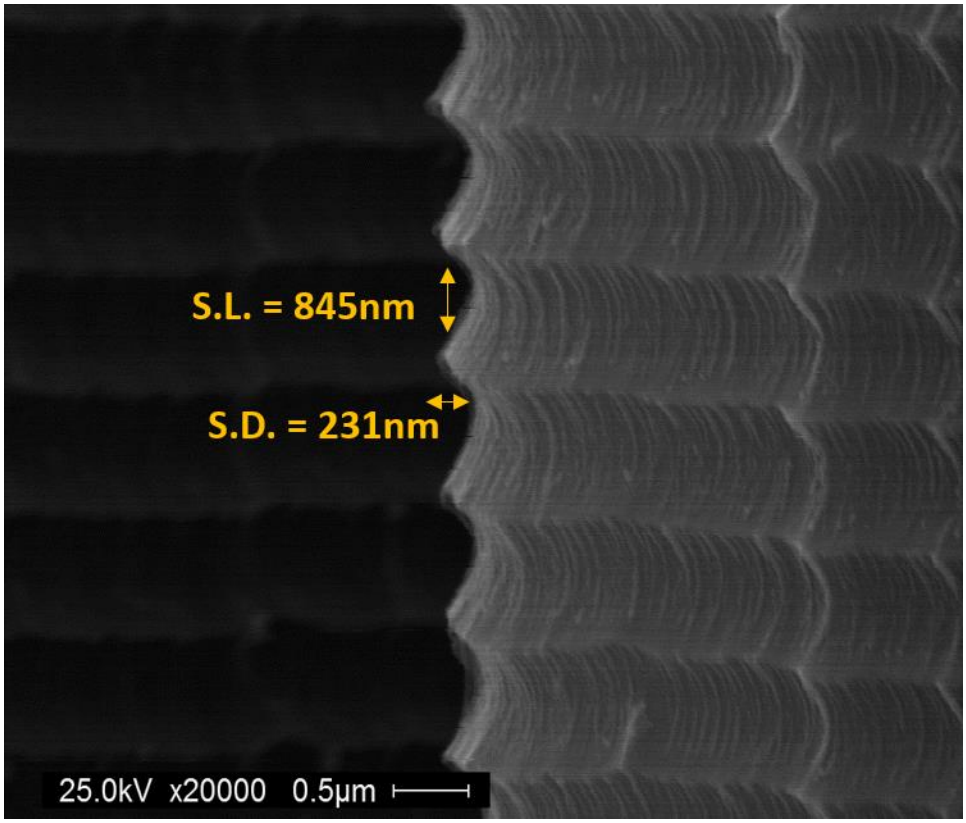

Figure 3.2 – SEM photo of an etched sidewall by a Bosch recipe with a scallop depth (S.D.) of 270 nm and scallop length (S.L.) of 835 nm.

As shown in Figure 3.1 (a), the sidewall scalloping generated by a Bosch process has two parameters for rendering its profiles: depth and length. The scallop length mostly depends on the number of free fluorine radicals that can react with Si atoms isotropically. It could be reduced through lowering source power, SF_6 gas flow rate, and pulse time. Meanwhile, scallop depth also

reflects the isotropic nature of the fluorine radicals at temperatures above -15°C. There are two processes (cryogenic and fast-gas-switching etch) that can mitigate the scalloping issue [37-38].

Cryogenic Si etching uses a continuous SF_6 etchant gas flow at very low temperatures (below -70°C) by leveraging the anisotropic etch nature of free fluorine radicals at cryogenic temperatures [37] and [41]. On the other hand, fast gas switching ICP etcher uses specially designed valves for a rapid (milliseconds) pulsating flow of SF_6 and C_4F_8/O_2 to limit the overall dry-etched sidewall roughness to 50 nm or lower [38]. Sidewall roughness reduction from 20nm to 0.26 nm was reported by post-DRIE thermal annealing in a hydrogen environment that needs a very high temperature over 1000 ^oC and creates rounded profiles [45].

In this work, an Alcatel AMS 100 ICP etcher with fluorine-based reactants such as SF_6 and C_4F_8 is used along with a standard Bosch recipe for creating a sidewall profile with a scallop length of 845 nm and a scallop depth of 231 nm that are insignificant for large microstructures. Nevertheless, they can negatively impact a vibrating micromechanical resonator as its motional impedance relies on the size of the electrode-to-resonator air gap. The scallop lengths and depths were reported (unless otherwise mentioned) near the top of the etched profile as their values often reduce at the bottom of etched trenches, as shown in Figure 3.2.

3.2.1 Optimization of Si DRIE for Reduced Scalloping

To reduce the sidewall roughness of a Si DRIE process by an ICP etcher, all process parameters need to be strategically modified. The thickness of the deposited passivation layer over the sidewall was the first parameter to be tuned. After changing C_4F_8/O_2 pulse time and keeping SF_6 pulse time of 3s and a substrate temperature of -15°C, the sidewall roughness stays largely unchanged, as shown in Table 3.1 and Figure 3.3. Aside from reducing the vertical etch rate, increasing C_4F_8 pulse time has a negative effect as the excess polymer passivation layer could not

be fully etched away by the O_2 plasma. Thus, grass looking residuals are formed due to the micro-masking, as shown in Figure 3.4.

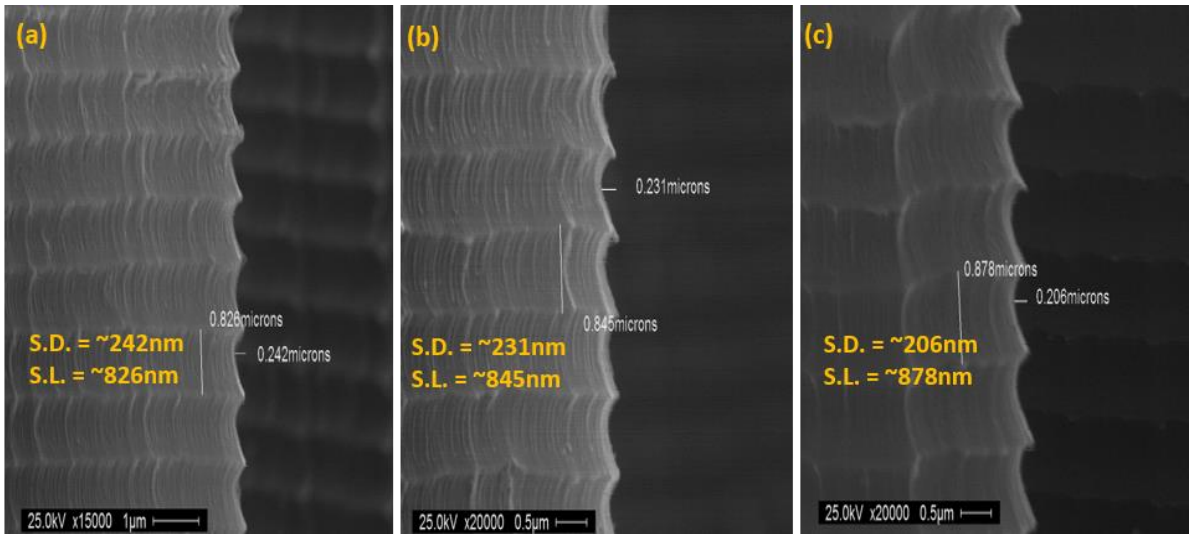

Figure 3.3 – Sidewall scalloping depth/length changes by varying the C_4F_8/O_2 pulse time while keeping other Bosch recipe parameters the same as Table 3.1, showing etched profiles of pulse time (a) 1 sec, (b) 1.4 sec, and (c) 2 sec.

Table 3.1 – Sidewall scalloping depth/length changes by varying the C_4F_8/O_2 pulse time while keeping other Bosch recipe parameters the same.

Temperature (°C)	**Passivation layer**		**Silicon Isotropic Etch**		**Source power (W)**	**Scalloping Feature Dimensions**	
	C_4F_8/O_2 pulse time (s)	**C_4F_8/O_2 flow rate (sccm)**	**SF_6 pulse time (s)**	**SF_6 flow rate (sccm)**		**Depth (nm)**	**Length (nm)**
		1				242	826
		1.2				238	840
-15	200/20	1.4	3	300	2400	231	845
		1.8				226	870
		2				206	878

The next parameter to adjust is the SF_6 pulse time, and it is crucial not to concurrently change two parameters for better comparison. As mentioned, there are commercial ICP etchers that use greatly reduced pulse times in milliseconds to mitigate the sidewall scalloping issue. However, all ICP etchers are designed with physical constraints, such as the minimum pulse time to stabilize a plasma. It was observed that both the scallop length and depth are strongly affected by varying SF_6 pulse time and keeping all other parameters the same as the standard Bosch recipe. For this study, SF_6 pulsating values ranging from 2s to 3s were investigated as values greater than 3s result in a significant sidewall roughness increase while values lower than 2s lead to a significant decrease of the sidewall straightness/anisotropy.

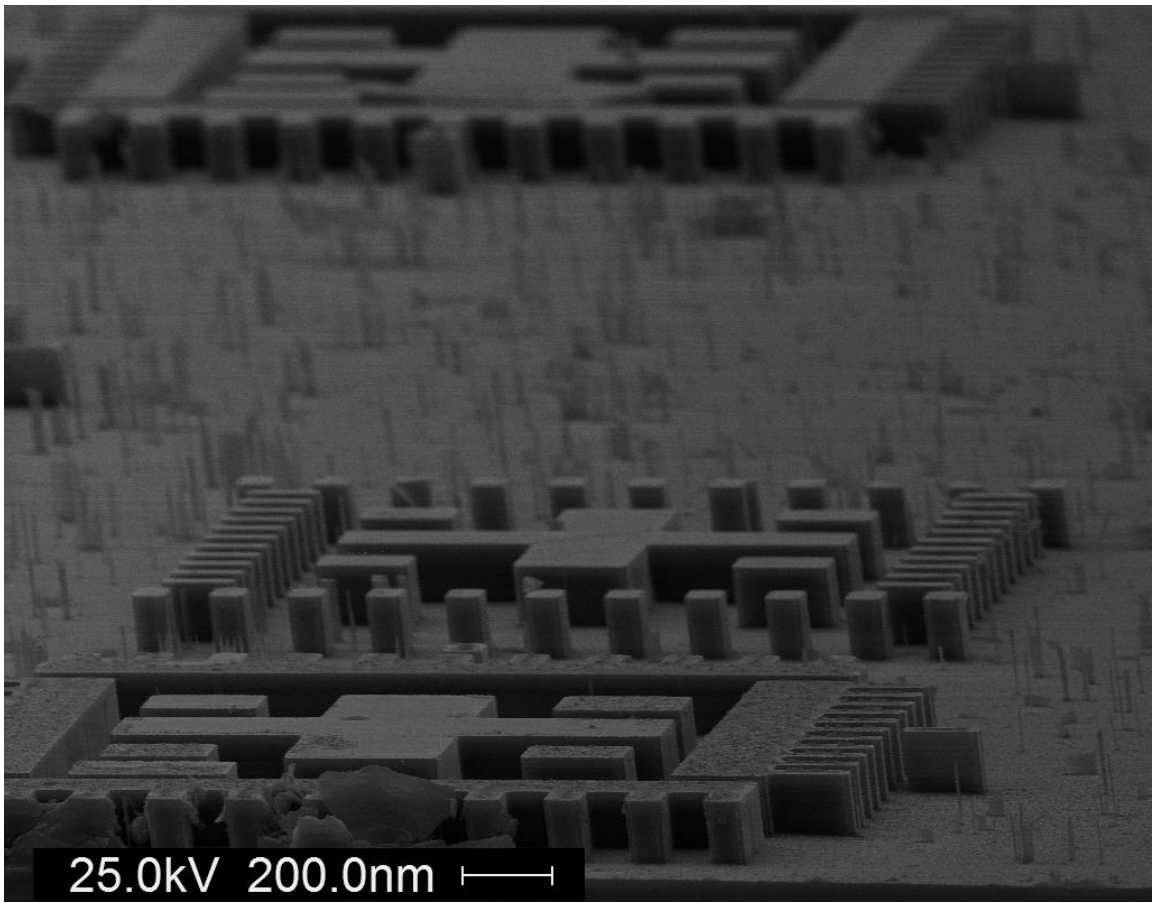

Figure 3.4 – DRIE Bosch process showing the SEM image of the etch profile with grassy looking residuals due to micro-masking.

By choosing an optimal SF_6 pulse time, a reduction of the scallop depth size from 231 nm to 90 nm can be realized, while maintaining the desired vertical sidewall profile. Meanwhile, reduced SF_6 pulse time also slightly lowers the etch rate, as seen in Figure 3.5 (a).

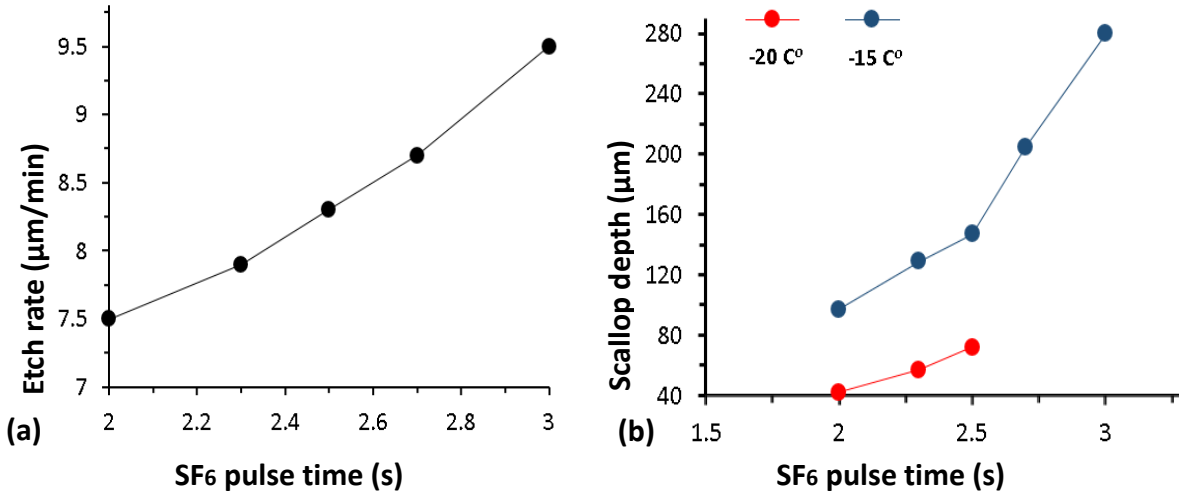

Figure 3.5 – The change of etch characteristics due to modified SF_6 pulse time showing (a) silicon etch rate vs. modified SF_6 pulse time; and (b) scallop depth vs. modified SF_6 pulse time under substrate temperature of -15°C and -20°C.

Next, the process pressure was varied, which has an effect on the etch rate and the profile angle [39-40], but no significant effect on the sidewall scalloping was observed. The substrate temperature was then lowered down to -30 °C to investigate its effects on the DIRE process as fluorine dry etching was reported to be more directional at lower temperatures [41]. As seen in Figure 3.6, the scallop depth was reduced from 90nm to less than 40nm by lowering the substrate temperature from -15 °C to -20 °C, while the scallop length was only reduced from 560 nm to 450 nm. The scalloping depth and length were slightly smaller and drastically larger than a prior report [42], which indicates a better balance between the etch rate and scallop sizes. Also, the etched sidewall is not only smoother but also very vertical at a substrate temperature of -20 °C as seen in Figure 3.7. Despite the fact that a substrate temperature of -25 °C or -30 °C can lead to further reduced scallop depth lower than 27nm, a serious grass formation issue was observed.

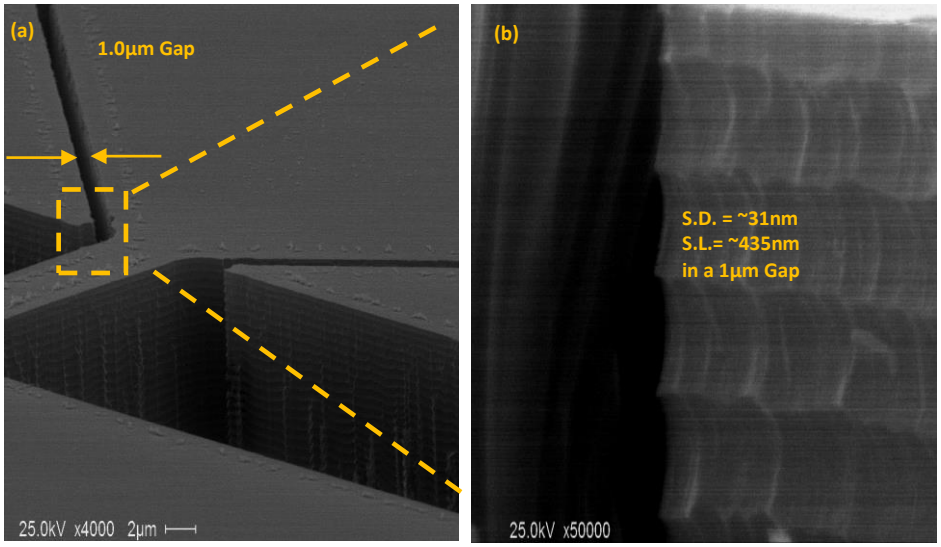

Figure 3.6 – SEM images of DRIE etched sidewall profiles, showing (a) a zoom-out photo of a 1µm wide capacitive gap between resonator body and its surrounding electrodes formed by an optimized Bosch dry etch recipe; and (b) a close-up image of the same area showing the scallop depth size of ~31 nm.

From this study, it can be concluded that smooth sidewalls can be achieved even with standard ICP etchers by modifying both SF_6 pulse time and lowering the substrate holder temperature, which makes the imperative influence. In essence, the sidewall scallop depth achieved by a modified Bosch process was reduced from 271 nm to 42 nm via the generic process optimization. It can be seen that the designed 300nm wide trench would behave like a 385 nm capacitive transducer gap after using the optimized Bosch etch recipe, as compared to 600-900 nm by the original Bosch recipe. Meanwhile, we have explored the well-studied "DRIE-lag" effect for further lowering the scallop depth down to 31 nm for a 1 µm wide, 15 µm deep trench, as seen in Figure 3.6. A similar prior work reported a scallop depth/length of 50 nm/420 nm in a narrow (1.45 µm) opening as compared to the nominal scallop depth/length of 200 nm/790 nm in a wider (201 µm) opening by using a similar Alcatel AMS-100 ICP etcher with different parameters [43].

Finally, to reveal the variation of the scalloping features at different depth of the etched sidewall, several zoom-in SEM photos were taken at positions with a 7 µm depth increment from

the top to the bottom of an etched 5µm wide and 35µm deep trench as shown in Figure 3.7. It can be observed that the scallop depth gradually reduces with etching depth to 18 nm at a 28 µm depth from the top surface of the etched feature. Our results on the reduced sidewall scalloping for a narrow and deep trench with a high aspect ratio confirm a prior work that indicates a strong dependence of the undercut ratio (the ratio of scallop depth and scallop length) on the trench aspect ratio (depth) for a wide range of opening sizes [44-48].

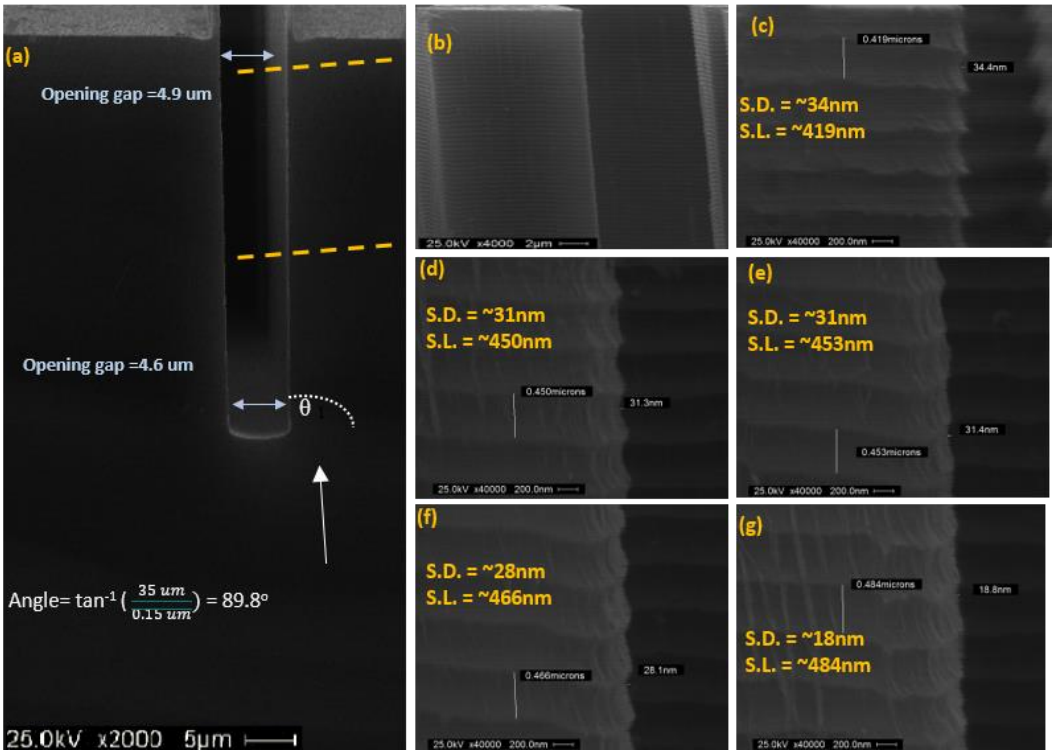

Figure 3.7 – SEM photo of the overall sidewall profile of a 5 µm wide and 35 µm deep DRIE etched trench showing (a) a vertical sidewall angle of 89.8°, (b) a close-up image of the etched sidewall, as well as zoom-in photos showing the sidewall roughness (scallop depth) at different depth from the top to the bottom of the etched trench, depicting scallop depths (c) at very top of 34 nm, (d) at 7 µm depth of 31 nm, (e) at 14 µm depth of 31 nm, (f) at 21 µm depth of 28 nm, (g) at 28 µm depth of 18 nm. All etch depths were from the top surface.

3.3 Fabrication Processes and Tools

3.3.1 Atomic Layer Deposition

Atomic Layer Deposition (ALD) is an important processing tool that deposits thin film to be used as a dielectric capacitive transducer gap filler material, which is a key enabler of capacitive

resonators fabrication process. Deposited ALD film is a very uniform coated layer with very accurate control of thickness and conformal coverage or high aspect ratio microstructures. Figure 3.8 shows the Al_2O_3 film deposition process using Cambridge Nanotech's model Savannah 200 ALD tool.

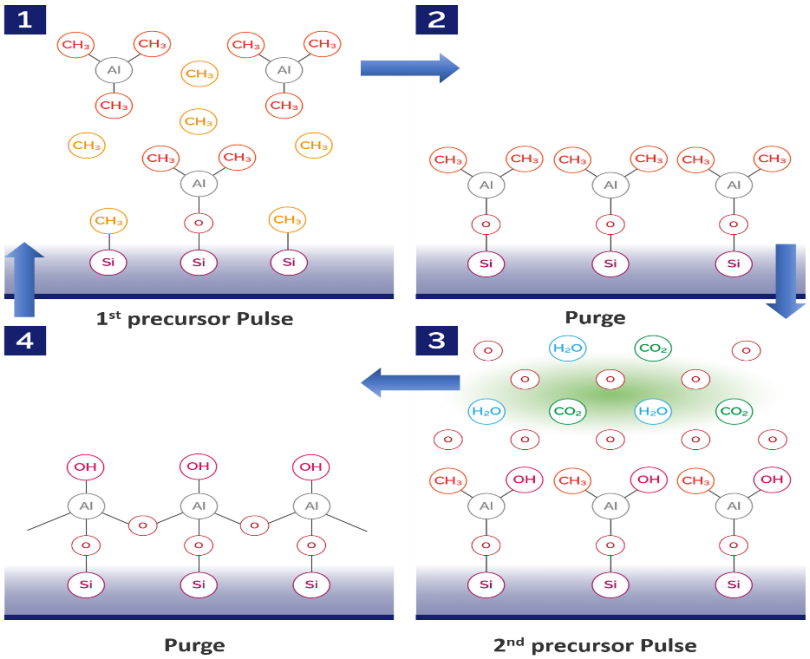

Figure 3.8 – Schematic illustration of the reaction sequence of a typical atomic layer deposition cycle.

ALD deposition process uses two precursors, the water vapor and trimethylaluminum (TMA) precursor, which are sequentially pulsed into the chamber. These two pulses are separated by a purge with an inert gas so that the two precursors never see each other. The process starts with exposure of the 1st precursor, which is the water vapor that adsorbed on most surfaces, forming a hydroxyl group. Then the reaction chamber needs to be purged to make sure non-reacted precursors and the gaseous reaction by-products are removed. After that, the 2nd precursor of TMA is precisely pulsed into the reaction chamber to react with the adsorbed hydroxyl group until the surface is passivated. Neither TMA nor H_2O vapor reacts with itself, which terminates the reaction to one layer and causes the perfect passivation to one atomic layer in a self-limiting fashion. The

reaction chamber needs to be purged again to make sure the non-reacted precursors and the gaseous reaction by-products are pumped away to avoid undesired chemical vapor deposition (CVD) type of reaction between the two precursors. This procedure completes a single cycle of Al_2O_3 atomic layer deposition, and the deposition rate is almost 1Å per cycle for Al_2O_3, and the deposition rate varies between materials. Many different materials can be used in the development of capacitive resonators, including Aluminum Oxide (Al_2O_3), Hafnium Oxide (HfO_2), and Titanium Oxide (TiO_2), and so on.

3.3.2 Chemical Mechanical Polishing

Chemical mechanical polishing (CMP) is one of the key processing techniques of the newly developed and simplified process for the microfabrication of capacitive resonators. The CMP process depends on three major components: specimen carrier, polishing pad, and abrasive slurry. The slurry is usually an aqueous solution with a certain PH level that accelerates the removal rate of targeted material. There are many different slurries, such as aluminum oxide and diamond abrasive slurries, which are used for a specific purpose. Two types of polishing pads are used in this work with different material removal rates. One is employed to remove metals and Si at a fast rate, while the other is specially designed to be used for the superior final surface finish in polishing when it is used with diamond or Al_2O_3 slurries. The CMP process is tuned to have a more uniform removal pattern and rate regardless of the materials being polished. This is achieved by using diamond abrasive slurry because diamond is much harder than most other materials, which make the polishing process more uniform across the wafer substrate even with a variety of surface coating materials such as nickel, platinum, and silicon. The CMP is performed by attaching the wafer to the carrier and rotates against the polishing pad, where the polishing pad helps transferring the slurry's abrasive forces to the substrate to remove the materials from the surface as described

in Figure 3.9. The system used herein for this work is the Logitech PM5 lapping/polishing machine.

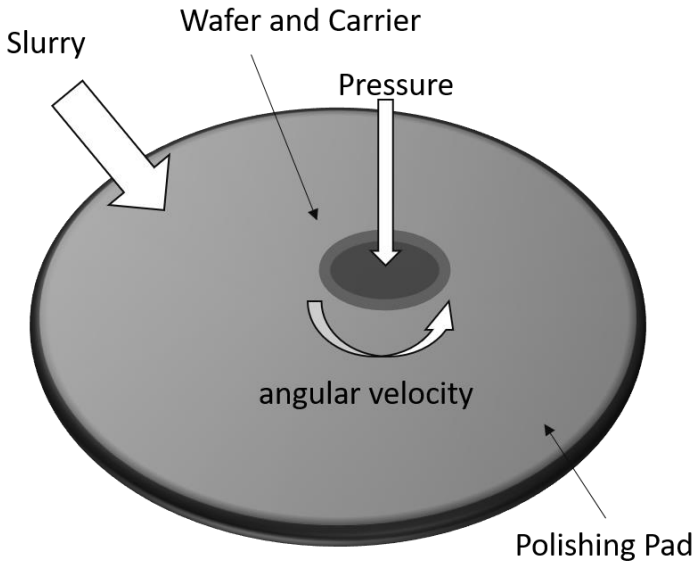

Figure 3.9 – Schematic illustration of CMP process, where the rotation refers to angular velocity of wafer and platen, respectively.

3.3.3 Nickel Electroplating

Nickel electroplating is the most practical way to achieve a relatively thick layer to form capacitive transducer electrodes in MEMS microstructures. In this work, the electrolyte nickel electroplating process was performed by using nickel sulfamate (Ni $(SO_3NH_2)_2$) to achieve low stress and high ductility. Nickel electroplating was fully characterized before it was used to form the side-surrounding electrode for the proposed hybrid MEMS resonators. As observed in Table 3.2, the electroplating solution, nickel sulfamate, was enhanced by boric acid and sodium lauryl sulfate to reduce the surface tension, improve the conductivity, and the brightness (surface roughness), while also eliminating hydrogen bubbles formed during the plating process. This enables the formation of a very smooth surface, as shown in the SEM image below in figure 3.10. In addition, the pH value must be in the range of 3.5 to 4.5 to reduce the roughness and to avoid pitting in the plated structure. To perform the electroplating, the target sample is connected to the

cathode, while a pure Nickel plate is connected to the anode, as shown in Figure 3.11. After running a desired level of current from a current source, the Ni2+ ions are attracted and deposited on the cathode (wafer). The approximated deposition thickness can be calculated from the current value and plating time with the following equation [26]:

$$T = \frac{12.294 \times \mathrm{I} \times \mathrm{t}}{\mathrm{A}} \qquad (26)$$

where A is the area being electroplated in μm^2, T is the desired plating thickness (μm) and, I is the current in amperes and t is the time of the process in hours. The deposition rate, as well as the quality of the plated nickel layer, is highly dependent on the current density, where the current density is the ratio of I/A.

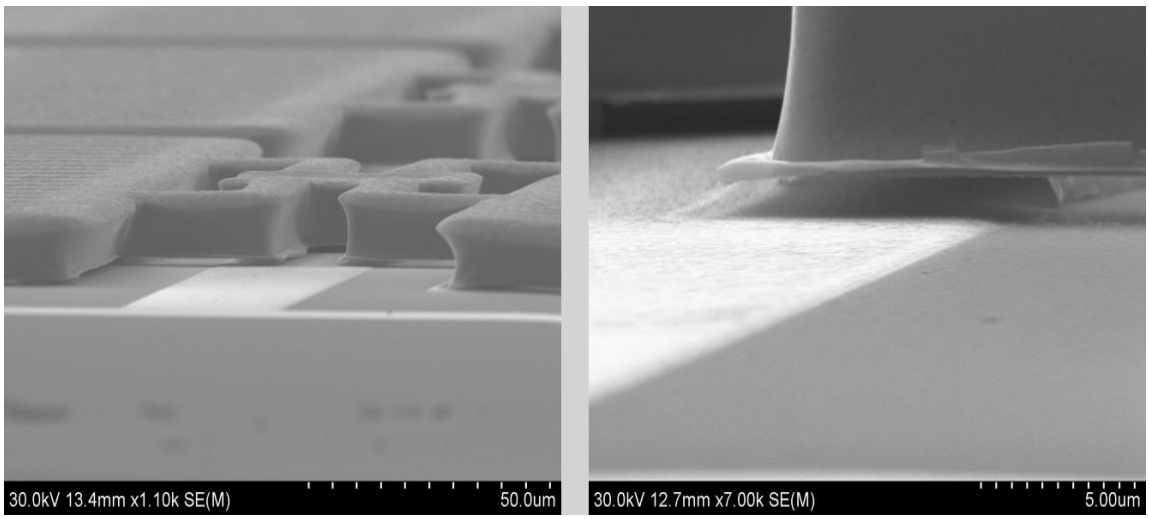

Figure 3.10 – SEM image showing the smoothness of electroplated nickel.

Table 3.2 – Composition and operating conditions for nickel sulfamate solution.

Composition and Operating Conditions for Nickel Sulfamate Solution	
$Ni(SO_3NH_2)_2$, (Nickel Sulfamate)	180 g/L
$NiCl_2 \cdot 6H_2O$, (Nickel Chloride)	4.5 g/L
$B(OH)_3$, (Boric Acid)	22.5 g/L
$CH_3(CH_2)_{11}OSO_3Na$ (Sodium Lauryl Sulfate)	2.7 g/L
Temperature	40-60 °C
Agitation Rate	200 rpm
Current density	10-20 mA/cm^2
pH	3.5-4.5

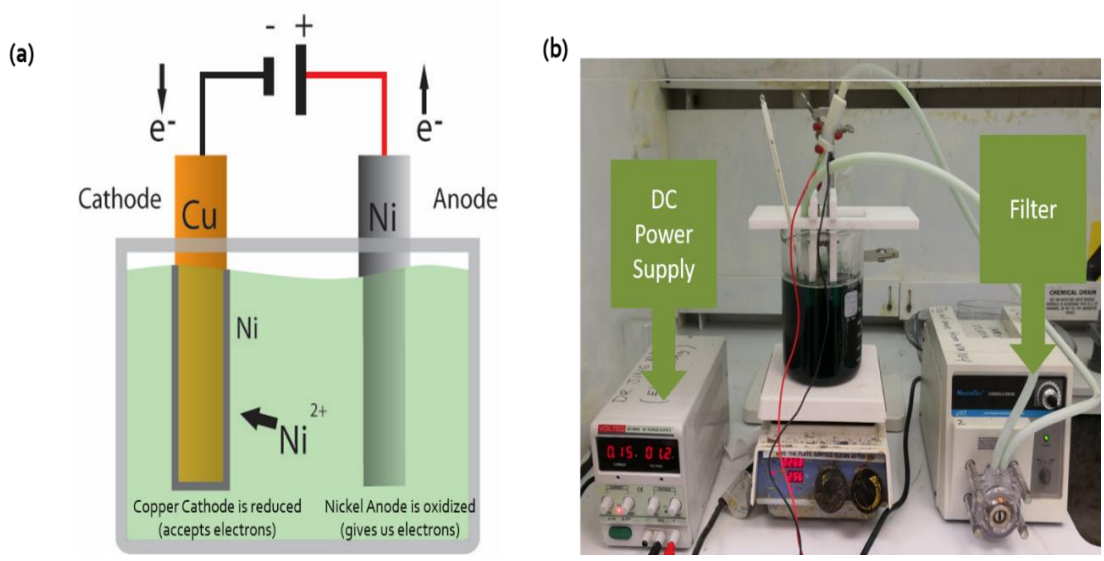

Figure 3.11 – (a) Schematic view and (b) experiment set-up of nickel electroplating apparatus used in this work.

3.3.4 Fabrication Process of Capacitively Transduced Resonators

In this work, the capacitively transduced resonators have been fabricated using a silicon-on-insulator (SOI) wafer along with a three-mask photolithography process. A 2 μm thick buried oxide (BOX) insulation layer made of SiO2 and a 27 μm thick highly doped silicon structural layer with a resistivity ranging from 0.001 Ω.cm to 0.002 Ω.cm are used in this work to achieve higher frequencies as seen in Figure 3.12 (a).

First, a solvent cleaning was performed using Acetone followed by Methanol. Then the wafer is baked for 5 to 10 minutes at an elevated temperature around 120 °C to eliminate any residual solvent. (a) Using 12xt photoresist as a mask, the device layer of SOI wafer is patterned to define the Si vibrating body by etching the Si using Bosch DRIE process; (b) Then, a blanket layer of 90 nm-thick ALD gap dielectric film was deposited using a Savannah 200 atomic layer deposition (ALD) system to define the capacitive gap; (c) After that, plating seed layer was deposited followed by nickel plating everywhere in the wafer; then, the wafer undergoes CMP planarization until the Si interface is exposed completely; (d) Afterwards, the device is released

from the backside by performing through-wafer etch using DRIE. After that, the wafer is dipped in HF acid for 2 mins to release the device after protecting the top side of the wafer with AZ1512 photoresist. Table 3.3 presents the ALD deposition process parameters for the capacitive resonator gap.

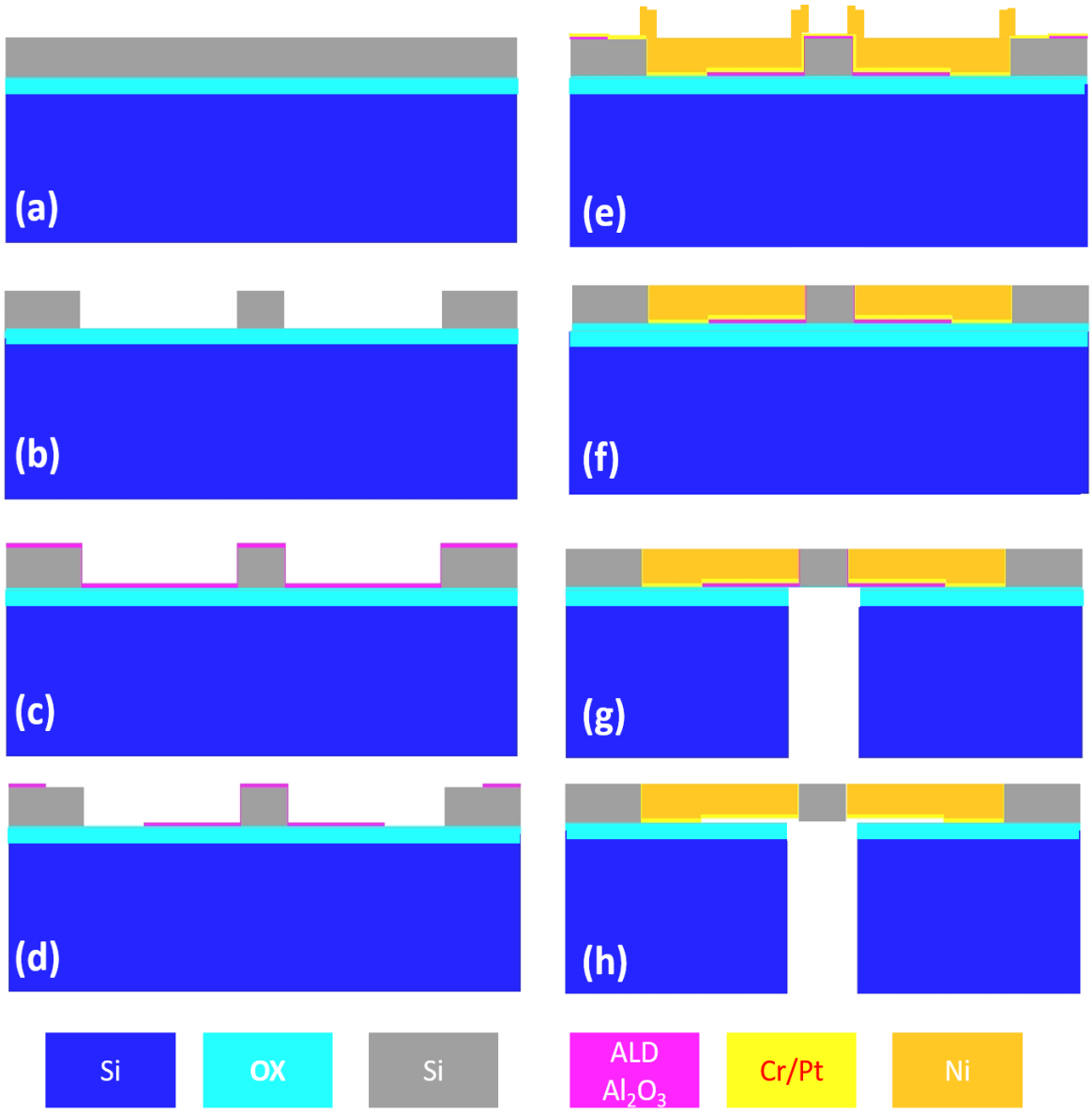

Figure 3.12 – Cross-sectional view illustration of the fabrication process flow of capacitive resonator.

Table 3.3 – ALD deposition process parameters for the capacitive resonator gap.

ALD Deposition parameters	**Al_2O_3**
Inner heater temperature (^oC)	250
Inner heater temperature (^oC)	250
Pulse H2O (sec)	0.015
Wait time between steps (sec)	5
Pulse TMA (sec)	0.015
Growth rates (A)	1 per cycle

Chapter 4: In Situ Localize Annealing Study of Enhanced Stability in Nickel and Silicon Micromechanical Resonators

In this work, a systematic investigation of post-fabrication annealing is performed for ZnO-on-Ni/Si MEMS lateral extensional mode resonators by using a localized annealing process. This post-fabrication annealing process is anticipated to result in a significant improvement in the overall performance of both nickel and silicon resonators. In-situ localized annealing was performed by applying a DC voltage to induce an electrical current through the anchors to the body of the MEMS resonators, which lead to controlled heating of the resonator body to reach a high target temperature needed for annealing. In addition, COMSOL finite element simulations have been conducted to determine the relationship between the applied DC voltage and the elevated temperature of the ZnO-on-substrate resonator composed of both silicon and nickel resonator body structural layer. The measured Q's and insertion loss have been improved as a result of enhancing the material properties due to the localized annealing. On the other hand, the metal on the surface of the resonator (e.g., the bottom electrode underneath the piezoelectric transducer layer) was sometimes melted and diffused into the body of the resonator as a result of excessive heat to a very high temperature by the localize annealing method, which shifting the resonant frequency based on the properties of the deposited metal. In this chapter, the study of the annealing process under some strategically designed conditions on both silicon and nickel resonators has been presented and investigated.

4.1 Fabrication Process of Piezoelectric Resonator

In this work, piezoelectric resonator devices were developed to achieve low motional resistance and high-quality factor using a top electrode design that matches the strain field and ZnO sputtering condition stated in Chapter 2. Piezoelectric resonators were fabricated using an SOI wafer, as shown in Figure 4.1. The ZnO thickness ranges from 500 nm up to 1μm, and the Si device layer for the ZnO-on-substrate resonator has a thickness ranging from 15 μm to 27 μm due to the different thickness uniformity and removal rate by the polishing step between the center and the edges of the wafer when fabricating capacitive resonators over the same wafer.

First, a solvent cleaning was performed using Acetone followed by Methanol. Then the wafer is baked for 5 to 10 minutes at an elevated temperature at 120 °C to eliminate any residual solvent. The fabrication process begins with a photolithography step using a 500 nm-thick LOR-3b and a 5 μm-thick AZ12xt to define a lift-off profile for the bottom electrode of the piezoelectric resonator. As a rule of thumb, it is important that the LOR thickness need to be at least 1.5X thicker than the deposited metal film thickness when using highly conformal depositions technique such as RF magnetron sputtering. Because the LOR is not UV sensitive, a suitable undercut of roughly 2 μm is generated by overdeveloping the LOR when it is exposed to the developer. Then the wafer is treated with an O_2 descum under 100 W and 100 mTorr for 2 minutes to remove any remaining residual photoresist.

In this work, chrome is used as an adhesion layer to provide a good anchor for the following metal layer. Platinum and ruthenium have been used as bottom electrodes because both metals hold the highest chemical resistance and temperature stability along with a good electrical resistivity of 10.5×10-8 ($\Omega \cdot$ m) and 11.5×10-8 ($\Omega \cdot$ m), respectively. AJA sputtering system was used to sputter a 40nm-thick Cr layer and 160nm-thick Ru or Pt layer using the process conditions

shown in Table 4.1. Finally, the wafer is dipped into AZ-400T stripper at 60 °C for 30-45 minutes then washed with DI water. After that, a reactive sputtering deposition of a 500 nm-thick ZnO is performed carefully with optimized parameters to achieve a (002) c-axis aligned crystal orientation. Next, a 1 µm thick AZ1512 photoresist is used to pattern the access to define the anchor points which is called via process that will allow the ohmic contact between the subsequent top electrode through the anchor point located on the bottom electrode layer. After the via is patterned, the wafer is dipped in ZnO wet etch solution of 1 HCL:100 H2O for 90 seconds. The top electrode process is performed by a photolithography step using a 500 nm-thick LOR-3b and 5 µm-thick AZ12xt to have a lift-off profile for defining the piezoelectric resonator's top electrode. Then, AJA sputtering system was used to sputter a 40nm-thick Cr and a 160nm-thick Ru to be used as the top electrode, followed by dipping the wafer into Microposit 1165 remover at 60 °C for 30-45 minutes then washed with DI water. It is worth mentioning that AZ 400T photoresist stripper attacks ZnO and AlN, especially under heated conditions. Thus, Microposit 1165 remover is used instead for the top electrode lift-off process. The final profile of the top electrodes is shown in Figure 4.2 (a).

Table 4.1 – Metal sputtering parameters for the piezoelectric resonator electrodes.

Metal Sputtering Parameters	**Copper**	**Chrome**	**Ruthenium**
Power (W)	100	100	100
Pressure (mTorr)	3	3	3
Ar Flow rate (sccm)	12	12	12
Time (mins)	15	14	33
Thickness (nm)	150	40	200

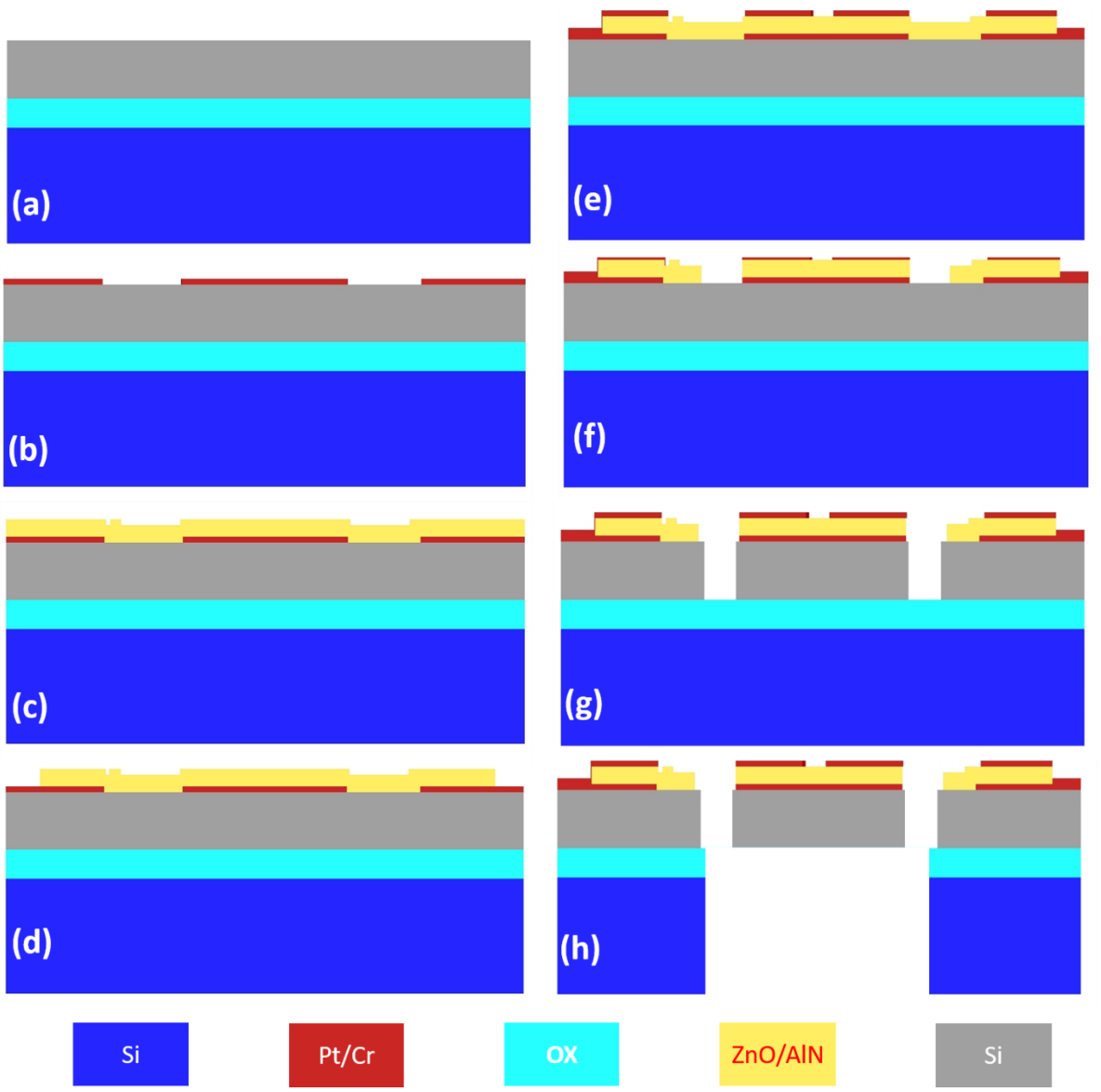

Figure 4.1 –Fabrication process of ZnO piezoelectric resonator on an SOI wafer.

The backside etch technique is used to release the device, as shown in Figure 4.1. Selected areas are defined and patterned by using a 12 µm-thick AZ12xt photoresist first to define the release pattern window on the backside of the wafer to allow etching and removal of selected areas of Si using HAR DRIE Si etch followed by SiO_2 dry anisotropic directional dry etch using an inductively plasma coupled (ICP) etcher and a DRIE process recipe for etching the buried oxide layer. A photolithography step using a 12 µm-thick AZ12XT photoresist followed by a ZnO

reactive ion etching (RIE) process with 30 sccm CH_4, 16 sccm Ar and 8 sccm He gas reactants. The ZnO RIE process is used to define the resonator body shape by selectively etching ZnO to reach the surface of the Si substrate. Thereafter, a silicon anisotropic deep reactive ion etching (DRIE) process is applied to define the body of the resonator by etching through the pre-released device layer that is already suspended. Finally, low power O_2 plasma can be applied to remove any remaining photoresist residues before measuring the device, as shown in Figure 4.2 (b).

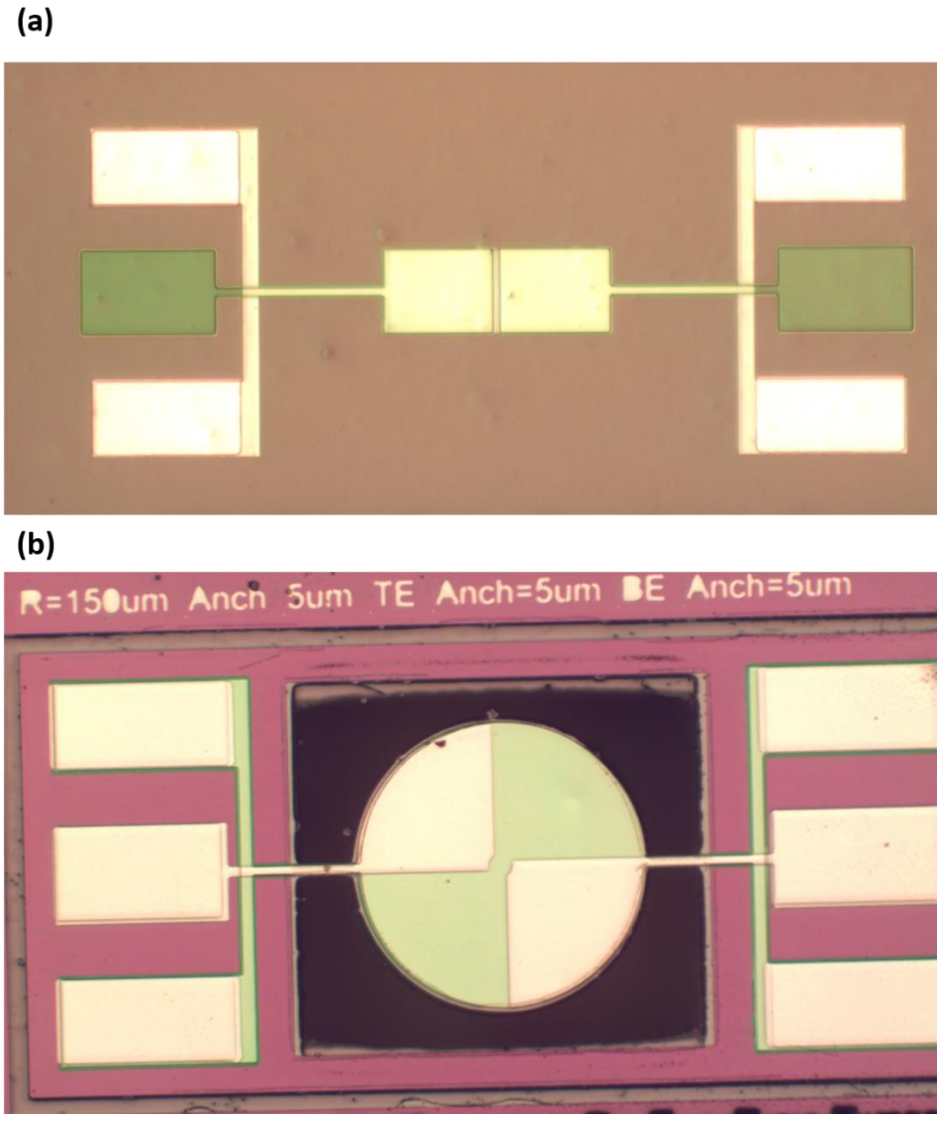

Figure 4.2 – Micro-fabricated (Cr/Ru) top electrodes of the piezoelectric MEMS: (a) after the lift-off step; (b) after the device release.

4.2 The Effects of the Surface Related Losses on the Resonator Quality Factor

Surface roughness shows direct effects on the performance of the MEMS resonators. Most of the energy dissipation in thin-film later extensional mode MEMS resonators have been found to occur via the surface-related losses. All micron-scale resonators suffer from the surface energy loss effect, especially when the ratio of the atoms on the surface of the resonator to the total atoms of the bulk volume of the resonators becomes comparable and cannot be ignored any more when excessive geometrical scaling is employed to further increase the resonance frequency. The surface stress models of both silicon and nickel in this work can be calculated based on the elasticity of the surface stress-strain law while excluding the dissipation mechanism. By applying the idea of Zener's "anelastic" model, the dissipative surface stress model can be written as follows [49]:

$$\sigma s + \tau\epsilon \frac{\partial \sigma s}{\partial t} = \gamma + ES.\epsilon S + ES.\tau\sigma.\frac{\partial \epsilon s}{\partial t} \qquad (27)$$

where ES is the elastic modulus of the surface, γ is the surface tension, σs is the surface stress, ϵS is the surface strain, and τϵ and τσ represent the deformation and the dissipation relaxation times, where γ, σs, and ϵS all have the unit of force/length.

The surface of the resonator can be affected by the stress of the substrate material or the metal on top of the surface. For resonators with significant surface roughness, the equation of the effective surface stress, σss, can be written as the following [51]:

$$\sigma ss = \tau\epsilon \sqrt{\left(\frac{\partial r}{\partial s}\right)^2}.\left(1 + \left(\frac{\partial r}{\partial s}\right)^2 - \frac{v}{1-v}\left(\frac{\partial r}{\partial s}\right)^2\right) \qquad (28)$$

where r presents the roughness of the surface as a function of s, and v is the Poisson's ratio. For the case when the surface of the resonator is totally smooth, the value of (∂r/∂s) is 0. Furthermore, based on the crystallographic structure of the materials, the values of both the residual surface stress and the elastic surface constant can be negative or positive.

4.3 Frequency Shift by Metal Diffusion Induced by Localized Annealing

The resonance frequency of micromechanical resonators is completely dependent on the resonator dimensions as well as material properties. The tolerance of the microfabrication processes such as the photolithography and/or the thicknesses of the resonator layers may cause variation in the resonance frequency of the designed micromechanical resonator to drift from the targeted frequency.

Many frequency tuning techniques have been used in the past as a post-fabrication process to readjust the frequency to the targeted value. Electrostatic voltage tuning is an inefficient way that was previously used. However, due to the large stiffness of the resonator, the electrostatic tuning through the creation of equivalent electric stiffness exhibits a fairly limited tuning range [52]. Metal diffusion has been used in this work as a post-fabrication technique to readjust the resonance frequency of the thin-film piezo-on-substrate resonators to the designed value. The choice of metal electrode is important, which would determine if the frequency shift is upward or downward. By passing a current through the body of the resonator via the anchors, the metal will form an eutectic interface with the body of the resonator at a certain temperature (based on the metal phase diagram), where the metal diffuses into the body of the resonator to affect the stiffness of the resonator and the density. As a result, the acoustic velocity of the resonator will change, which will drift the frequency up or down depends on the chosen metal's properties, such as its atomic weight (density and stiffness). In this work, a systematic study of the annealing effects on MEMS resonators with a thin-film resonator body made of both silicon and nickel have been demonstrated.

4.3.1 In-Situ Annealing Effect for ZnO-on-Nickel Lateral Extensional Resonators

The employment of electroplated nickel as the structural material allows the processing temperature to be kept below 300 ^{o}C that is low enough for post-CMOS MEMS resonator fabrication. The electroplated nickel was carefully tuned to ensure a very smooth surface finish of the electroplated nickel to make sure the nickel surface is smooth enough to not impact the overall performance of the resonator. Still, piezoelectric-on-nickel resonator shows a degradation of the quality factor due to the uncontrolled environment of electroplating. Therefore, a localized annealing process has been used to further improve the actual properties of the electroplated nickel structural layer during this work. By applying a current to the nickel substrate through the anchors, the current will heat the resonator to a high temperature that can readily reach 800 ^{o}C or higher, which results in the removal of the surface contaminants and readjust the structural material throughout its surface and body. Most importantly, the electroplated nickel serves as a bottom electrode and a seed layer that can impact the c-axis alignment of the sputtered ZnO piezoelectric layer, which can affect the coupling coefficient of the resonator, which can be ascribed to variations of piezoelectric coefficients (e.g., d_{31}). The localized annealing processes can improve quality factor (Q), kt^2 factor, and motional impedance (R_m) by reducing the residual stresses and smoothing the surface of the resonator while improving the acoustic properties of the electroplated nickel.

To perform the annealing, a maximum of 0.4 A electrical current can be applied to a 96μm width rectangular plate resonator for no longer than 30 mins to heat up the device to a certain level without damaging the anchors. As a result, the localize annealing has enhanced the performance of the resonator by increasing the value of quality factor from 580 to 1,100 and decreased the motional resistance to be as low as 246 Ω as shown in Figure 4.3. In addition, as the nickel

structural material has been softened, the frequency of the resonator has been drifting down accordingly.

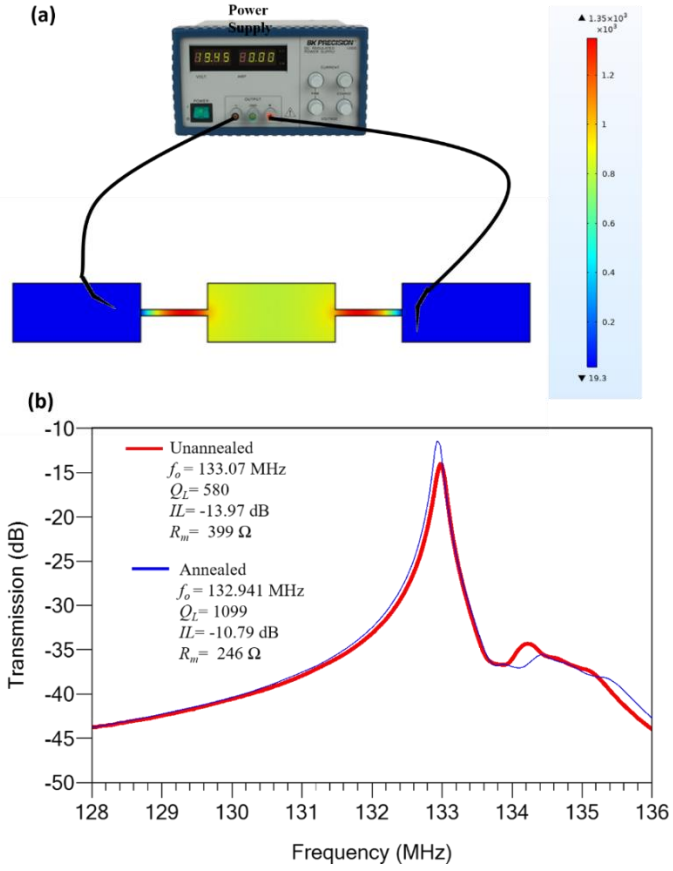

Figure 4.3 – Conceptual illustration of the localized annealing scheme by showing (a) a COMSOL simulation model that depicts the temperature distribution and the actual localized annealing set-up scheme; and (b) frequency responses of ZnO-on-nickel resonator measured before and after localized annealing.

The annealing of nickel resonator has a limitation that prevents one from applying a larger current or applying the current for a longer time due to the need for the current to flow through narrow anchors that suspended the resonator. The quality factor can be further improved if the anchor's width of the device was designed to be wider in order to be able to apply a much higher current, which can heat the body of the resonator to even higher temperatures. A maximum of 30 mins of annealing can be performed in the nickel resonators before the anchors are totally

destroyed by the very high temperature that heated up the anchors more severely before the body of the resonator due to its narrower width and higher resistance.

4.3.2 In Situ Annealing Effect on ZnO-on-Silicon Lateral Extensional Resonators

Silicides are caused by the reactive diffusion between the metal and Si as the surface of the silicon, and the metal is heated up to a certain temperature depending on the choice of metal, which is called silicidation temperature. By applying an electrical current to thin-film piezo on silicon (TPoS) resonators, the bottom electrode metal will react with only the underlying silicon resonator body but not the dielectric ZnO film, which will cause the metal and the Si to react to form a new thin silicide combination layer after reaching the silicidation temperature. Silicidaition is widely used in electronic devices application to reduce contact resistance. The silicidation temperature ranges from 363 °C for aluminum silicide up to 850 °C for titanium silicide [53]. In order for platinum to diffuse into the bulk of the silicon, the surface needs to be heated to at least 600 °C, which is the silicidation temperature for the Pt and Si to react and form PtSi on the surface of the resonator. This temperature is much lower than the melting point of the platinum (1768.2 ^{o}C) or the silicon (1414 ^{o}C) [54]. The silicidation temperature can be reached by applying a current of 1 A to the body of the resonator, which will raise the temperature of the resonator to 1000 ^{o}C based on COMSOL finite-element modeling (FEM). As a result, the Pt–Si bonds will break the Si-Si bonds since they are stronger than the bonds that they will replace. This will cause the frequency to shift up by 500 kHz as the platinum diffusion reduces the density and increases the effective stiffness, thus increasing the effective acoustic velocity. On the contrary, for other metals such as aluminum (Al), the newly formed metal–Si bonds are weaker than the ones in Si–Si, which will result in a downward frequency shift after performing the in-situ annealing as seen in Figure 4.4. The metal diffusion into the body of the resonator can be clearly seen by using a TEM image to

show the diffused metal and ordered atomic planes of resonator atoms before and after the as shown in Figure 4.5 and Figure 4.6.

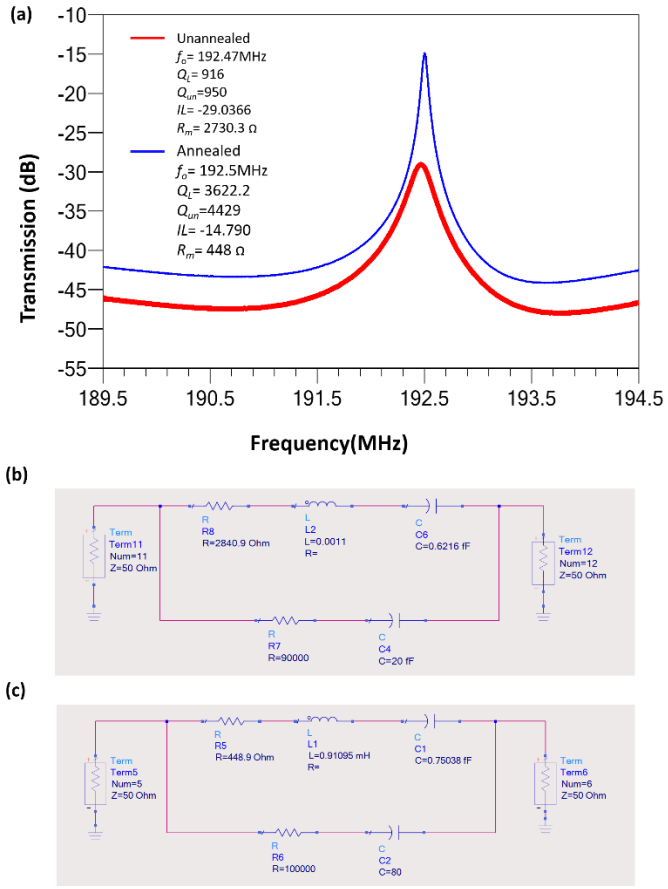

Figure 4.4 – Measured responses of ZnO-on-silicon resonator, including: (a) measured results for the same resonator before and after localized annealing is applied; and b) a typical BVD model for resonator before the annealing; (c) a BVD model for the same device after the annealing.

As a result of applying the Joule heating to thin-film piezo-on-silicon resonator, the quality factor and insertion loss were also enhanced after heating up the device to cause the removal of surface-attached contaminants while reducing the surface stress and readjusting the surface of the structural material. The quality factor has been drastically increased from 950 to 4,429, and the motional impedance has been decreased from 2730 Ω to 448 Ω. A typical BVD model of the measured piezoelectric resonator before and after the annealing is shown in Figure 4.4. The ZnO is known to be a lossy material. And as shown in the LCR circuit model, the value of the inductance

is too high in the circuit. Given the inductance dominates in the BVD model, it results in the weakening of the anti-resonance frequency response.

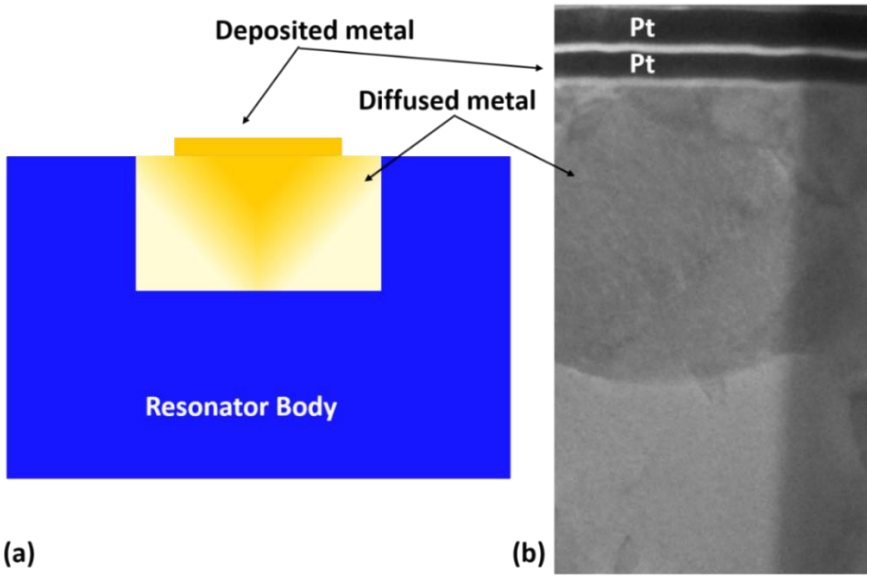

Figure 4.5 – (a) Illustration of the metal diffusion into the body of the resonator; (b) TEM image shows the diffused metal.

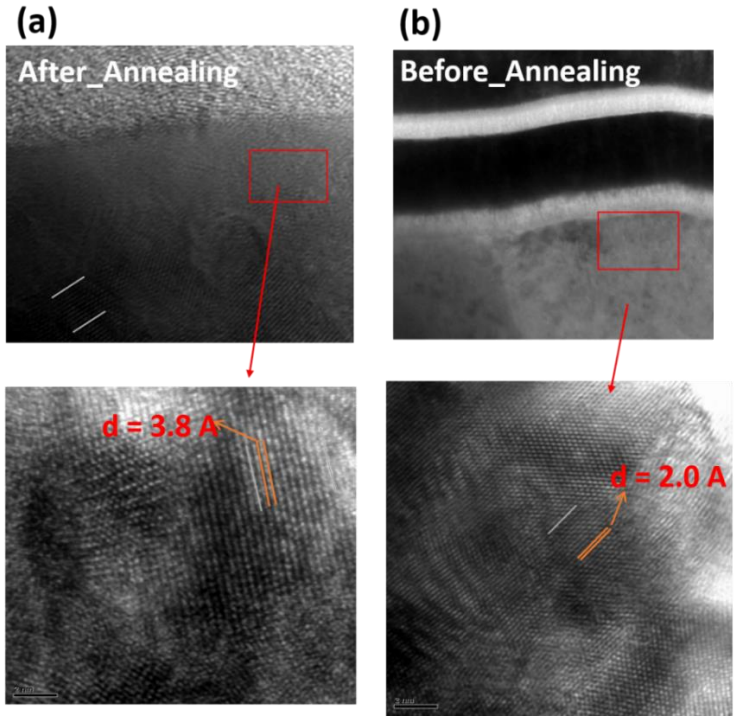

Figure 4.6 – TEM images showing ordered atomic planes of resonator atoms, which is taken for devices (a) before annealing, and (b) after annealing.

Chapter 5: Combined Capacitive and Piezoelectric Transduction Resonators

Among the various possible transduction mechanisms for on-chip micromechanical resonator technologies, piezoelectric and capacitive resonators have been mostly used because of their specific individual advantages. On the one hand, capacitively-transduced resonators exhibit high Q-factor at higher frequencies and hold many other advantages such as on/off self-switching capability, better temperature coefficient, and best possible spectral purity. On the other hand, piezoelectrically-transduced resonators offer low insertion loss and relative ease of fabrication, and they have been demonstrated with 50 Ω matched motional impedance. Filters based on piezoelectric material have shown insertion loss as low as 3dB while capacitive resonators are operating at high frequency up to 6.2 GHz while still exhibiting Q higher than 4000. Sadly, with all the aforementioned advantages, neither capacitive resonators nor piezoelectric resonators by themselves can make such a single resonator unit to fulfill the needs of chip-scale spectrum analysis as a solution required for the emerging single-chip multi-frequency RF front-end applications. Fortunately, these two resonator design configurations can very nicely complement each other. Therefore, by combining capacitive and piezoelectric transduction in silicon microresonators, the advantages of both these technologies could be consolidated in one single device. The concept of combining both piezoelectric and capacitive resonators as a dual-transduced micromechanical resonator is introduced in this work to combine the advantages of a high electromechanically coupling coefficient from piezoelectric transducers, low acoustic loss property from high Q materials such as Si, and additional functionalities such as on-off switching and frequency tuning.

5.1 Parasitic Effect in MEMS Resonators

A typical MEMS resonator that is fabricated on a silicon-on-insulator (SOI) wafer has parasitic elements that limit the performance of either capacitive or piezoelectric micromechanical resonator. The imperfect ground provided by the silicon of the wafer handle layer an SOI substrate contributes to a capacitive feedthrough signal traveling between the drive and sense electrodes, which increases the noise floor to such an extent that the resonance peaks from the resonator device layer are going to be strongly distorted or swamped by the feedthrough noise floor, as shown in Figure 5.2.

Figure 5.1 illustrates the feedthrough signal travel paths for both capacitive and piezoelectric resonators. The air gap in the capacitive resonator limits the RF signal path of the feedthrough signal to travel only through the substrate underneath each device. Since air provides superior signal isolation than any other solid dielectric, the overall parasitic feedthrough signal is considerably less for resonators equipped with air-gap capacitive transducers since the RF feedthrough signal can only travel from the actuation and sensing parallel plate electrodes through the SOI wafer handle layer (i.e., the silicon layer underneath the buried oxide layer). On the other hand, piezoelectric resonators heavily rely on the two closely positioned input and output electrodes that sit next to each other on top of the piezoelectric layer for actuation and detection operation. Therefore, the RF feedthrough leakage signal has two paths to travel through the substrate and through the piezoelectric transducer layer (dielectric).

Parasitic elements become more noticeable and influential at higher frequencies. As shown in Figure 5.2, the high Q resonance peaks are not shown in the measured forward transmission frequency spectrum due to the high feedthrough level at high frequencies because the feedthrough signal escalated quickly as frequency goes higher. To mitigate this problem, the drive/sense

parasitic capacitances can be de-embedded using a vector network analyzer (VNA) based calibration approach. The signal-to-noise ratio can also be significantly improved, which makes the resonance peak raise above the feedthrough noise floor level. However, such de-embedding by using VNA may not be practical in the practical integration of silicon MEMS resonators with ICs for timing and filtering in RF front-end applications.

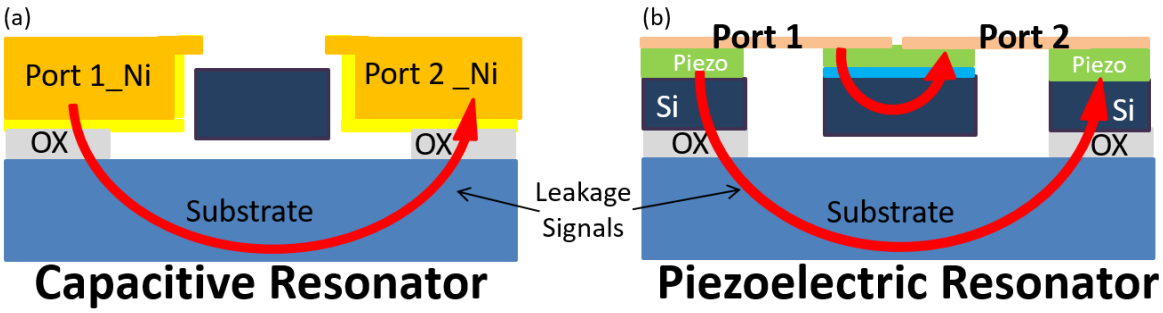

Figure 5.1 – Conceptual illustration of feedthrough signal travel paths for (a) capacitive resonator; (b) piezoelectric resonator.

Another approach to demonstrate parasitic compensation of micro-scale resonators is by combining piezoelectric transduction with capacitive transduction in silicon micromechanical resonators. Capacitive transduction is well known to offer an unprecedentedly high frequency-Q product (f×Q) and a very low feedthrough noise level from the input to the output electrodes, which result in very low noise levels. On the other hand, piezoelectric transduction offers a very low motional impedance due to its high electromechanical coupling coefficient. This combination strategy can further be used to enhance the Q-factor of piezoelectric resonators to achieve simultaneous high-Q and low impedance resonators with input and output electrodes completely isolated, which should improve the cross-talking between input and output ports even at high frequency (up to tens of GHz).

As illustrated in Figure 5.3 below, combining both transduction mechanisms to harvest the individual advantages of both these technologies should lead to having an excellent signal to noise

ratio as we can employ a few different transduction mechanisms in such hybrid resonator, some of which are much less prone to parasitic feedthrough. In Figure 5.3 (a), by using the piezo electrodes (ports 3 and 4) to actuate the device while sensing from the capacitive electrodes (ports 1 and 2), this will not only reduce the cross-talking between input and output electrodes but will also improve the suppression of spurious modes as capacitive resonator tend to suppress all modes other than the targeted frequency which produce a stronger and cleaner signal response. Similarly, as can be seen in Figure 5.3 (b), using the capacitive electrodes (ports 1 and 2) to actuate the device while sensing from the piezo electrodes (ports 3 and 4), this will lead to reducing the cross-talking between input and output as these electrodes are completely isolated.

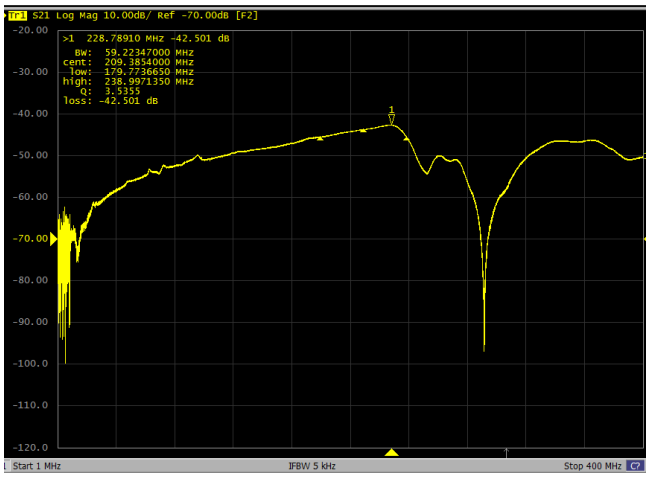

Figure 5.2 – Measured response in the air of a capacitive MEMS resonator without applying the de-embedding of the drive/sense parasitic capacitance signal by using a VNA.

This testifies that the hybrid MEMS resonator concept by showing a few configurations of such a device that can achieve not only true input and output isolation but also a true hybrid (reconfigurable) design. Basically, a designer can operate such a resonator by taking full advantage of its multi-port configuration and asymmetric input-output characteristic behavior between two transducer types. By combining the low loss acoustic characteristic of an electrostatic microresonator with its resonant body largely made of silicon with high electromechanical

coupling values of the chosen piezoelectric material, most problems that MEMS resonators are currently facing will be directly or partially addressed. The primary goal of having dual resonators is to combine the advantage of the additional influx of acoustic energy from capacitive actuation that offers an improvement of Q-factor with the low insertion loss and small motional resistance from piezoelectric actuation while still retains all the other aforementioned benefits. These added benefits include capacitive resonator's self-switching capability, voltage-controlled configurability, better thermal stability, the benefit of frequency tuning. Table 5.1 summarizes the key characteristics (advantages and weaknesses) of electrostatically-transduced and piezoelectrically- transduced MEMS resonators.

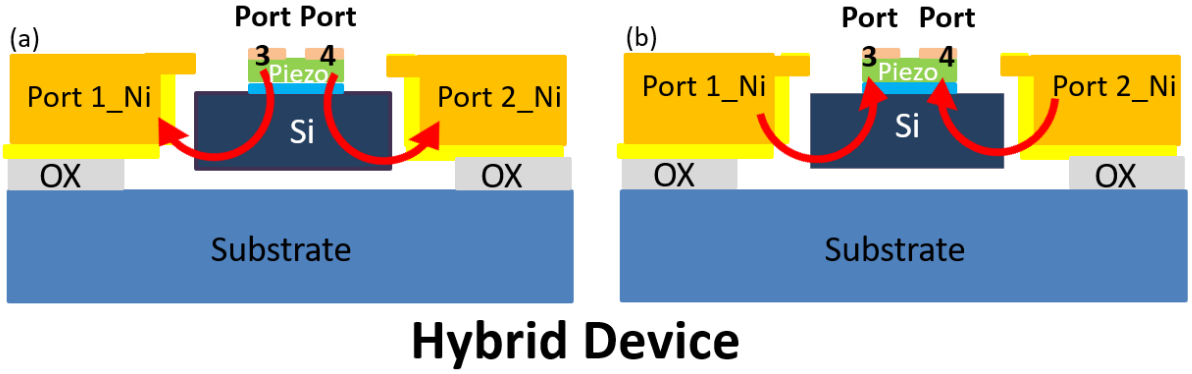

Figure 5.3 – Illustration of signal travel paths for a hybrid resonator with reduced feedthrough as device operate in different configurations, including (a) piezo drive and capacitive sense; and (b) capacitive drive and piezo sense.

Table 5.1 – Summary of the advantages and disadvantages of capacitive and piezoelectric MEMS resonators.

	Capacitive	Piezoelectric
Quality factor	High	Moderate
Fabrication	Complicate	Relatively easy
Motional impedance	High	Low
Signal feedthrough	Moderate to high	Moderate to high
Reconfigurability	DC bias ON/OFF	None
Material selection	Most of the conductive materials (Si, Diamond, Ni)	Only mainstream piezoelectric materials

5.2 Hybrid Resonator Fabrication Process

The hybrid resonator fabrication process starts with the fabrication of the capacitive resonator, followed by the building of the piezoelectric resonator structure on the top. Figure 5.4 illustrates the fabrication process of the capacitive and piezoelectric hybrid resonator. The fabrication process starts with a photolithography step using a 5 μm-thick AZ12xt photoresist followed by etching the silicon using the modified HAR DRIE Bosch etching recipe (as described in chapter 3). Next, a 90 nm-thick gap spacing layer made of Al_2O_3 was deposited using a Savannah 200 atomic layer deposition (ALD) system to define the capacitive gap, as seen in Figure 5.4 (b). The next step is the major modification in this fabrication process, where the capacitive electrodes needed to be fixed to silicon instead of being sitting atop the gap layer. The ALD layer can be attacked easily by HF, which will cause the plated metal capacitive electrodes to delaminate in the subsequent HF oxide release process to fully define the 90nm nano-scale capacitive transducer gap. Therefore, it is important to etch the ALD layer from some of the sidewall regions in the capacitive electrodes to allow the electrodes to be attached directly to the silicon layer (without ALD layer), as shown in Figure 5.5. To do that, the gold pad mask was used here along with a photolithography step using HMDS, 1μm-thick LOR 10b, and 5μm-thick 12xt photoresist followed by 6:1 buffer oxide etch (BOE) wet etching to remove the ALD gap layer from some sidewall areas. It is important to use HMDS and thicker photoresist because of the pre-defined trenches in the wafer that causes a high level of topology; otherwise, the resist adhesion will be impacted. A peeling of photoresist film issues on the edges of the structure occurred when thinner photoresist such as 1512 and LOR 3b was used. After developing the photoresist, thin photoresist does not stick in the edges of the device structure, as shown in Figure 5.6. To solve this issue, LOR 10b and 12xt were used in this step.

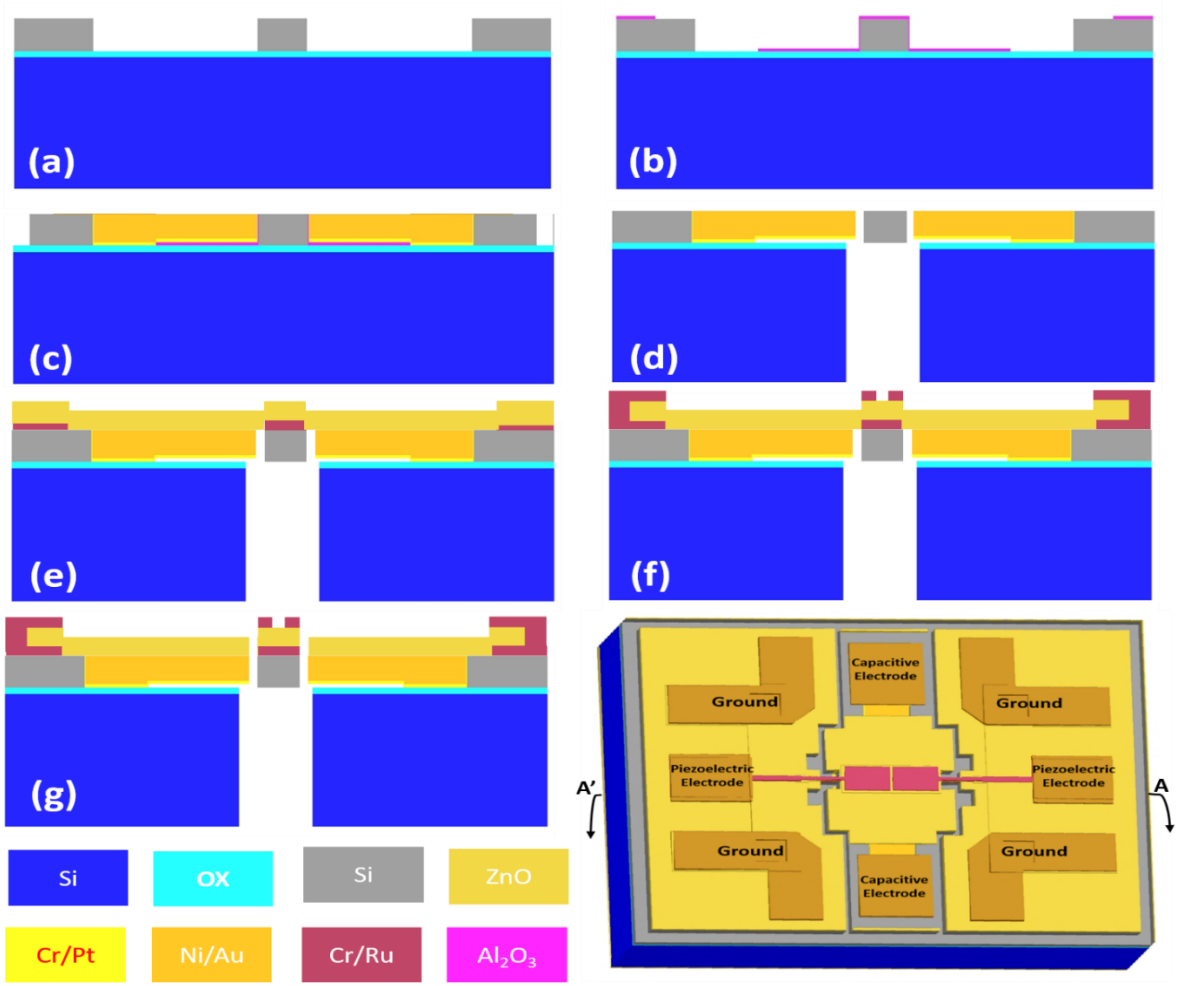

Figure 5.4 – Top view and cross-sectional view illustration of the fabrication process flow of hybrid resonator.

After the gap layer step, a seed layer deposition is performed using AJA sputtering system to deposit a 40 nm-thick layer of chrome that acts as an adhesion layer and a 150 nm-thick layer of copper. Electroplating is the most practical way to achieve the relatively thick capacitive electrode layer at low cost and high fabrication yield. In this work, the capacitive electrode is formed using nickel electroplating. The plating process starts with a lithography step to define a mold for nickel plating by performing it over a selective area opened within a thick layer of photoresist. In this work, a 14 µm-thick AZ 12xt resist was used, followed by an O_2 descum treatment under 100 W and 100 mTorr for 2 minutes to remove any remaining residue of

photoresist. Once the lithography step is completed, the seed layer needs to be activated before the electroplating process by etching away any oxide layer that is generated during the O_2 descum treatment process. Seed layer activation process can be done by soaking the wafer in a 200:1 solution of deionized (DI) water to 30% Ammonium Hydroxide (NH_4OH) for 30 seconds, followed by washing in with DI water (3 times) to etch and remove the copper oxide layer formed on the surface of the seed layer.

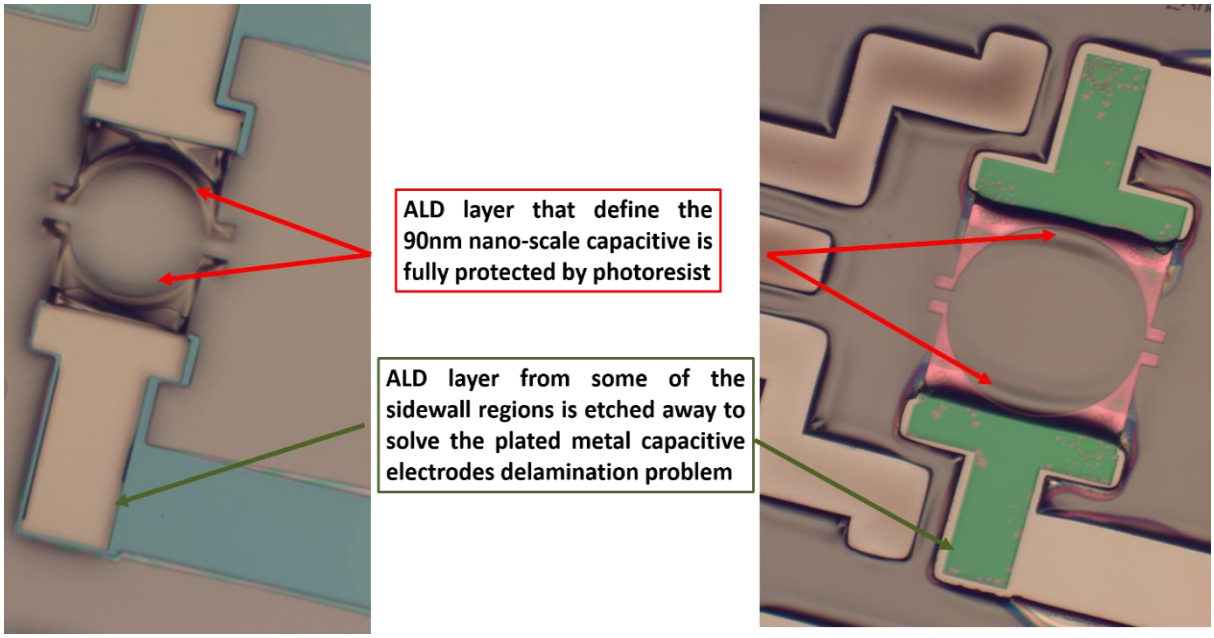

Figure 5.5 – ALD layer is etched from some of the sidewall regions in the capacitive electrodes to allow the electrodes to be attached directly to the silicon layer (without ALD layer).

After that seed layer activation, a thick nickel side electrode (27 µm) is plated in the selected area that is defined and patterned by the photoresist to form the capacitive drive/sense electrodes. A nickel sulfamate (Ni $(SO_3NH_2)_2$) solution is used for nickel electroplating to achieve low stress and high ductility that is mixed with sodium lauryl sulfate and nickel chloride to improve the brightness and conductivity. Boric acid is added to keep the PH level value between 3.5 and 4.5 to reduce the pitting and the roughness, as shown in Table 5.2. To electroplate a 27µm-thick

of nickel electrodes, 10 mA/cm^2 current density was applied for 150 mins to obtain low roughness and better plating quality at the expense of reduced plating speed.

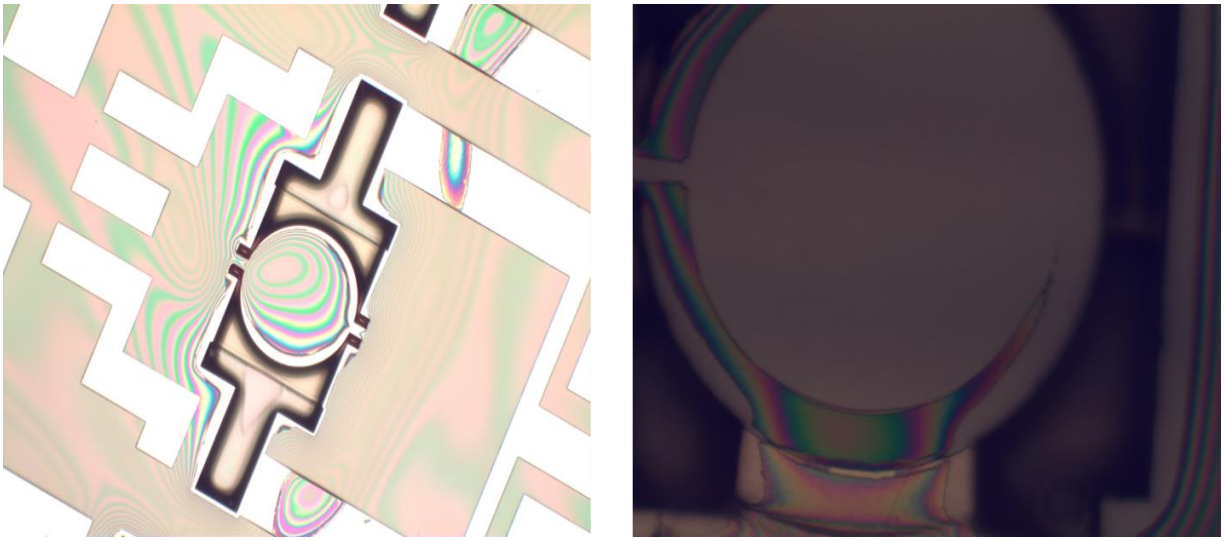

Figure 5.6 – Shows photoresist adhesion problem if there are pre-etched trenches in the wafer.

Table 5.2 – Lithography process parameters for the hybrid resonator fabrication process.

Photoresist		**Az12xt**	**Az1512**	**LOR 3b**	**LOR 10b**
Spinning step 1	speed (rpm)	500	5005	500	500
	time (s)	10	10	10	10
Spinning step 2	speed (rpm)	2500	2500	2200	2200
	time (s)	40	40	40	40
Soft bake / time		110^{o}C /120 sec	95^{o}C /50 sec	180^{o}C /8.5mins	180^{o}C /8.5mins
Post bake (^{o}C) / time (sec)		90^{o}C /60 sec	105^{o}C /50 sec	-	-
Developer / time		Az 300	Az726	Az300/Az726	Az300/Az726
Layer thickness [nm]		5000	1000	500	1000

Afterward, the wafer is planarized from the top uniformly until the Si layer interface is exposed using the polishing tool, as described in section 3.3.2. The wafer is polished for 90 mins using Nylon polishing cloth and 5 micron-sized Aluminum Oxide powders, followed by 60 mins polishing by using Rayon final polishing cloth and 0.9 micron-sized Aluminum Oxide powders polishing as shown in Figure 5.7. The uncovered seed layer metal is etched away before releasing the device. To release the device, a front or a backside etch could be used. In both techniques, selected areas are defined and patterned by the AZ12xt photoresist first to etch the Si using DRIE followed by an oxide etch using hydrofluoric (HF) acid for 2 mins, which will attack both the ALD gap layer and the 2 µm-thick buried oxide layers from the backside opening of the wafer which will result in releasing and suspending the device before depositing the ZnO layer as shown in Figure 5.10.

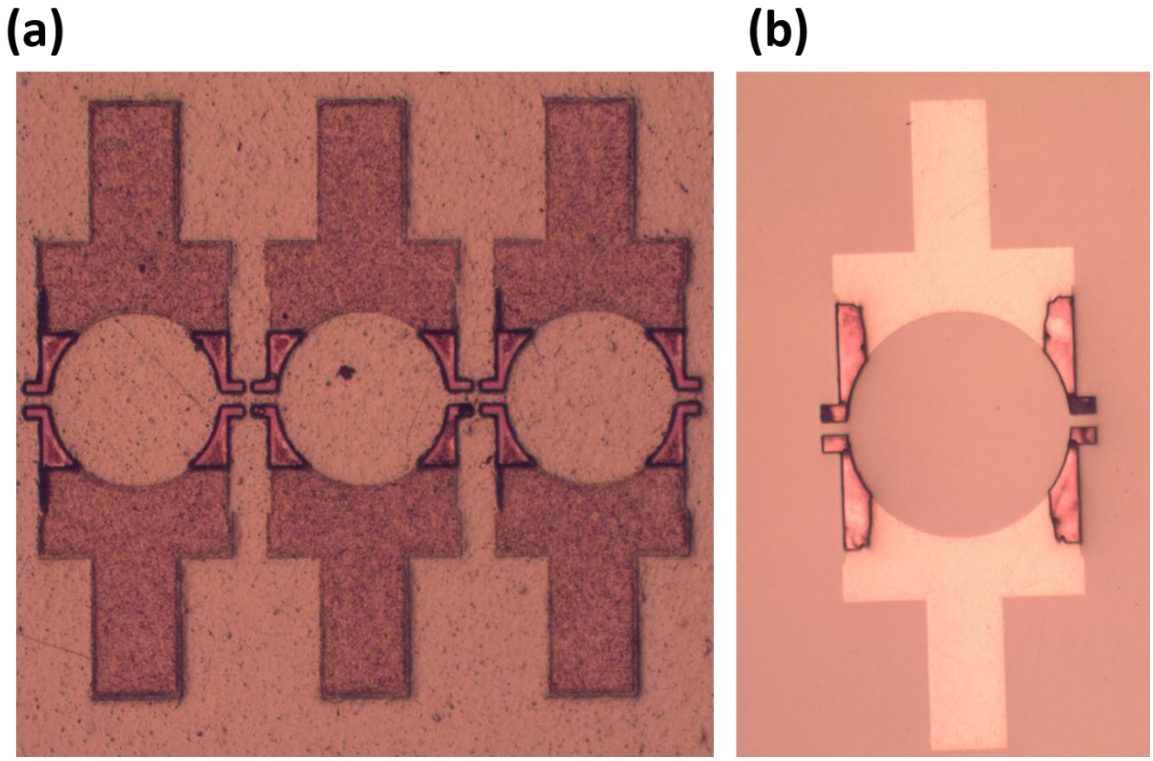

Figure 5.7 – Top-view microscope image of the capacitive electrodes and resonator body after the polishing using: (a) nylon polishing pads; (b) rayon polishing pad.

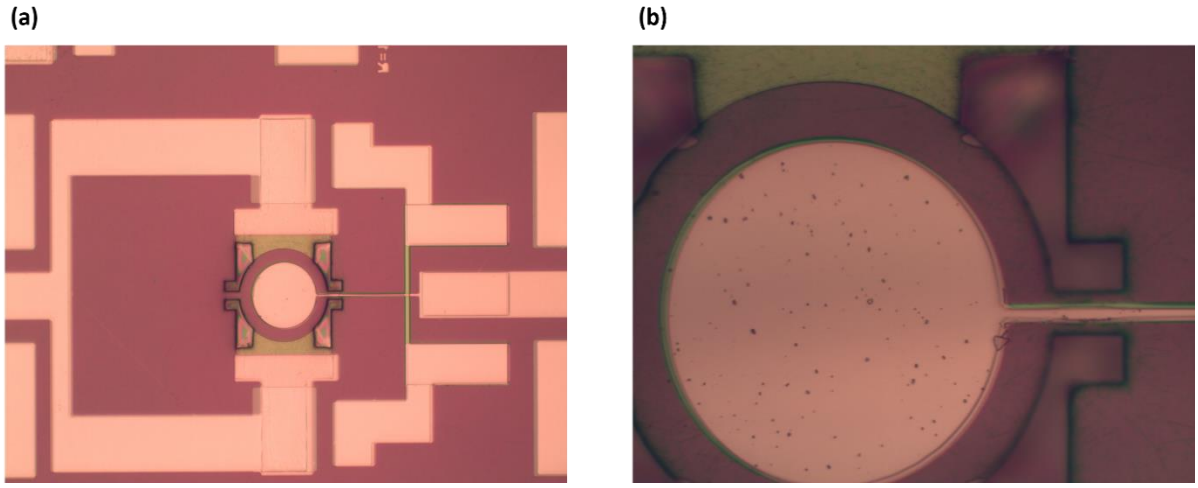

Figure 5.8 – Top-view microscope image of the top electrode of the hybrid resonator to define the piezoelectric port of the resonator, where the other port has the capacitive electrodes that's surrounded the resonator body.

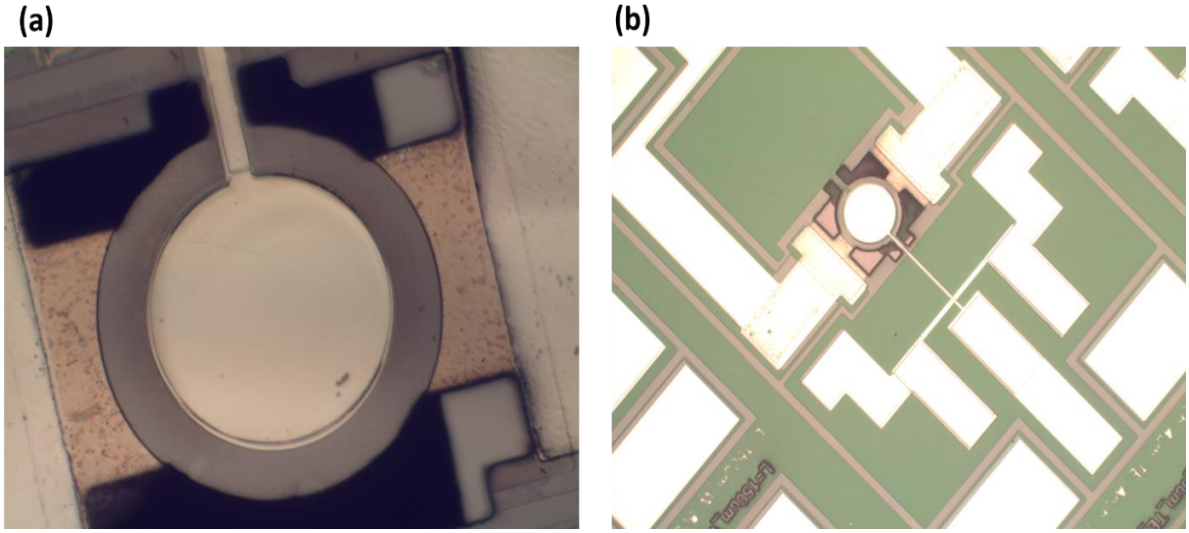

Figure 5.9 – Top-view microscope image of the fabricated hybrid resonator after etching the Zno to define the resonator body.

At this point, the gap layer is removed, and the device is ready for piezoelectric fabrication steps. The bottom electrode is deposited and patterned by a lift-off process, followed by 500 nm of sputtered ZnO onto the entire wafer. Then, ZnO is etched by diluted HCl, which is called via step to reach the bottom electrode. Afterward, the top electrode is deposited and patterned by lift-off, as seen in Figure 5.8. As shown in Figure 5.9, DRIE etch was used to define the resonator

body and to define isolation between ports and ground. Now, the device is already released from the backside and ready to be measured. However, if more release is needed, devices can be dipped in AZ 726 developer for few minutes to remove the remaining residues of the ALD layer gap. It is worthwhile mentioning that many chemical etchant selectivity tests were performed to find that AZ 726 developer as a chosen etchant that will attack only Al2O3, which makes the final device releasing step possible. SEM picture of the fabricated hybrid resonator is shown in Figure 5.11 and Figure 5.12.

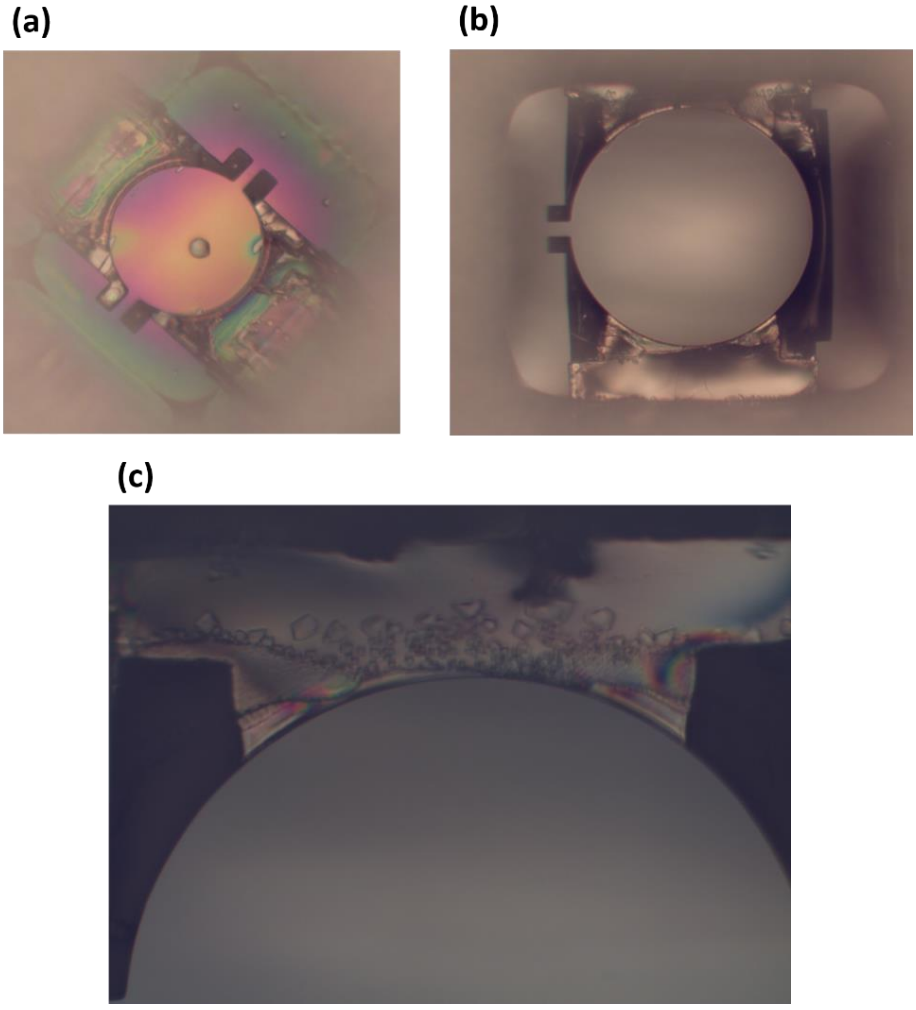

Figure 5.10 – Microscope image of suspended device from the backside; (a) before and (b) and (c) after backside release of HAR DRIE Si etch.

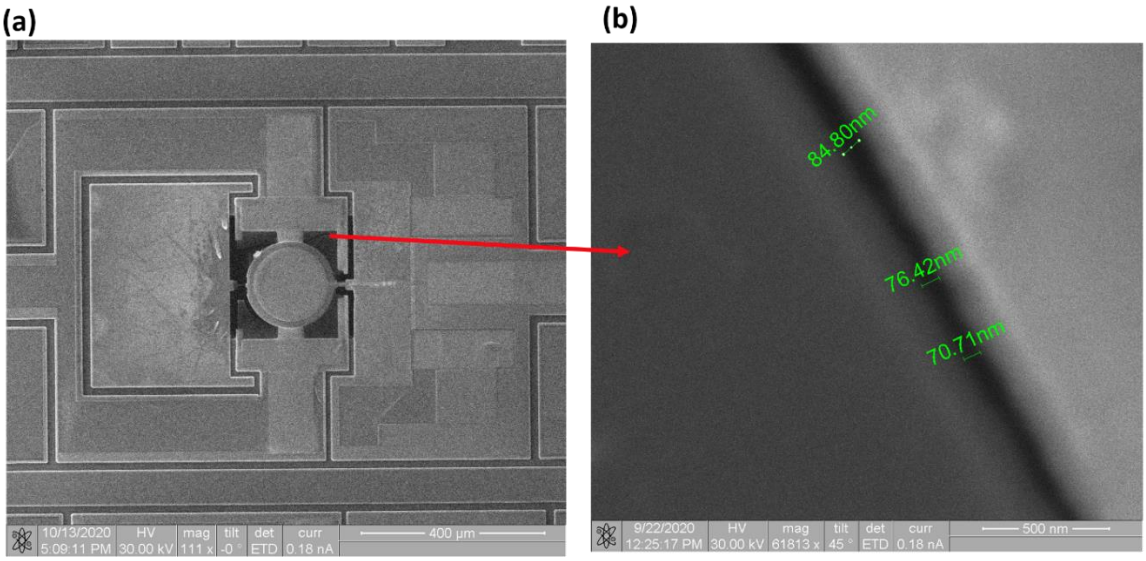

Figure 5.11 – SEM image of a suspended device after backside release with a 75 nm air-capacitive gap.

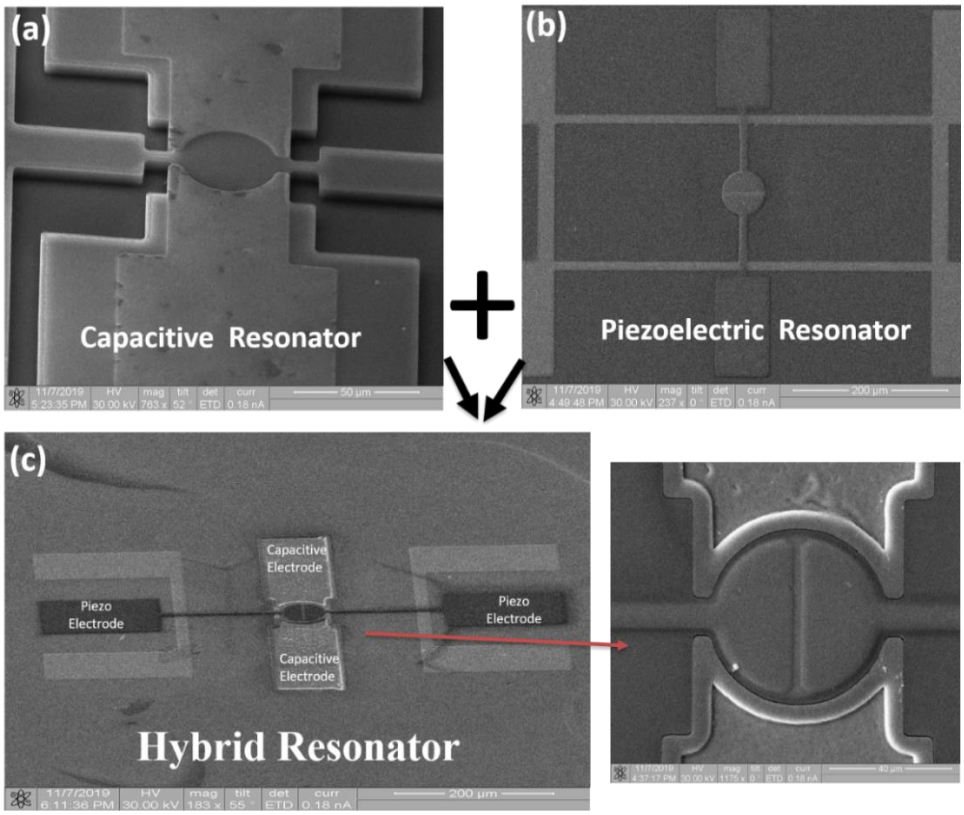

Figure 5.12 – SEM pictures showing fabricated (a) capacitive resonator; (b) piezoelectric resonator; (c) combining both capacitive and piezoelectric resonators in a newly proposed hybrid resonator.

5.3 The Device Structure and Operation

By sharing a lateral extensional contour-mode device configuration, the resonance frequencies of both piezoelectrically-transduced and electrostatically-transduced MEMS resonators inside a hybrid resonator are both determined by the in-plane lateral dimensions of the shared micromechanical resonator body. This resonator design configuration allows multiple resonators to operate at different frequencies on the same substrate from a single fabrication run. The incorporation of low acoustic loss single crystalline silicon as the structural material and the advantage of the additional influx of acoustic energy from capacitive actuation is anticipated to improve both the linearity and the quality factor of the proposed hybrid resonators. The purpose of this work is to have a study of different effects of this combination. As shown in Figure 5.6, the hybrid device consists of a doped silicon resonator body, which is designed to be mechanically vibrated at the designed resonance frequency in the desired mode shape (e.g., wine glass and radial contour mode, etc.). The resonator body is suspended by two or four anchors over the substrate. In order to excite the wine glass and contour modes in a circular disk-shaped resonator while minimizing the anchor related losses, the supporting tethers are strategically located at the quasi-nodal locations where the resonator plate does not have any radial displacement to minimize the loss of acoustic energy through the anchors. The suspended beam is surrounded by electroplated nickel electrodes with a specified gap thickness to perform the electrostatic actuation. A thin layer of piezoelectric material (ZnO) is placed on top of the resonator body, which is sandwiched between two layers of metals. The top metal layer is patterned to form the drive and sense electrodes while the bottom metal layer forms the ground plane. By leveraging the d_{31} piezoelectric coefficients of the ZnO layer, the contour mode resonance can be readily excited and detected.

There are four different transduction configurations to operate the proposed hybrid MEMS resonator device, including (1) capacitive drive and piezoelectric sense; (2) piezoelectric drive and capacitive sense; (3) both piezoelectric and capacitive drive and capacitive only sense; (3) both piezoelectric and capacitive drive and piezoelectric only sense. More detailed explanations are given below, while the conceptual illustrations are shown in Figure 15.13.

5.3.1 Capacitive Drive and Piezoelectric Sense

To operate the device, a DC bias voltage is applied to both input and output capacitive electrodes to generate electrostatic potential in the capacitive gap, which is located between the electrodes and the body of the resonator. Then, an AC signal is also applied to both capacitive electrodes to generate a variable potential, which triggers a time-varying electrostatic activation force, which excites the resonator into its resonance once the frequency of the input drive matches the resonant frequency. This effect is closely related to a time-varying parallel plate capacitive transducer, which causes mechanical modal vibration of the Si device layer. This deformation is directly proportional to the strength of the electric field and to the equivalent acoustic velocity (V_{eq}) within the piezoelectric material crystal layer. The mechanical deformation in the form of modal vibration during resonance directly affects the internal electric polarization of the piezoelectric layer, which will excite the acoustic wave to be converted back to the electrical signal known as the direct piezoelectric effect through the output electrodes where it can be detected. The output motional current (i_0) can be measured from the piezoelectric electrodes to obtain the frequency and electrical characteristics of the devices.

In this case, a reduction in the resonance frequency is expected with the increase of an optional tuning voltage through one of the capacitive transducers due to the so-called spring softening effect, which adds the extra benefit of electrostatic tuning for such a hybrid resonator.

In addition, the feedthrough should be reduced as the hybrid design has excellent inter-electrode isolation.

5.3.2 Piezoelectric Drive and Capacitive Sense

In this case, the operation of the device is slightly different. When an AC signal is applied to the piezoelectric electrodes, and it matches the natural resonant frequencies of the piezoelectric layer (piezo-resonator), mechanical deformation is induced (indirect piezoelectric effect). The resultant deformation is proportional to the equivalent longitudinal acoustic wave propagation within the piezo-material (ZnO) crystal layer. The mechanical deformation during resonance directly affects the internal polarization of the piezoelectric layer resulting in an electric response (the direct piezoelectric effect) that can be extracted and detected in this case from the capacitive sensing electrode as only DC bias is applied to the capacitive electrodes, which generate a motional output current. The motional current is generated due to the resonant movement of the capacitive transducer air gap that is charged by the DC bias voltage but driven to motion by the piezoelectric transducer.

Detection of output motional current by capacitive electrodes has many advantages as capacitive transduction tends to be much less prone to spurious modes. Capacitive transducers are designed to have an effective detection only if the resonant motion is in the desired mode shape that matches with the location and shape of the capacitive transducer electrodes. In this case, more energy can be saved as the device is in standby mode (with zero volts) to act as a resonator switch. In addition, using one resonator to drive and the other to sense will likely offer a chance to decouple the signal path between the drive and sense electrodes, which should lead to feedthrough level reduction.

5.3.3 Piezoelectric and Capacitive Drive and Capacitive Only Sense

In this scheme, an AC signal is applied to both of the two piezoelectric electrodes along with one capacitive electrode in order to operate the device. These electrodes are positioned to actuate the device to the targeted resonance of a lateral extensional contour-mode. DC bias is applied to both capacitive electrodes to measure the output motional current (i_0) from one sense electrode. As mentioned before, detecting by the capacitive electrode is expected to suppress the spurious modes, while the signal stays strong as piezoelectric electrodes are also used for actuating the device. In addition, frequency tuning is provided the increase of the potential voltage due to the spring softening effect, which adds the advantage of electrostatic tuning in this device operation scheme. The detected signal is strong as both capacitive and piezoelectric resonators are driving the device, and this configuration is anticipated to also result in a higher Q-factor due to the employment of capacitive sensing for the output current.

5.3.4 Piezoelectric and Capacitive Drive and Piezoelectric Only Sense

In this configuration, an AC signal is applied to one piezoelectric electrode and both capacitive electrodes in order to activate the device. A DC bias voltage is applied to both capacitive electrodes to generate the electrostatic actuation potential in the capacitive transducer gaps of the actuation capacitive transducer electrodes. Finally, the output motional current (i_0) can be measured from the piezoelectric sense electrodes to obtain the frequency and electrical characteristics of the devices.

In this case, both the insertion loss and the quality factor should be improved due to the additional influx of acoustic energy from capacitive actuation, which may also offer an improvement in the Q-factor. And the motional resistance is expected to be reduced due to the combined effects of the use of piezoelectric actuation and the additional capacitive motional

current contribution by the two capacitive transducers. However, in addition to exciting the device to its desired resonance frequency and mode shape, piezoelectric transduction is known to be susceptible to also actuate other out of lane spurious modes. This issue will be carefully investigated, as well.

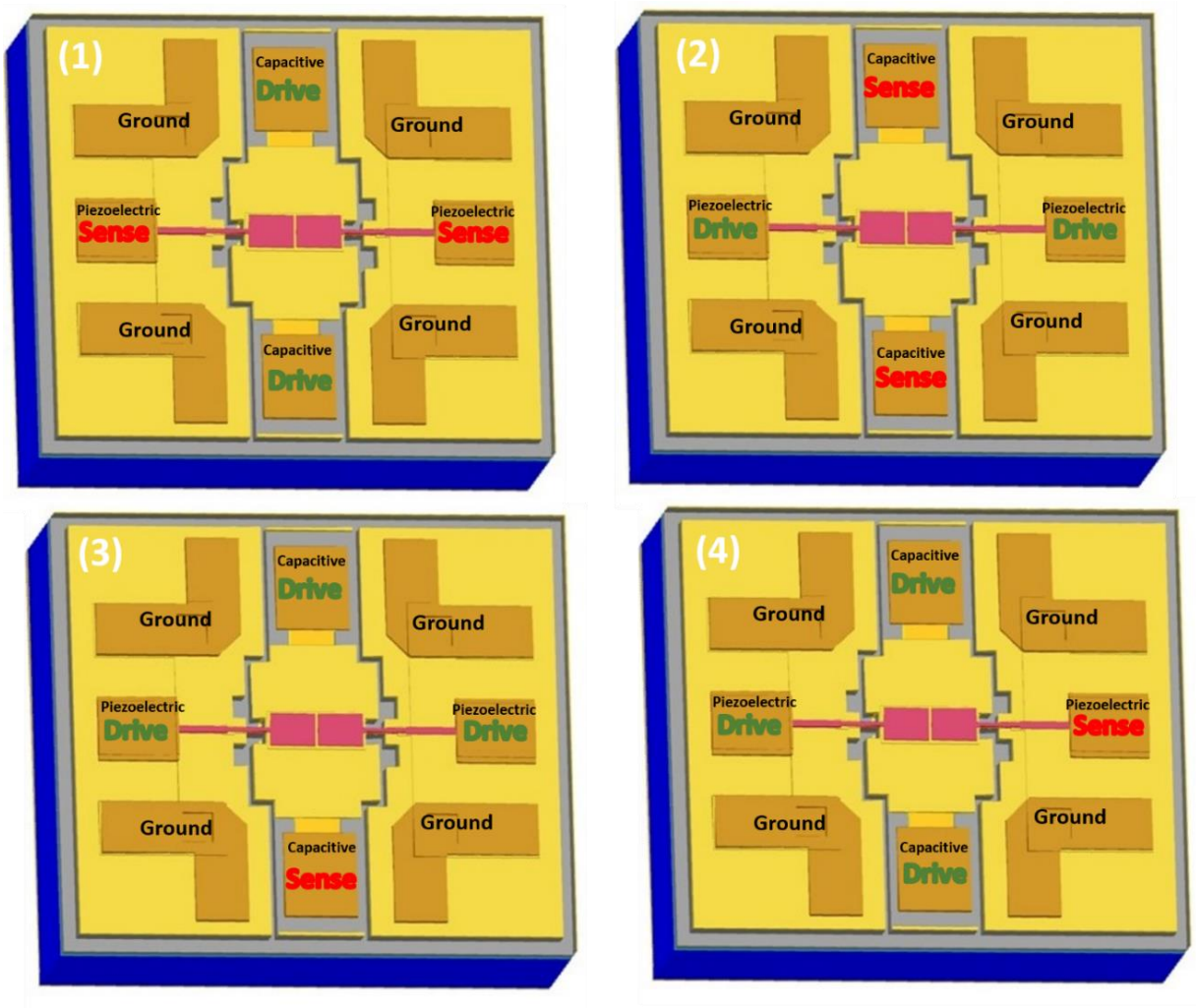

Figure 5.13 – Conceptual illustration of different transduction mechanisms to operate the proposed hybrid MEMS resonator device by showing: (1) capacitive drive and piezoelectric sense; (2) piezoelectric drive and capacitive sense; (3) both piezoelectric and capacitive drive and capacitive only sense; (3) both piezoelectric and capacitive drive and piezoelectric only sense. All of these configurations will be investigated by this work and they are detailed in this chapter.

5.4 Hybrid Probing 2-Ports Set-Up

The fabricated hybrid MEMS resonator devices have been tested by on-wafer probing using an RF probe station under atmospheric pressure and room temperature after performing a Short-Open-Load-Thru calibration using GGB CS-5 calibration kit to bring the reference to the probe tips. Some hybrid devices were shorting out after a low biasing voltage was applied, which implies that particles are finding their way into the air gaps between the capacitive electrodes and the resonator body during the release process. This problem often happens when MEMS devices are dried using solvent under atmospheric pressure as the solvent tends to be drawn along with other particles into the released air gap area by the capillary forces [58]. To solve this problem, a critical CO2 drying system should be used right after wet HF etchant gap spacing oxide removal.

The device in Figure 5.14 is designed to have two capacitive electrodes surrounding the resonator body to act as the first capacitive port. The other port is on top of the piezoelectric layer that is sitting on the resonator body to operate as the piezoelectric electrode. A direct two-port measurement set-up using a VNA and a power supply, as shown in Figure 5.16, was adopted to measure the S-parameter frequency responses and extract quality factor and resonance frequency. The device is designed to be measured by two different methods. In the first method, there is no need to use a bias tee as the DC bias voltage is applied directly to the resonator body through the piezoelectric bottom electrodes where the ground is fully isolated from the device. As shown in Figure 5.14 (a), the device can be actuated by applying an AC signal to the capacitive electrodes, and the output current can be detected from the piezoelectric top electrode, and vice versa. Another way to operate the device is by using a bias tee to apply both AC and DC voltage to the capacitive electrodes, while the generated motional current can be detected from the top piezoelectric electrode as indicated in Figure 5.14 (b).

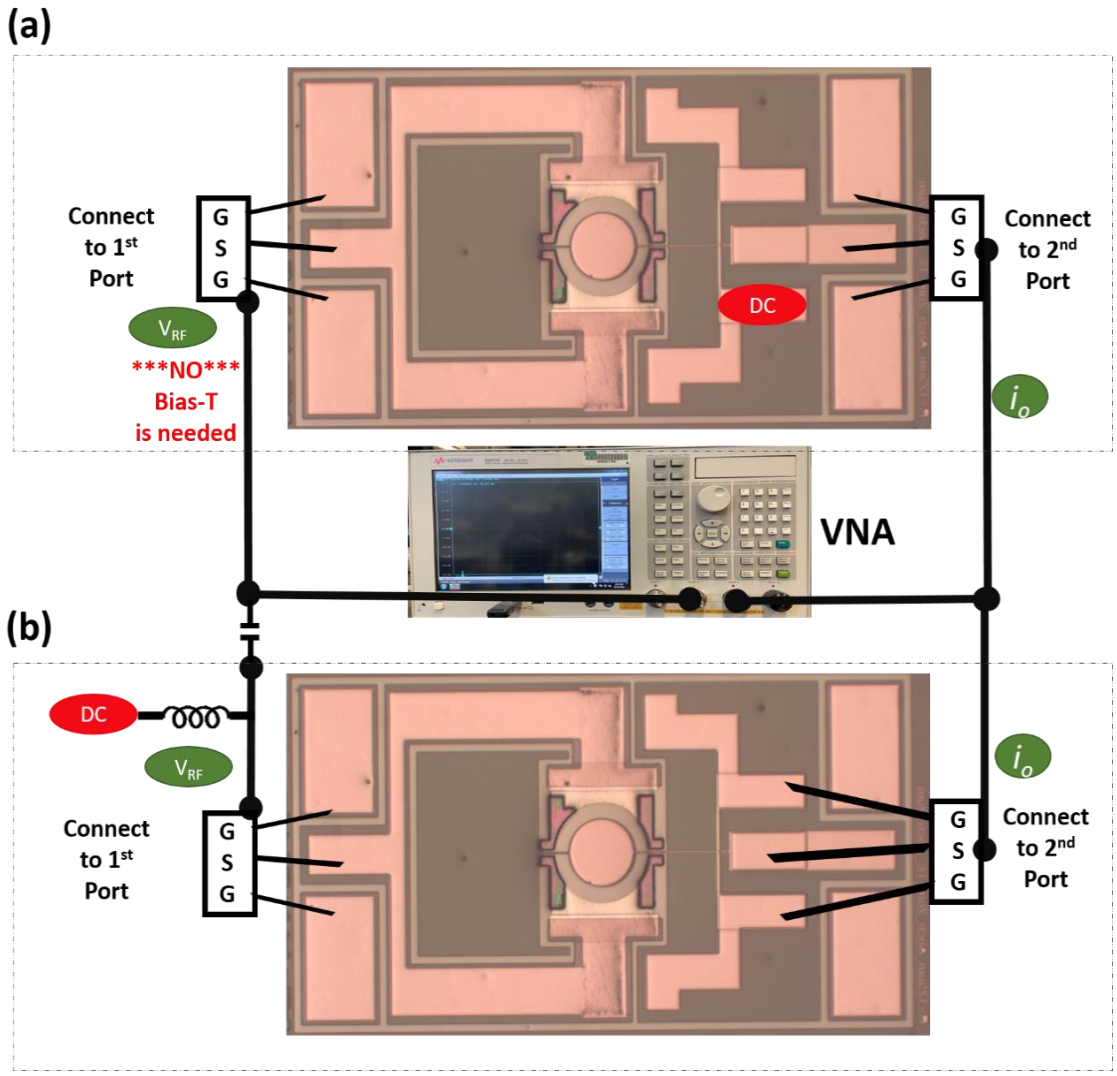

Figure 5.14 – Illustration of RF test set-up for the RF measurements of hybrid devices with one capacitive port and one piezoelectric port, which are fully isolated by the resonator body.

Feedthrough measurements have been performed, as shown in Figure 5.15, to capture the parasitic feedthrough effect at high frequency in piezoelectric, capacitive, and hybrid resonators. The feedthrough mechanism usually occurs when the electrical signal that travels between the electrodes leaks directly through the substrate or through other parasitic couplings instead of going through the electromechanical transformation of the resonator. In piezoelectric resonators, the leakage signal can travel through the substrate and the piezoelectric layer at a high frequency much more easily. As shown in the measured feedthrough level vs. frequency plots of Figure 5.15,

feedthrough suppression can be achieved even at high frequencies by using a hybrid resonator as a new device configuration. More than 30 dB of feedthrough suppression is observed as a result of actuating the resonator using capacitive electrodes and sensing from the fully isolated piezoelectric top electrode as compared with piezoelectric only or capacitive only resonators. Further reduction in feedthrough can be achieved by increasing the thickness of the piezo layer, which can result in a more than 50 dB reduction in feedthrough compare to piezoelectric only device counterparts.

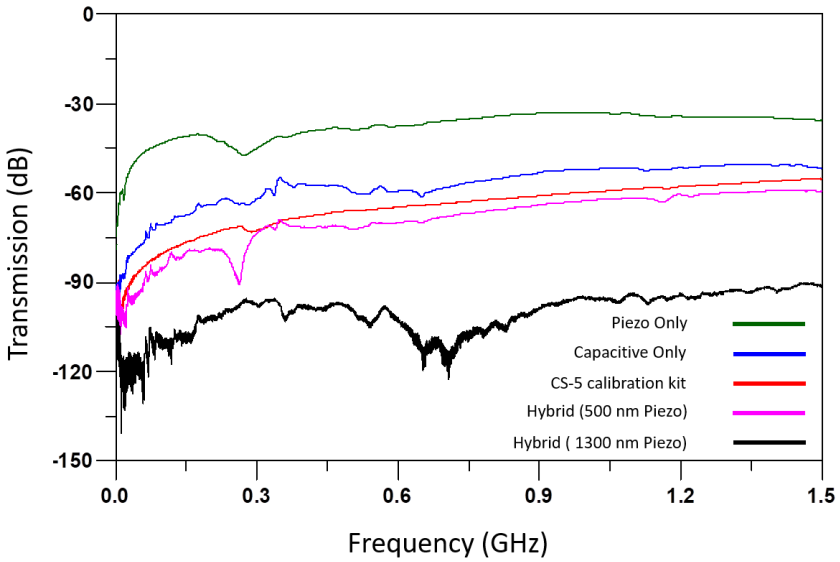

Figure 5.15 – Measured feedthrough levels versus frequency for piezoelectric only, capacitive only, and hybrid resonators with different thin-film piezoelectric transducer thicknesses.

Figure 5.17 and Figure 5.18 present the S-parameter responses of fabricated hybrid disk resonators operating in 1st and 4th contour modes. The disk resonator in Figure 5.17 is designed to have two 6 µm-wide side-supporting anchors and capacitive electrodes covering a smaller area, which has the advantages of easier and faster gap etching (releasing) process using the wet etchant as compared to the devices with capacitive electrodes covering a larger area. In addition, smaller electrodes require a lower DC voltage to actuate the resonator from the capacitive electrode port. However, the trade-off of shrinking the capacitive electrode areas is the reduction of the influx of

acoustic energy from capacitive actuation that decreases the quality factor, as seen in Figure 5.17. On the contrary, the disk resonator, as shown in Figure 5.18, is designed to have only one 10 µm-wide side-supporting anchor and its capacitive electrodes covering a larger area. As a result, the measured frequency responses of the hybrid disk resonators based on that design show significant improvement in terms of quality factor as compared to piezoelectric only resonators. The hybrid device demonstrates a loaded Q factor as high as ~29,000 in air by actuating the resonator from two large surrounding capacitive electrodes that enclose most of the resonator contour area. The motional current was detected from the top piezoelectric electrode, which is fully isolated from the other capacitive electrodes, thus resulting in a much lower feedthrough level, as seen in Figure 5.18.

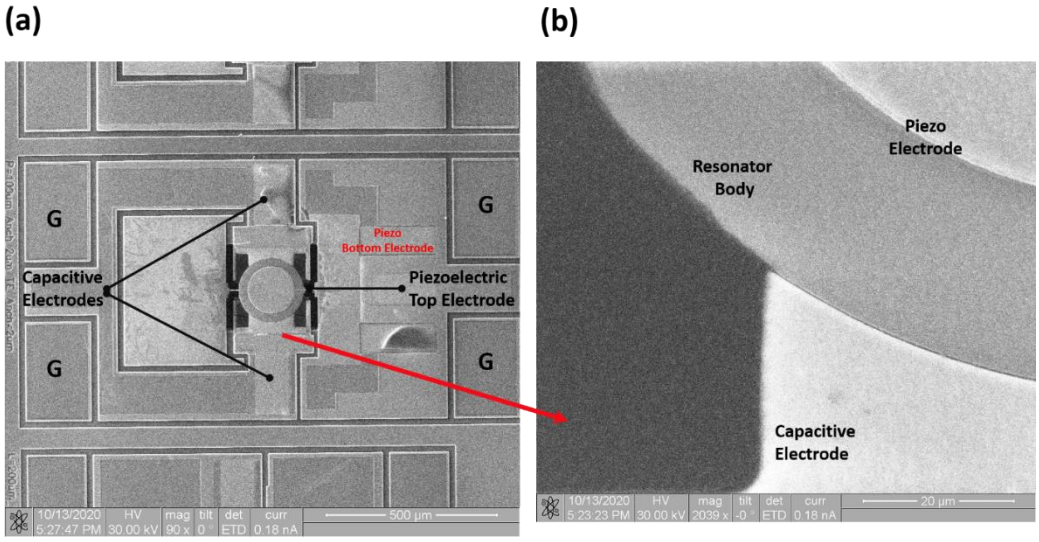

Figure 5.16 – Zoom-out and zoom-in top-view SEM images of fabricated hybrid resonators.

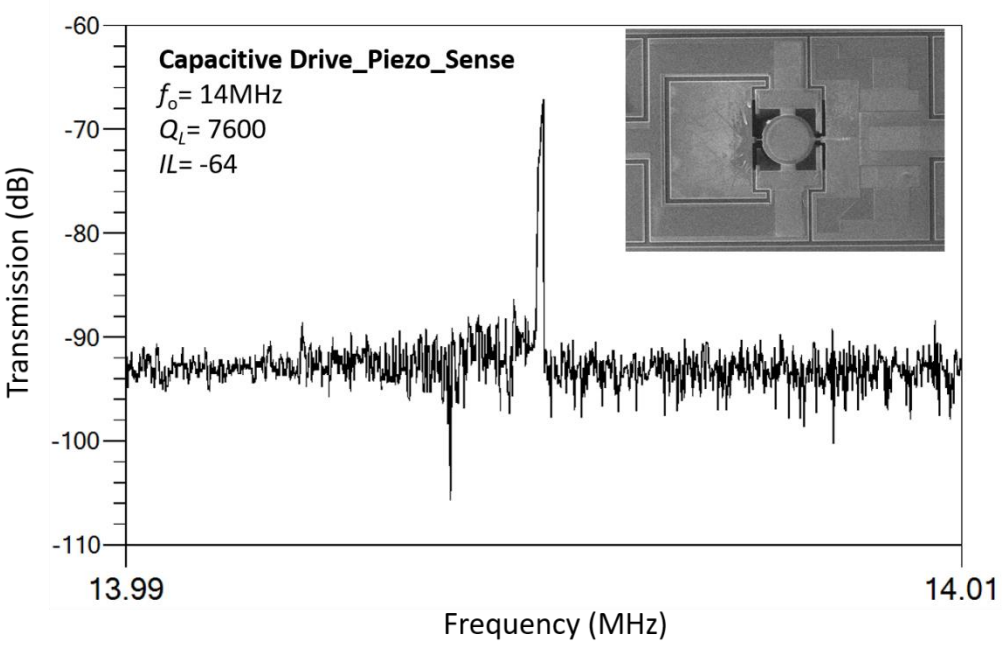

Figure 5.17 – Measured two-port forward transmission frequency response of the 1st contour mode thin-film hybrid disk resonator, which is actuated by the fully integrated capacitive transducer surrounding electrodes and detected by a piezoelectric transducer top electrode.

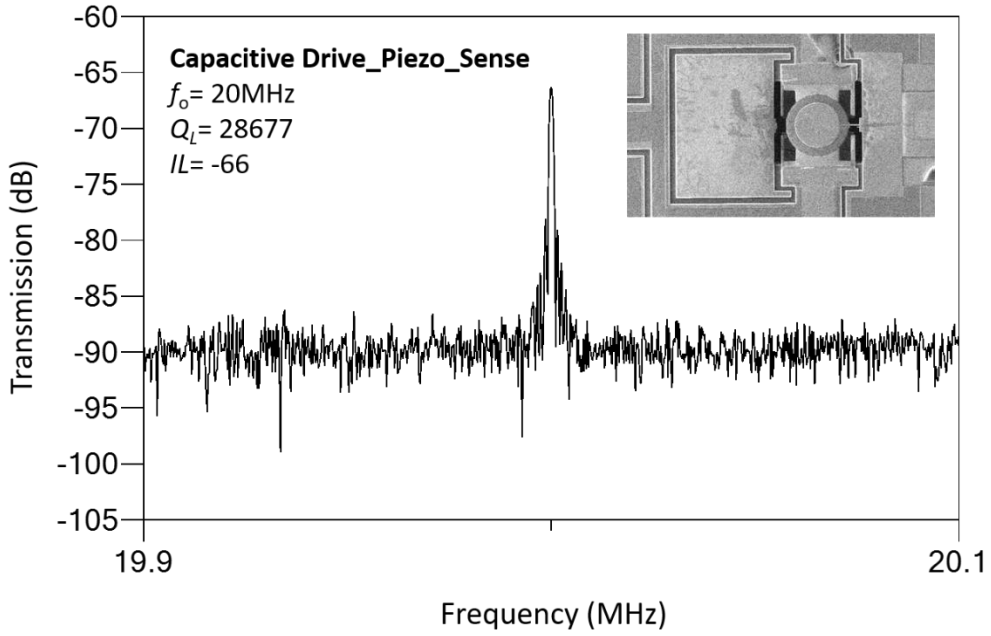

Figure 5.18 – Measured forward transmission frequency response of the 4th contour mode thin-film hybrid disk resonator, which is actuated by the fully integrated capacitive transducer surrounding electrodes and detected by a piezoelectric transducer top electrode.

Chapter 6: Micromechanical Filters Based on Capacitive, Piezoelectric and Hybrid Resonators

In this work, piezoelectric MEMS resonators have been developed as a complete system-on-a-chip solution to meet today's market demands. Resonator size needs to be reduced in order to achieve a higher operating frequency. As a trade-off, higher motional resistance is generated due to the lower electromechanical coupling coefficient (kt^2) as the transduction area is reduced. This issue can be solved by mechanically coupling several identical resonators into an array to reduce the overall effective motional resistance.

Mechanically coupling of several identically-sized disk resonators into an array solves this problem by reducing the motional resistance while the designed frequency is not changed. In the array design, the output current can be increased by a factor of the total number of the parallel-coupled resonators in the array while sharing the same input drive voltage, which will reduce the motional resistance by the number of the coupled resonators in the array. When the overall mechanically coupled filter structure vibrates at a designed modal frequency, the frequency is anticipated to match the frequency of the electrically coupled method as they naturally generate a single resonance response (same mode for each resonator) as all mechanically coupled resonators vibrate at exactly the same resonance frequency [55].

In this work, first efforts on mechanically coupling of a few resonators into an array for capacitive, piezoelectric, and hybrid array designs have been investigated as a viable system-level means to mitigate the motional impedance issue. All the resonators array studies are in the shape of a circular disk designed to operate in the contour-mode. The electrodes and anchors need to be

strategically designed to operate in desired resonant frequency and mode shape. The top and bottom electrodes were designed to match the strain field, which has enhanced the transverse piezoelectric coefficient (d_{31}) of ZnO/AlN thin film. This chapter details the design and implementation of the mechanically-coupled capacitive, piezoelectric, and hybrid MEMS resonators operating in their lateral extensional modes.

6.1 Device Operation

In this work, disk resonators were mechanically coupled by a longitudinal beam that acts as a string with a length equal to half the wavelength corresponding to the designed resonance frequency. The support beams act as anchors, which connect all the resonators to operate in the symmetric mode and asymmetric mode depends on the width of the anchor or method of transduction. Figure 6.1 shows the equivalent circuit model of the mechanically-coupled disk resonator. Under the first contour mode, all disk resonators move in phase while the coupling beams are stretching and compressing along with the resonators. The resonance frequency-shifted higher for the fourth contour mode of the disk resonator. However, for the higher-order mode of the disk resonator whose resonance frequency is much higher, the two resonators move 180o out-of-phase as the middle resonator doesn't necessarily force the beam to stretch too much since the coupling beams stay almost unstressed, which allow the other two resonators to move out of phase or moving in phase with each other's corresponding to three resonance peaks to shape the passband of a band-pass filter as shown in Figure 6.1.

6.2 Capacitively Transduced Resonator Array

Mechanically coupled-resonator array is a great system-level method that was previously used for lowering the motional resistance of capacitively transduced resonators while maintaining the high-quality factors achieved by capacitive MEMS resonators [57].

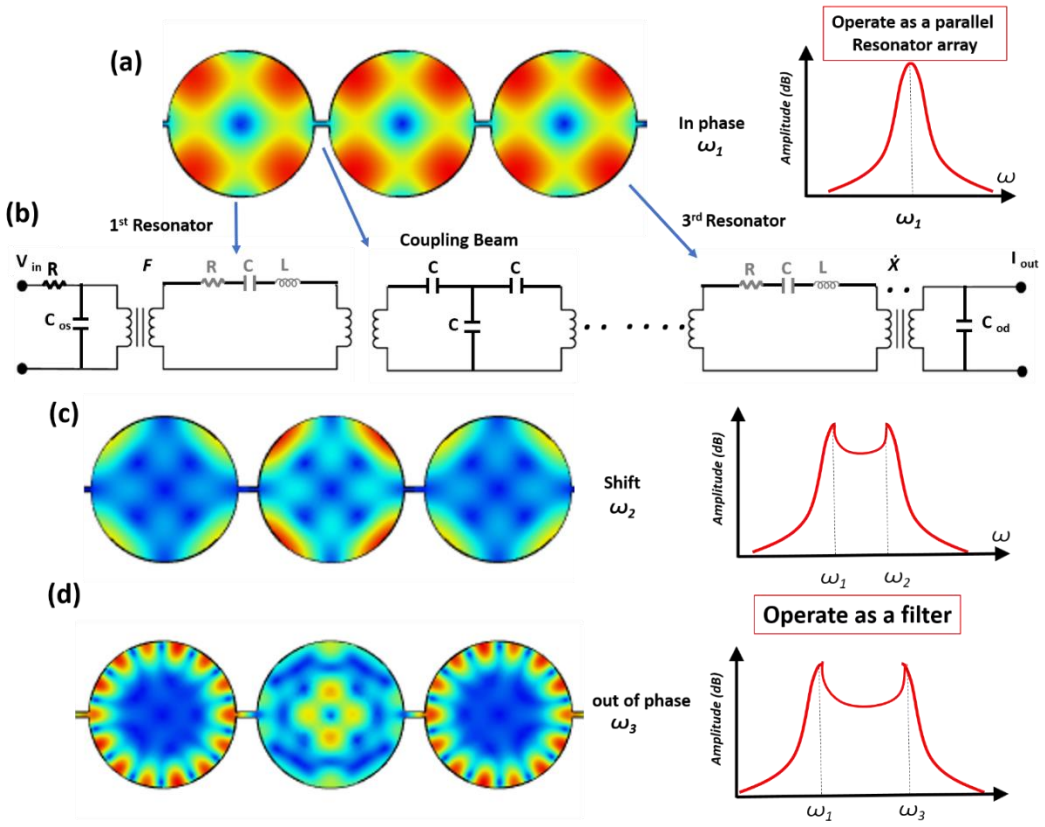

Figure 6.1 – Equivalent circuit of resonator array illustrating the in and out of phase shift where (a) all disk resonators move in phase; (b) the resonance frequency shifted higher for the fourth contour mode of the disk resonator; (c) two resonators move 180^o out-of-phase in the higher order mode of the disk resonator.

In this work, three disk resonators are mechanically coupled by a quarter wavelength longitudinal beam and surrounded by nickel-plated electrodes to provide phase flexibility for modal vibration in symmetrical and asymmetrical modes. The device operation is similar to the capacitive resonator that was described in Chapter 3. An electrostatic actuation force is generated as an AC voltage is applied to the input electrodes, while a DC-bias voltage is applied to the body of the resonator structure through the anchors to generate the electrostatic actuation potential across the capacitive transducer gaps. This results in a time-varying dc-biased capacitor between the input electrodes and the resonator body that leads to an output motional current (i_0), which can be measured from the output electrodes to obtain the electrical frequency characteristics of the

resonator devices. The electrodes were designed to produce in-phase or out-of-phase modes (0^o or 180^o phase difference), as shown in Figure 6.1. For the capacitively transduced resonator array, the effective insertion loss reduces accordingly based on the number of mechanically-coupled constituent resonators within the resonator. At the same time, the array quality factor may be lower than that of the constituent resonator, especially after reaching a certain number of mechanically-coupled parallel resonators, which limits the advantage of motional impedance reduction by implementing such kine of resonator array [21].

6.3 Piezoelectric Array

In this work, all the designs include three disk resonators mechanically coupled by a quarter wavelength long longitudinal beam connected through the nodal points to reduce the energy dissipation through the anchors, as shown in Figure 6.2. In a mechanically coupled array, the three resonates are synchronized to vibrate in phase at the same frequency as these resonators are designed to be coupled to each other strongly by using a half-wavelength coupling beam length, which results in a reduction of the insertion loss in this resonator filter. On the contrary, weak coupling method results in lower separation of the modes to define a narrower bandwidth of such a passband filter. This approach is particularly used in sensing applications such as multi-gas sensors systems application, which is also well-known as electronic-noses [56]. The piezoelectric resonators are excited and sensed by applying an AC signal, while the output motional current is detected through the top input and output electrodes. The mechanically-coupled array based on piezoelectric resonators is designed and fabricated in a ZnO/AlN-on-SOI MEMS fabrication process. The piezoelectric-on-SOI devices composed of a strategically chosen piezoelectric transducer and acoustic structural layer, which allows one more degree of freedom in design and performance optimization by combining a certain piezoelectric transducer material, such as

sputtered thin-film ZnO, which has a great electromechanical coupling coefficient but not so good acoustic properties (e.g., low acoustic velocity and high acoustic energy dissipations). Thus, single crystalline silicon as another potentially better acoustic structural material has been chosen for this work to implement thin-film piezoelectric on silicon (TPoS) resonators. More importantly, the employment of a much thicker (stress-free) silicon layer not only mitigates the built-in residual stress issue of the sputtered ZnO piezoelectric layer but also allows a greater amount of acoustic wave energy to be stored inside the resonator body for potentially lower energy dissipation per cycle thus leading to higher quality factor (Q). Wine-glass mode disk resonators have been investigated in this work based on its high resonance frequency and the ability to achieve lower motional resistance. Figure 6.1 illustrated the modal analysis of this array resonator using COMSOL ®. The electrodes should be designed to be matched with the strain field of the target resonance mode to strengthen the desired mode and to decrease the losses due to the excitation and acoustic energy leakage to other spurious modes.

Unlike capacitive resonators, where the electrodes do not contact and touch the resonator body, the electrodes in piezoelectric resonators are coupled directly to the resonator body, which results in maximal electric field strength to fortify the piezoelectric effect, but this would increase the material losses at the same time, which leads to a significant drop in the quality factor as compared to capacitive resonators. Although this approach of mechanically coupling piezoelectric resonators into an array results in a reduction of the motional impedance by increase the electrode-to-resonator interference area, the key figure of merit ($kt^2.Q$) does not significantly improve when higher frequency operation is needed. In essence, the electromechanical coupling coefficient and the quality factor start to degrade when excessive shrinking of the size of the resonator is needed to reach the ultra-high frequency (UHF) range.

In summary, both capacitive and piezoelectric mechanically coupled-resonator array design configurations can very nicely complement each other. Therefore, by combining both capacitive and piezoelectric arrays into one hybrid mechanically coupled-resonator array, the advantages of both these MEMS transduction technologies could be combined in one single array device including, high electromechanically coupling coefficient, high Q-factor, and additional functionalities such as on-off switching as detailed in the next section.

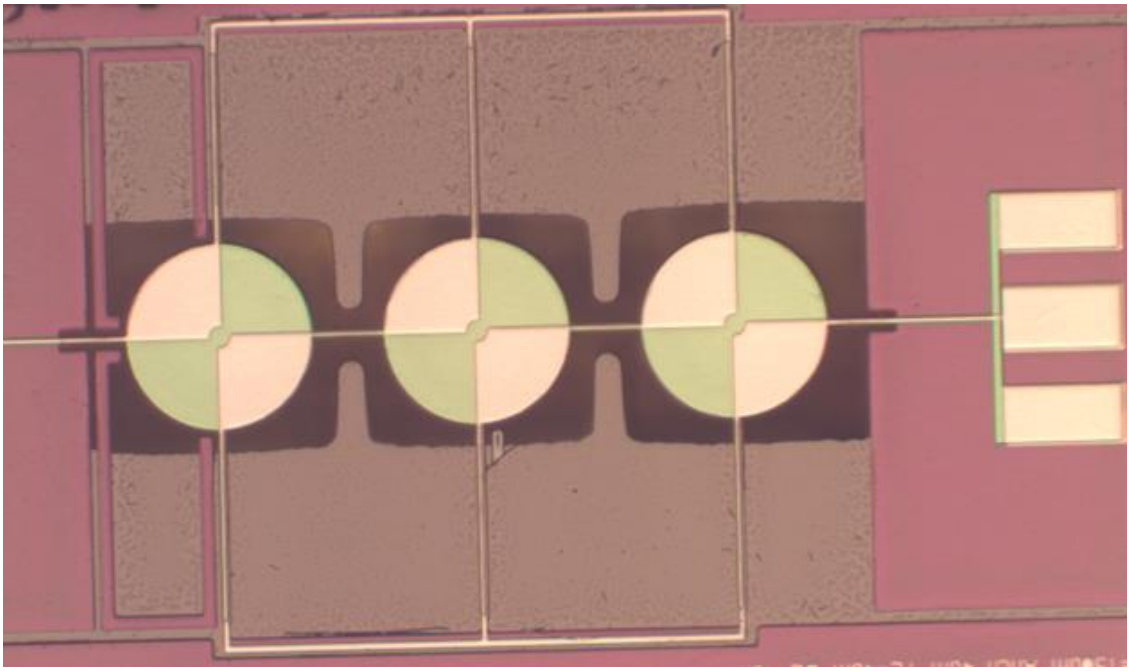

Figure 6.2 – Top-view microscope image of the fabricated piezoelectric array after the release.

6.4 Hybrid Array

Reducing the size of the micromechanical disk resonator is required to reach operating frequencies in the UHF range. As a result, the electromechanical coupling coefficient is anticipated to also degrade, which leads to increased motional resistance. Furthermore, the reduction of the motional impedance by using the mechanically coupled array was not enough to readily achieve the impedance matching to 50 Ω RF electronics. Further impedance reduction is necessary while maintaining a high-quality factor of these acoustic resonator devices. The new design proposed

herein combines both capacitive and piezoelectric transducers in a single array that can provide further improvement in terms of all the key performance metrics such as kt^2, Q-factor, and motional impedance (R_m). There are several different designs of mechanically coupled hybrid resonators in this work, which are detailed below:

6.4.1 A Hybrid Resonator Array Design with All Three Constituent Resonators Designed to Be Equipped with Both Piezoelectric and Capacitive Transducers and Electrodes

In this configuration, the array device can be piezoelectrically actuated and capacitively (electrostatically) sensed. Also, the device can be actuated capacitively while using the piezoelectric transducer for sensing purposes. Both approaches are anticipated to result in a significant reduction of the feedthrough noise, as the hybrid array design has excellent inter-electrode isolation that decouples the signal path between the drive and sense electrodes.

Another way to operate the device is to apply an AC signal to one electrode of both the piezoelectric and capacitive transducers while applying a DC bias voltage to one capacitive electrode to generate the electrostatic actuation potential in the capacitive transducer gaps of the capacitive transducer electrodes. Where the output motional current (i0) can be measured by both the piezoelectric and capacitive electrodes, which will lead to further improvement of both the insertion loss and the quality factor due to the additional influx of acoustic energy from capacitive actuation, and the motional resistance is expected to be reduced due to combined effects of the use of piezoelectric actuation and the additional capacitive motional current contribution through combined effects of both type of transducers as seen in Figure 6.3.

6.4.2 A Hybrid Array with Two Piezoelectric Outer Resonators and a Capacitive Inner Resonator

In this design, the inner resonator does not include piezoelectric electrodes, which results in reducing of the acoustic energy dissipations due to the metal electrode related losses in the inner

resonator, thus increasing the effective quality factor. At the same time, the inner resonator is surrounded by electroplated nickel electrodes separated by a small capacitive gap. The outer resonators include piezoelectric bottom and top electrodes that can be excited into the resonance by applying an AC voltage across and bottom electrodes of one of the resonator (the actuator resonator), which will generate a vertical electric field that will induce the lateral strain via the transverse piezoelectric coefficient (d_{31}) of the piezoelectric thin-film transducer material, therefore resulting all three resonators to vibrate at the designed frequency. The output motional current (i_0) can be measured from the other outer resonator's (the sensor resonator) electrodes to obtain the electrical frequency characteristics of the array, as seen in Figure 6.4.

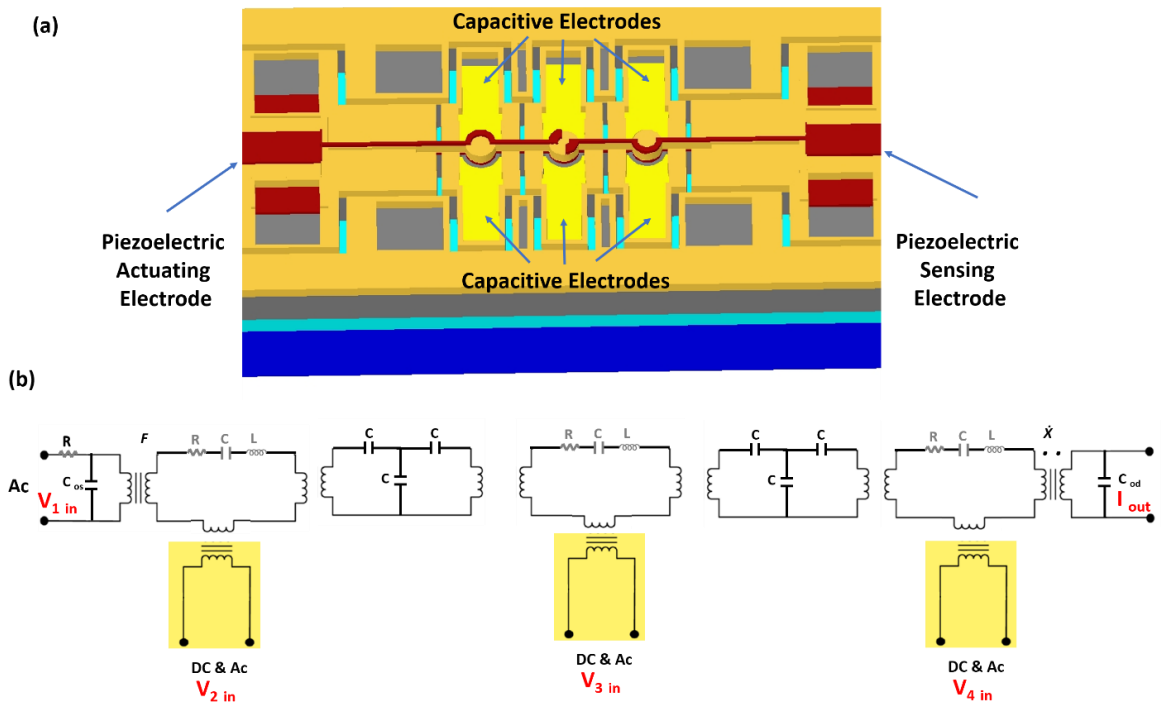

Figure 6.3 – Equivalent circuit of hybrid resonator array with fully integrated capacitive and piezoelectric transducers.

To further decrease the motional impedance and increase the quality factor, an Ac signal and DC bias voltage can be applied to the capacitive electrodes to generate the electrostatic actuation potential in the capacitive transducer gaps of the actuation capacitive transducer

electrodes, which results in an additional influx of acoustic energy from capacitive actuation. In this approach, the (kt^2.Q) of the resonator array will be improved by the number of the coupled arrays.

Another way to operate the device is to use the inner resonator to drive the array by applying an AC signal and DC bias voltage to the capacitive electrodes in order to activate the device. The output motional current (i_0) can be measured from the piezoelectric transducer electrode, which will likely offer a chance to decouple the signal path between the drive and sense electrodes. This should lead to substantial feedthrough level reduction. In addition, this array device can operate as a filter switch to be in the standby mode under zero-volt bias voltage to lower the power consumption.

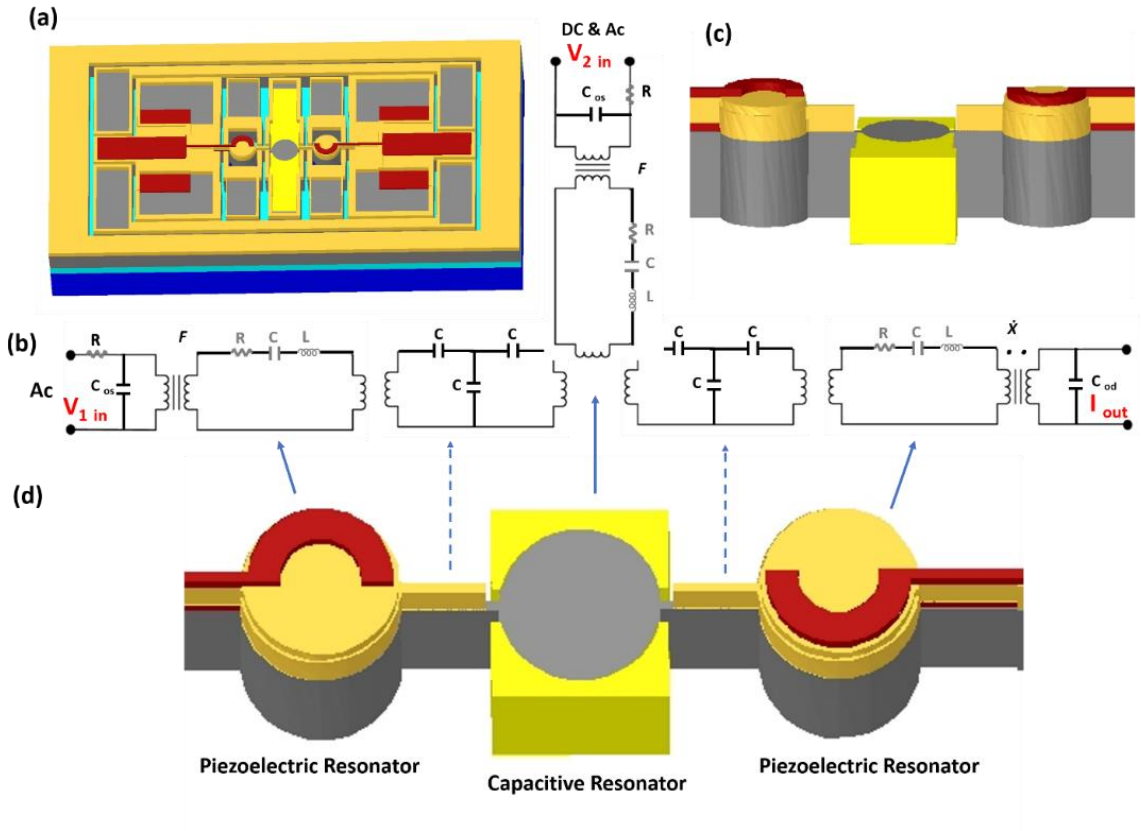

Figure 6.4 – Equivalent circuit of a hybrid resonator array, where the inner part is a capacitive resonator and the outer two devices are piezoelectric resonators.

6.5 Fabrication Process of the Hybrid Resonator Array

The hybrid resonator array fabrication process starts with the fabrication of the capacitive resonator as the inner resonator, followed by the building of the piezoelectric transducer structure on the top of the two outer resonators. Figure 6.5 illustrates the fabrication process of the hybrid array resonator. The step-by-step fabrication procedure is detailed as the following: (a) Using 12xt photoresist as a mask, the device layer of SOI wafer is patterned to define the Si vibrating resonator body by etching the Si using Bosch DRIE process to define the body of the capacitive inner resonator; (b) Then, a thin blanket layer of ALD gap-spacing dielectric film was deposited; (c) After that, the seed layer for the plating process was deposited followed by nickel plating via the photo-lithographically defined mold for surrounding electrode to form the capacitive electrodes; the wafer then undergoes CMP planarization until the Si interface is exposed completely; (d) The bottom electrode is deposited and patterned by lift-off on the outer resonators followed by RF sputtering of 500 nm-thick ZnO onto the entire wafer; (e) Then, ZnO is etched by diluted HCl solution to pattern the via hole to access to the bottom electrode. Then, the top electrode is deposited on top of the ZnO piezoelectric transducer layer over the outer resonators and patterned by lift-off; (f) Afterwards, the device is released from the backside by performing through-wafer etch using DRIE followed by SiO2 anisotropic directional dry etch to remove the oxide layer.

Thereafter, DRIE etch was used to define the resonator body as well as the isolation between ports and ground. Given that the device is already released from the backside and the entire wafer front-side surface is protected by 1512 photoresist except for the capacitive electrode area to remove the ALD gap-spacing layer by wet etching using 6:1 BOE. It is worthwhile mentioning that the inner resonator in this design is totally separated from the outer resonators

where the ZnO is deposited. This facilitates the wet etch, releasing the device using buffer HF etchant. Figure 6.6 presents the SEM photo of a fabricated hybrid resonator device.

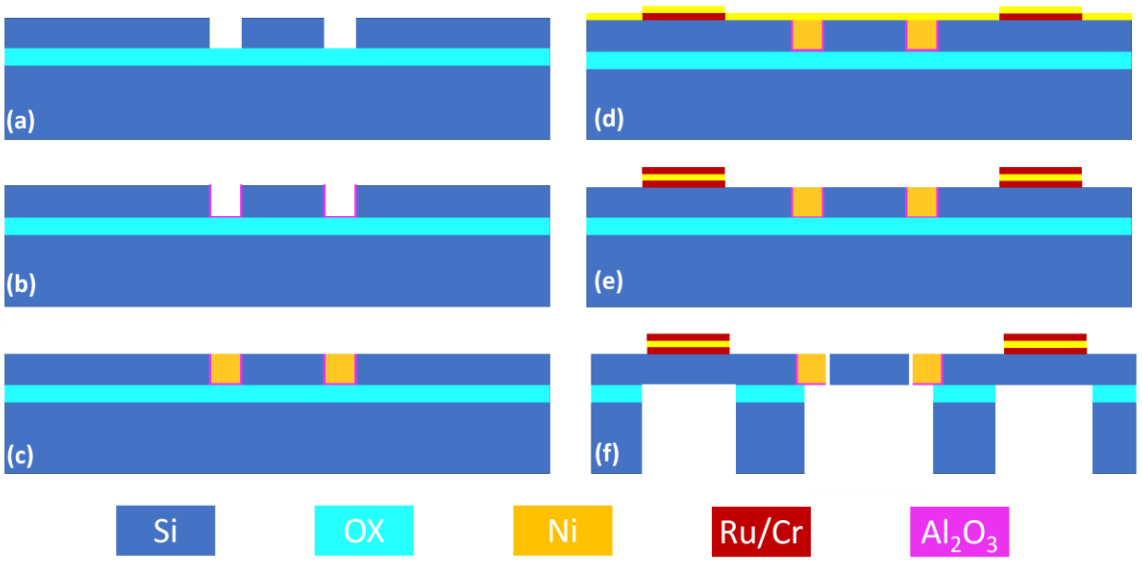

Figure 6.5 – Cross-sectional view illustration of the fabrication process flow of hybrid array resonator.

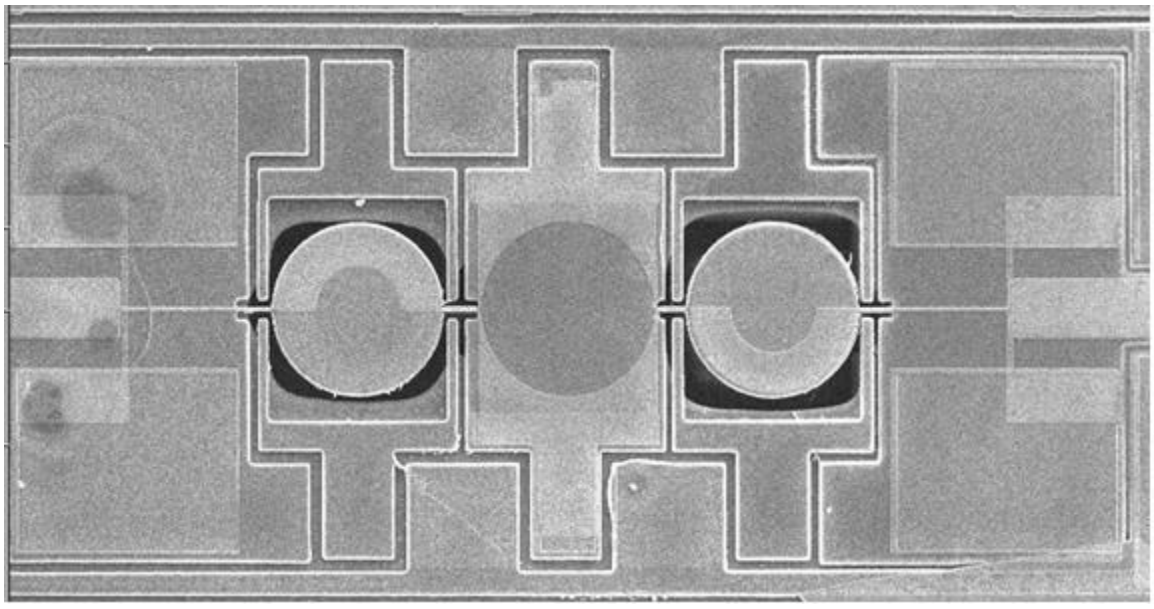

Figure 6.6 – SEM photo of a newly proposed hybrid resonator array with seamlessly integrated capacitive and piezoelectric transducers.

Chapter 7: Conclusions and Future Work

7.1 Conclusions

In this dissertation work, strategic designs to combine both piezoelectric and capacitive transducers in a newly proposed hybrid resonator have been thoroughly investigated. The primary goal of having dual transduction mechanisms consolidated into one resonator is to combine the advantages of the additional influx of acoustic energy from capacitive actuation that offers an improvement in terms of quality factor. Meanwhile, piezoelectric transduction is anticipated to lead to low insertion loss and small motional resistance while still retaining all the other benefits. These added benefits include self-switching capability, voltage-controlled configurability, better thermal stability, and electrostatic (capacitive) frequency tuning, which can all largely be ascribed to the capacitive transduction mechanism. For instance, electrostatic tuning is also expected to be able to leverage the spring softening effect through a capacitive tuning electrode, and the feedthrough noise level should be reduced as the newly proposed hybrid resonator design has excellent inter-electrode isolation. The newly proposed hybrid resonators have thoroughly investigated to exhibit superb performance, such as a loaded Q factor as high as ~29,000 in air and greater than 30 dB of feedthrough suppression as a result of actuating the resonator using the capacitive electrodes that surrounds the resonator body while sensing from the fully isolated piezoelectric electrode on top of the resonator body, as compared to the broadband response of piezoelectric only resonators.

In addition, a process optimization method has been developed to improve the sidewall smoothness of Bosch silicon deep reactive ion etching (DRIE) process. The proposed method has

exploited process pressure, C_4F_8/O_2 pulse time, SF_6 pulse time, the substrate temperature, as well as device structure related parameters such as trench opening size/depth to reduce the sidewall roughness that is crucial for capacitive transducers. The scalloping effect could increase the total effective capacitive air gap, thereby reducing the electrode-to-resonator overlap capacitance that is the key parameter affecting the motional resistance of a capacitive resonator. The modified recipe results in a 7x-9x reduction of the side scallop depth down to 42 nm and 31 nm in a wide-open field area and a narrow 1μm-wide trench opening, thus significantly lowering the effective air gap of capacitive transducer. It is observed the scallop depth gradually reduces with etching depth to 18 nm at a 28 μm depth from the top of the etched trench. Since the high motional resistance is the key remaining issue of capacitively transduced vibrating resonators, this work could pave the way for future capacitive MEMS resonator batch microfabrication by using DRIE.

Furthermore, a systematic investigation of post-fabrication annealing was performed for ZnO-on-Ni/Si MEMS lateral extensional mode resonators by using localized annealing process by Joule heating effect, which resulted in a significant improvement in the overall performance of both nickel and silicon resonators. The measured Q's and insertion losses have been improved as a result of enhancing the material properties due to the localized annealing. On the other hand, the metal on the surface of the resonator was sometimes melted and diffused into the body of the resonator as a result of excessive and rapid Joule heating during localized annealing to a very high temperature, which shifted the resonant frequency based on the properties of the deposited metal.

7.2 Future Work

Instead of defining the sub-90nm transducer gap, a wide variety of high-k dielectric thin films with permittivity much higher than that of air including Al_2O_3 (εr=8), ZrO2 (εr=12.5), HfO_2 (εr=25), and TiO_2 (εr=80) [59] can be used similarly by taking advantage of the ALD's precisely

controlled thickness (30 nm or much lower) to serve as the solid gap for the hybrid resonator, which is expected to provide a better transducer efficiency as a result of the higher permittivity in the high-k dielectric thin films. Additionally, large air-gaps on already fabricated hybrid resonators can be partially refilled by an ALD high-k layer, which will result in shrinking of the 100 nm-wide released air gap to 40 nm or less to reduce the motional resistance of the hybrid resonator.

Piezoelectrically and capacitively transduced resonators have proven themselves to be an excellent candidate for wireless multi-frequency applications. However, even with the high quality and low insertion loss, their performance can be improved further as it has not reached its limitation yet. Actuating the hybrid resonator using two or more ports (electrodes) at the same time with the fully integrated piezoelectric and capacitive transducers could improve the overall performance even more. In addition, increasing the thickness of the single crystalline silicon resonator structural layer to store more acoustic energy inside the resonator body can increase the performance of the hybrid resonator.

A MEMS resonator with 4 capacitive electrodes and 4 piezoelectric electrodes has been successfully fabricated in this work, which is equipped with 8 isolated and individually accessible probe pads (ports), which is named as hybrid spider resonator by us. The hybrid spider resonator can be tested by using 4 ports in the VNA and "dual RF picoprobes," as illustrated in Figure 7.1. This hybrid spider resonator is designed to include four differential probe pads that are patterned for RF probe measurements by using four GSGSG probes. Each GSGSG probe can be connected to one VNA port to either actuate or sense one capacitive/piezoelectric electrode in each port, as depicted in Figure 7.2 and Figure 7.3. This new design will give additional functionalities such as on-off switching, frequency tuning, and much more.

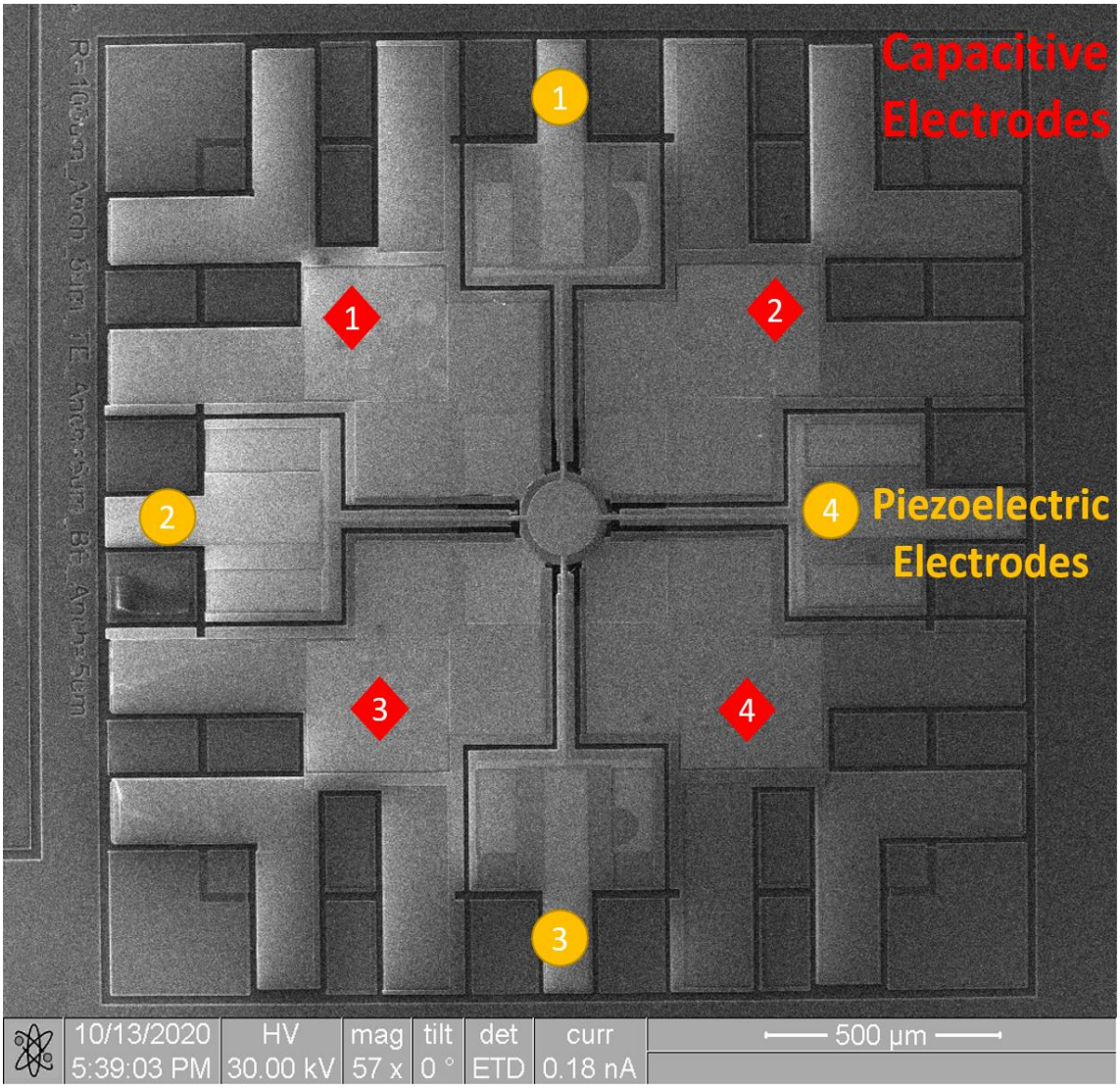

Figure 7.1 – SEM pictures showing fabricated hybrid spider MEMS resonator with 4 capacitive electrodes and 4 piezoelectric electrodes, which is the first demonstration of devices of its kind.

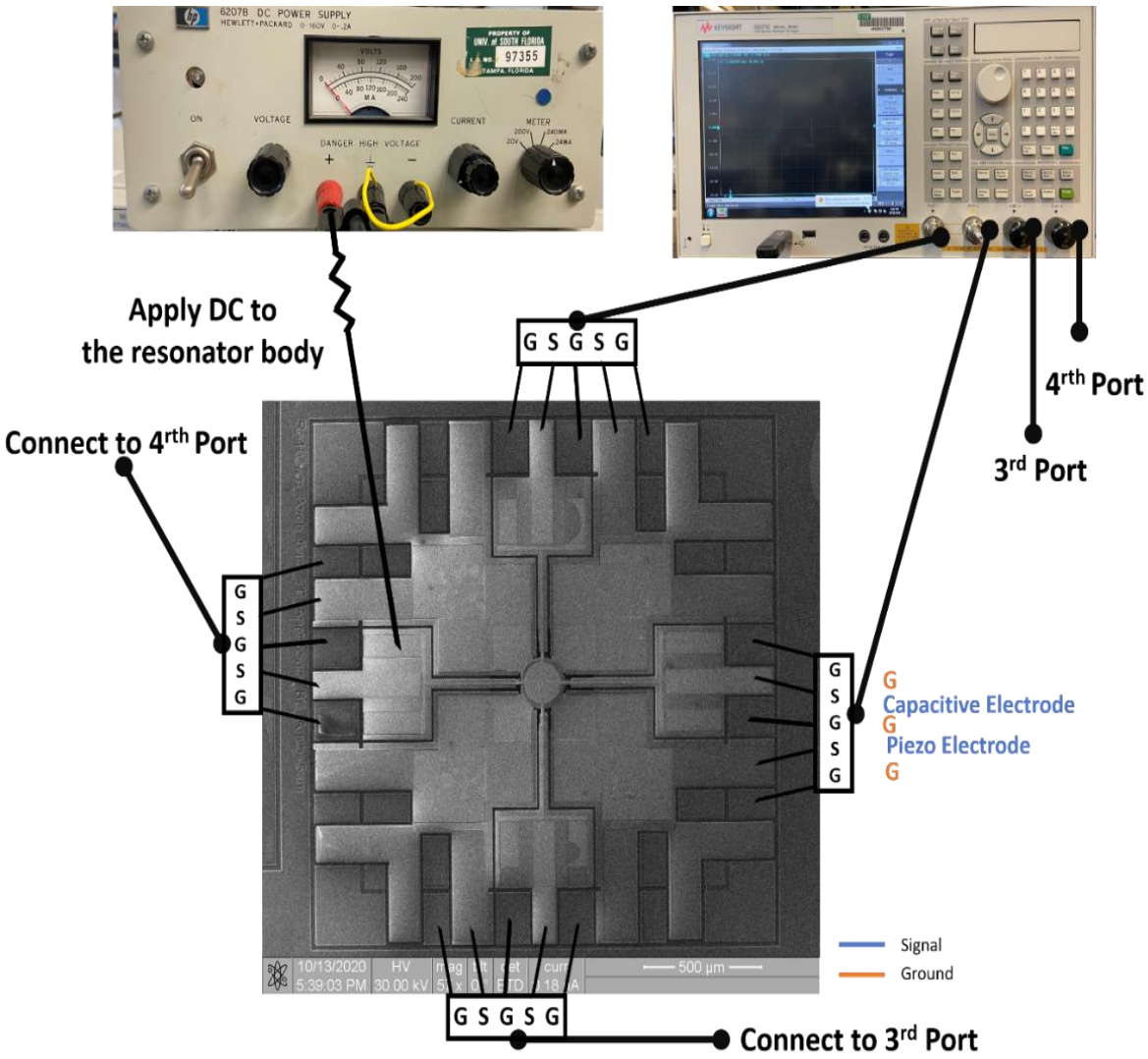

Figure 7.2 – Illustration of RF probe measurement set-up for hybrid spider device with 8 ports.

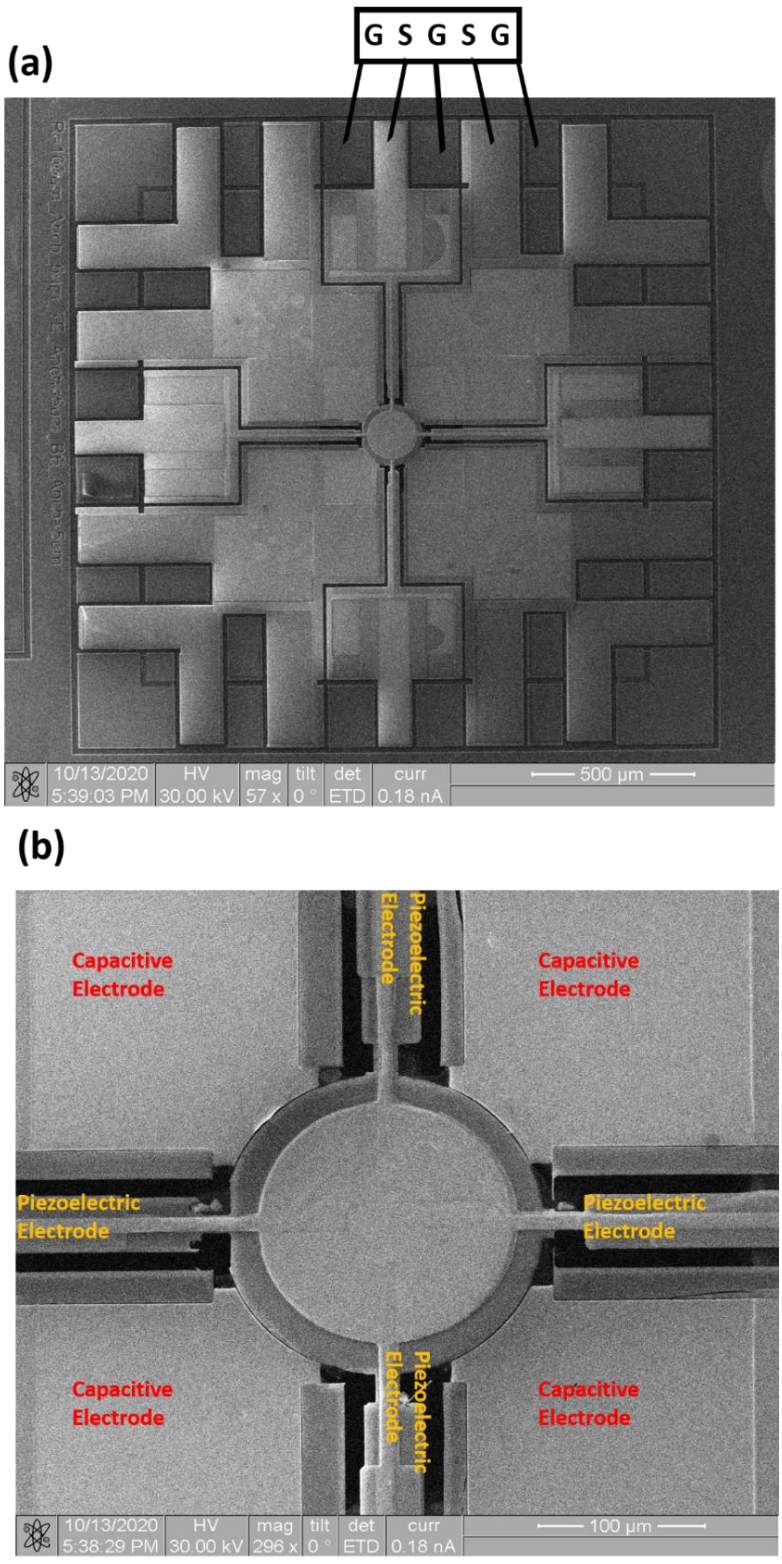

Figure 7.3 – Illustration of the capacitive and piezoelectric electrodes of hybrid spider resonator.

References

[1] C. T.-C. Nguyen and R. T. Howe, “Polysilicon microresonators for signal processing,” *Digest of Papers, Government Microcircuit and Applications Conference,* San Diego, CA, Aug. 15, 1994, pp. 195-198.

[2] Kun. Wang, Ark-Chew. Wong, Nguyen. C.T.-C., "VHF free-free beam high-Q micromechanical resonators," *Microelectromechanical Systems, Journal of,* vol.9, no.3, pp.347-360, Sep 2000.

[3] J. R. Clark, W.-T. Hsu, and C. T.-C. Nguyen, “High-Q VHF micromechanical contour-mode disk resonators,” in Tech. Digest, *IEEE Int. Electron Devices Meeting*, San Francisco, CA, Dec. 11–13, 2000, pp. 399–402.

[4] J. Wang, Z. Ren, and C.-C. Nguyen, "1.156-GHz self-aligned vibrating micromechanical disk resonator," *Ultrasonics, Ferroelectrics and Frequency Control, IEEE Transactions on,* vol. 51, pp. 1607-1628, 2004.

[5] M. A. Abdelmoneum, M. U. Demirci, and C. T. C. Nguyen, "Stemless wine-glass-mode disk micromechanical resonators," in *Micro Electro Mechanical Systems, 2003. MEMS-03 Kyoto. IEEE The Sixteenth Annual International Conference on*, 2003, pp. 698-701.

[6] H. Li-Wen, C. T. C. Nguyen, X. Yuan, L. Yu-Wei, L. Sheng-Shian, and R. Zeying, "UHF Micromechanical Compound-(2,4) Mode Ring Resonators With Solid-Gap Transducers," in *Frequency Control Symposium, 2007 Joint with the 21st European Frequency and Time Forum. IEEE International*, 2007, pp. 1370-1375.

[7] D. Weinstein and S. A. Bhave, "Internal dielectric transduction in bulk-mode resonators," *Microelectromechanical Systems, Journal of,* vol. 18, pp. 1401-1408, 2009.

[8] K. Lakin and J. Wang, "UHF composite bulk wave resonators," in *1980 Ultrasonics Symposium*, 1980, pp. 834-837.

[9] Y. Satoh, T. Nishihara, T. Yokoyama, M. Ueda, and T. Miyashita, "Development of Piezoelectric Thin Film Resonator and Its Impact on Future Wireless Communication Systems," *Japanese Journal of Applied Physics*, vol. 44, pp. 2883-2894, 2005.

[10] G. Piazza, P. J. Stephanou, and A. P. Pisano, "One and two port piezoelectric higher order contour-mode MEMS resonators for mechanical signal processing," *Solid-State Electronics*, vol. 51, pp. 1596-1608, 2007.

[11] R. Abdolvand, H. M. Lavasani, G. K. Ho, and F. Ayazi, "Thin-film piezoelectric-on-silicon resonators for high-frequency reference oscillator applications," *Ultrasonics, Ferroelectrics, and Frequency Control, IEEE Transactions on*, vol. 55, pp. 2596-2606, 2008.

[12] J. Tichý, Fundamentals of Piezoelectric Sensorics: Mechanical, Dielectric, and Thermodynamical Properties of Piezoelectric Materials. Verlag Berlin Heidelberg: Springer, 2010.

[13] M.-A. Dubois and P. Muralt, "Properties of aluminum nitride thin films for piezoelectric transducers and microwave filter applications," Applied Physics Letters, vol. 74, pp. 3032-3034, 1999.

[14] H. C. Nathanson, W. E. Newell, R. A. Wickstrom, and J. R. Davis, Jr., "The resonant gate transistor," *Electron Devices, IEEE Transactions on*, vol. 14, pp. 117-133, 1967.

[15] lin, Yang. "Micromechanical Resonant Switches ("Resoswitches") And Resonant Power Converters".N.p., 2015.

[16] C. T.-C. Nguyen, "Vibrating RF MEMS overview: applications to wireless communications," Proceedings of SPIE: Micromachining and Microfabrication Process Technology, vol. 5715, Photonics West: MOEMS-MEMS 2005, San Jose, California, Jan. 22-27, 2005, pp. 11-25.

[17] R. Abdolvand, H.M. Lavasani, G.K. Ho and F. Ayazi, "Thin-film piezoelectric-on-silicon resonators for high-frequency reference oscillator applications," *IEEE Transactions on Ultrasonics, Ferroelectrics, and Frequency Control*, vol. 55, no. 12, pp. 2596-2606, December 2008.

[18] B. P. Harrington, M. Shahmohammadi, and R. Abdolvand, "Toward ultimate performance in GHz MEMS resonators: Low impedance and high Q," *Proc. IEEE Micro Electro Mechanical Systems Conf.*, Jan. 2010, pp. 707–710

[19] K. Wang and C.-C. Nguyen, "High-order medium frequency micromechanical electronic filters," *Microelectromechanical Systems, Journal of*, vol. 8, pp. 534-556, 1999.

[20] Wu, I-Tsang, "Integrated Electrostatically- and Piezoelectrically-Transduced Contour-Mode MEMS Resonator on Silicon-on-Insulator (SOI) Wafer" (2014). *Graduate Theses and Dissertations.*

[21] Dewdney, Julio Mario, "Low Loss VHF and UHF Filters for Wireless Communications Based on Piezoelectrically-Transduced Micromechanical Resonators" (2012). *Graduate Theses and Dissertations.* http://scholarcommons.usf.edu/etd/4309

[22] Nickelinstitute.org. (2014, 10/25/20). Nickel Plating Handbook. Available: https://www.nickelinstitute.org.

[23] G. Gautschi, Piezoelectric sensorics: force, strain, pressure, acceleration and acoustic emission sensors, materials and amplifiers: Springer, 2002.

[24] C. T. C. Nguyen, "MEMS technology for timing and frequency control," IEEE Transactions on Ultrasonics, Ferroelectrics, and Frequency Control, vol. 54, no. 2, pp. 251-270, February 2007.

[25] V. Lim, T. Karacolak, J. Y. Jiang, C. F. Huang and F. Zhao, "Electrostatically-Actuated 4H-SiC In-plane and Out-of-Plane High Frequency MEMS Resonator," IEEE Microwave and wireless Components Letters, vol. 26, no. 1, pp. 28-30, January 2016.

[26] A. Uranga, J. Verd, N. Barniol, "CMOS–MEMS resonators: From devices to applications," Microelectronic Engineering, vol. 132, no. 25 pp. 58-73, January 2015.

[27] M. Baghelani, HB Ghavifekr, A Ebrahimi, "Analysis and suppression of spurious modes of the ring shape anchored RF MEMS contour mode disk resonator," Microsystem Technologies, vol. 17, pp. 1599-1609, October 2011.

[28] W. C. Chen, W. Fang and S. S. Li, "High- Q Integrated CMOS-MEMS Resonators With Deep-Submicrometer Gaps and Quasi-Linear Frequency Tuning," Journal of Microelectromechanical Systems, vol. 21, no. 3, pp. 688-701, June 2012.

[29] H. M. Lavasani, W. Pan, B. Harrington, R. Abdolvand and F. Ayazi, "A 76 dB Ω 1.7 GHz 0.18 μ m CMOS Tunable TIA Using Broadband Current Pre-Amplifier for High Frequency Lateral MEMS Oscillators," IEEE Journal of Solid-State Circuits, vol. 46, no. 1, pp. 224-235, Jan. 2011.

[30] Erbes, P. Thiruvenkatanathan, J. Woodhouse and A. A. Seshia, "Numerical Study of the Impact of Vibration Localization on the Motional Resistance of Weakly Coupled MEMS Resonators," Journal of Microelectromechanical Systems, vol. 24, no. 4, pp. 997-1005, Aug. 2015.

[31] J. Wang, J. E. Butler, T. Feygelson and C. T. C. Nguyen, "1.51-GHz nanocrystalline diamond micromechanical disk resonator with material-mismatched isolating support," Proceedings of 17th IEEE International Conference on Micro Electro Mechanical Systems (MEMS 2004), pp. 641-644, 2004.

[32] J.E.-Y. Lee, A.A. Seshia, "5.4-MHz single-crystal silicon wine glass mode disk resonator with quality factor of 2 million," Sensors and Actuators A: Physical, vol. 156, no. 1, pp. 28-35, Nov. 2009.

[33] M. H. Li, W. C. Chen and S. S. Li, "Realizing Deep-Submicron Gap Spacing for CMOS-MEMS Resonators," IEEE Sensors Journal, vol. 12, no. 12, pp. 3399-3407, Dec. 2012.

[34] M. U. Demirci and C. T. C. Nguyen, "Mechanically Corner-Coupled Square Microresonator Array for Reduced Series Motional Resistance," Journal of Microelectromechanical Systems, vol. 15, no. 6, pp. 1419-1436, Dec. 2006.

[35] S. S. Li, Y. W. Lin, Z. Ren and C. T. C. Nguyen, "An MSI Micromechanical Differential Disk-Array Filter," Proceedings of 2007 International Solid-State Sensors, Actuators and Microsystems Conference (Transducers 2007), pp. 307-311, Lyon, 2007.

[36] G. Wu, D. Xu, B. Xiong and Y. Wang, "High Q Single Crystal Silicon Micromechanical Resonators With Hybrid Etching Process," IEEE Sensors Journal, vol. 12, no. 7, pp. 2414-2415, July 2012.

[37] R. Dussart, T. Tillocher, P. Lefaucheux and M Boufniche, "Plasma cryogenic etching of silicon: from the early days to today's advanced technologies," Journal of Physics D: Applied Physics, 47 (2014) 123001 (27pp).

[38] R. Abdolvand, F. Ayazi "An advanced reactive ion etching process for very high aspect-ratio sub micron wide trenches in silicon," Sensors and Actuators A, vol. 144, pp. 109–116, 2008.

[39] A. Aydemir and T. Akin, "DRIE process optimization to achieve high aspect ratio for capacitive MEMS sensors," Proceedings of the 26th Micromechanics and Microsystems Europe Workshop, Toledo, Spain, September 20-23, 2015.

[40] K.-S. Chen, A.A. Ayon, X. Zhang, S.M. Spearing, "Effect of Process Parameters on the Surface Morphology and Mechanical Performance of Silicon Structures After Deep Reactive Ion Etching (DRIE),"Journal of Microelectromechanical Systems, vol.11, no.3, pp.264-275, 2002.

[41] M. J. de Boer, J. G. E. Gardeniers, H. V. Jansen, E. Smulders, M. J. Gilde, G. Roelofs, J. N. Sasserath, and M. Elwenspoek, "Guidelines for etching silicon MEMS structures using fluorine high-density plasmas at cryogenic temperatures," Journal of Microelectromechanical Systems, vol. 11, no. 4, pp. 385-401, 2002.

[42] Q. Wang, A. D. Rider, D. C. Moore, C. P. Blakemore, L. Cao, G. Gratta, "A density staggered cantilever for micron length gravity probing," Proceedings of 2017 IEEE 67th Electronic Components and Technology Conference (ECTC), Orlando, FL, May 30-June 02, 2017.

[43] Y. Mita, M. Sugiyama, M. Kubota, F. Marty, T. Bourouina, and T. Shibata, "Aspect ratio dependent scalloping attenuation in DRIE and an application to low-loss fiber-optical switches," Proceedings of 19th IEEE International Conference on Micro Electro Mechanical Systems (MEMS 2006), Istanbul, Turkey, January 22-26, 2006.

[44] Y. Li, Y. Xing, M. A. Gosálvez, P. Pal, Y. Zhou, “Particle swarm optimization of model parameters: Simulation of deep reactive ion etching by the continuous cellular automaton,” Proceedings of the 17th International Conference on Solid-State Sensors, Actuators and Microsystems (Transducers & Eurosensors XXVII), June 16-20 2013.

[45] M. C. M. Lee and M. C. Wu, “Thermal annealing in hydrogen for 3-D profile transformation on silicon-on-insulator and sidewall roughness reduction,” Journal of Microelectromechanical Systems, vol. 15, no. 2, pp. 338-343, April 2006.

[46] C.J. Mogab, “The loading effect in plasma etching,” Journal of Electrochemical Society, vol. 124, pp.1262-1268, 1977.

[47] K.P. Giapis, G.R. Scheller, R.A. Gottscho, W.S. Hobson, and Y.H. Lee, “Microscopic and macroscopic uniformity control in plasma etching,” Applied Physics Letters, 57 (10) p.983, 1990.

[48] J. Kiihamäki, S. Franssila “Deep silicon etching in inductively coupled plasma reactor for MEMS,” Physica Scripta, T79, pp. 250-254, 1999.

[49] C. Q. Ru, “Size Effect of on Quality Factor of Micro vol. 94, pp. 051905, 2009.

[50] A. Alsolami, A. Zaman, I. F. Rivera, M. Baghelani and J. Wang, "Improvement of Deep Reactive Ion Etching Process For Motional Resistance Reduction of Capacitively Transduced Vibrating Resonators," in IEEE Sensors Letters, vol. 2, no. 1, pp. 1-4, March 2018, Art no. 5000104, doi: 10.1109/LSENS.2018.2797076.

[51] B. Shiari and K. Najafi, "Surface effect influence on the quality factor of microresonators," 2013 Transducers & Eurosensors XXVII: The 17th International Conference on Solid-State Sensors, Actuators and Microsystems (TRANSDUCERS & EUROSENSORS XXVII), Barcelona, 2013, pp. 1715-1718, doi: 10.1109/Transducers.2013.6627117.

[52] G. Casinovi, X. Gao, and F. Ayazi, “Analytical modeling and numerical simulation of capacitive silicon bulk acoustic resonators,” in Proc. IEEE Int. Conf. MEMS, Jan. 2009, pp. 935–938.

[53] Li-Wen Hung, "High-Q Low-Impedance MEMS Resonators", 2011, eScholarship University of California Electronic Thesis and Dissertations UC Berkeley, Spring 2011, 152 pages.

[54] A. K. Samarao and F. Ayazi, "Postfabrication Electrical Trimming of Silicon Micromechanical Resonators via Joule Heating," in Journal of Microelectromechanical Systems, vol. 20, no. 5, pp. 1081-1088, Oct. 2011, doi: 10.1109/JMEMS.2011.2162489.

[55] J. Wang, Self-Aligned Radial Contour Mode Micromechanical Disk Resonators for Wireless Communications, Doctor Dissertation, University of Michigan, 2006.

[56] Hagleitner, C.; Hierlemann, A.; Lange, D.; Kummer, A.; Kerness, N.; Brand, O.; Baltes, H. Smart single-chip gas sensor microsystem. Nature 2001, 414, 293–296

[57] M. Demirci and C. Nguyen, "Mechanically corner-coupled square microresonator array for reduced series motional resistance," IEEE/ASME J. Microelectromechanical Systems, vol. 15, no. 6, pp. 1419-1436, Dec. 2006.

[58] C. H. Mastrangelo and C. H. Hsu, "Mechanical stability and adhesion of microstructures under capillary forces. I. Basic theory," *Microelectromechanical Systems, Journal of*, vol. 2, pp. 33-43, 1993.

[59] Y.-W. Lin, S.-S. Li, Y. Xie, Z. Ren, and N. C. T. C., "Vibrating micromechanical resonators with solid dielectric capacitive transducer gaps," in IEEE International Frequency Control Symposium and Exposition, 2005, pp. 128-134.

[60] A. Zaman, A. Alsolami, I. F. Rivera and J. Wang, "Thin-Piezo on Single-Crystal Silicon Reactive Etched RF MEMS Resonators," in IEEE Access, vol. 8, pp. 139266-139273, 2020, doi: 10.1109/ACCESS.2020.3012520.

Appendix A: Copyright Permission

The permission below is for the use of the material in Chapter 3.

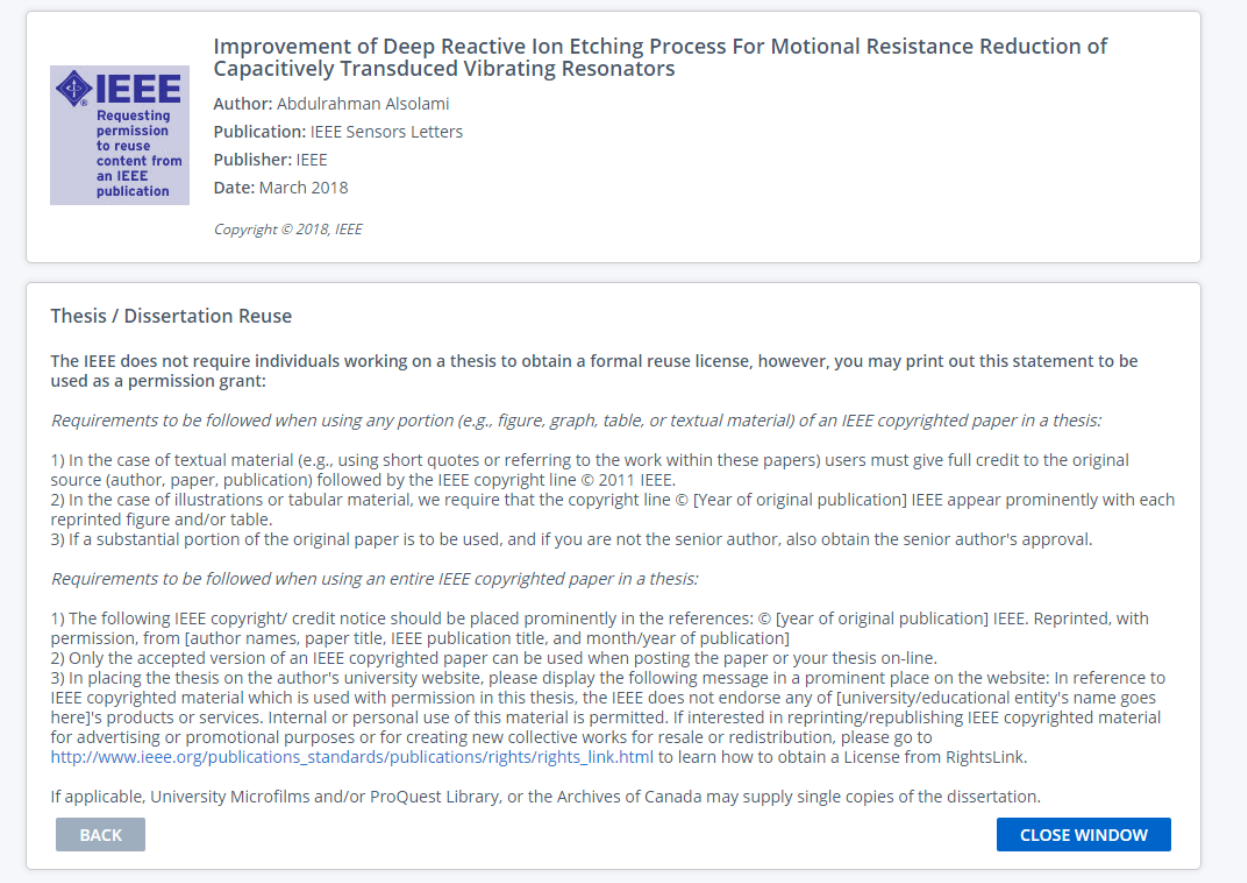

Improvement of Deep Reactive Ion Etching Process For Motional Resistance Reduction of Capacitively Transduced Vibrating Resonators

Author: Abdulrahman Alsolami
Publication: IEEE Sensors Letters
Publisher: IEEE
Date: March 2018

Copyright © 2018, IEEE

Thesis / Dissertation Reuse

The IEEE does not require individuals working on a thesis to obtain a formal reuse license, however, you may print out this statement to be used as a permission grant:

Requirements to be followed when using any portion (e.g., figure, graph, table, or textual material) of an IEEE copyrighted paper in a thesis:

1) In the case of textual material (e.g., using short quotes or referring to the work within these papers) users must give full credit to the original source (author, paper, publication) followed by the IEEE copyright line © 2011 IEEE.
2) In the case of illustrations or tabular material, we require that the copyright line © [Year of original publication] IEEE appear prominently with each reprinted figure and/or table.
3) If a substantial portion of the original paper is to be used, and if you are not the senior author, also obtain the senior author's approval.

Requirements to be followed when using an entire IEEE copyrighted paper in a thesis:

1) The following IEEE copyright/ credit notice should be placed prominently in the references: © [year of original publication] IEEE. Reprinted, with permission, from [author names, paper title, IEEE publication title, and month/year of publication]
2) Only the accepted version of an IEEE copyrighted paper can be used when posting the paper or your thesis on-line.
3) In placing the thesis on the author's university website, please display the following message in a prominent place on the website: In reference to IEEE copyrighted material which is used with permission in this thesis, the IEEE does not endorse any of [university/educational entity's name goes here]'s products or services. Internal or personal use of this material is permitted. If interested in reprinting/republishing IEEE copyrighted material for advertising or promotional purposes or for creating new collective works for resale or redistribution, please go to http://www.ieee.org/publications_standards/publications/rights/rights_link.html to learn how to obtain a License from RightsLink.

If applicable, University Microfilms and/or ProQuest Library, or the Archives of Canada may supply single copies of the dissertation.

BACK CLOSE WINDOW